TUM School of Medicine and Health

Single-cell transcriptomic profiling of the developing cardiac conduction system and in vivo visualization of its components in real-time

Benjamin Maurice Beyersdorf

Vollständiger Abdruck der von der TUM School of Medicine and Health
der Technischen Universität München zur Erlangung eines

Doktors der Medizin (Dr. med.)

genehmigten Dissertation.

Vorsitz: apl. Prof. Dr. Lutz Renders

Prüfende der Dissertation:

1. Prof. Dr. Markus Krane
2. Prof. Dr. Maximilian Reichert

Die Dissertation wurde am 15.04.2024 bei der Technischen Universität München eingereicht und durch die TUM School of Medicine and Health am 06.11.2024 angenommen.

Table of Contents

Acknowledgments

The medical research that led to this thesis was performed in the Sean Wu laboratory at Stanford Cardiovascular Institute, under close mentorship and supervision by my doctoral advisor **Prof. Dr. med. Markus Krane** at the German Heart Center Munich. The science described here was only made possible through enormous support, help and guidance provided by many outstanding scientists and friends.

First and foremost, I am deeply grateful to **Prof. Dr. Markus Krane**, my thesis advisor who provided me the great opportunity to pursue my doctoral studies as a member of the Institute for Translational Cardiac Surgery (INSURE) at the German Heart Center Munich. Furthermore, through the long-standing cooperation between the INSURE Institute and the Sean Wu laboratory at Stanford University, Markus encouraged me to spend a full year at Stanford University to perform my doctorate research. I want to deeply thank Markus for all his support, patience, and encouragement with which he has guided me through the first phase of my scientific career. I will always be thankful and gratefully remember the time in which we have been working together.

I sincerely thank **Prof. Dr. Sean Wu**, Associate Director of the Stanford Cardiovascular Institute and Principal Investigator of my lab at Stanford University, in which I have performed the here described studies, which form the basis of my thesis. The Wu laboratory has not only provided a stimulating professional environment and infrastructure for innovative research, but also allowed me to have a wonderful time in a team of motivated young scientists that have quickly become close friends. Furthermore, the close mentorship of Sean in my actual scientific work as well as his honest interest in the personal development of each of his trainees has been exceptional. I will always remember the weekly meetings and great discussions we had, from which I gained an astounding amount of motivation and priceless scientific knowledge. Whenever I needed help during experiments, Sean was always there to help warm-heartedly. I am deeply thankful for the wonderful and successful time I was able to have in the Sean Wu lab, and for his daily effort in paving my early way in science.

I want to deeply thank **Dr. William Goodyer**, Assistant Professor for pediatrics and cardiology at Stanford University. Will has profoundly shaped my medical and scientific career in various aspects through close training, exceptional mentorship, and support during the 12 months that we have worked together day by day on many exciting projects. First and foremost, Will has sparked my scientific interest and excitement for medical science. Despite all potential failure and pitfalls, he has helped me develop true passion and fascination for science and has thus had a tremendous impact on both my personal development and future career.

Moreover, without the strong support that I have received by members of my lab in the German Heart Center in Munich, this work would not have been possible. Especially, **PD Dr. Harald Lahm** and **Dr. Martina Dreßen** always stood by my side, supported me with great scientific expertise and invested a lot of their time and effort in training me. In my very first year of medical research, Harald and Martina laid an important and profound scientific foundation for all my following scientific endeavors. Additionally, I am thankful for all the fun moments we had both in the lab and at various other events. Thank you for always being wonderful mentors to me.

Additionally, I want to thank **Dr. Stefanie Doppler**, **Irina Neb**, **Nicole Beck**, **Dr. Zhong Zhang**, **Dr. Sarah Hölscher**, **Dr. Palgit Kogan**, and **Xinghai Li** for their support and insightful comments and suggestions.

Further, I want to thank all the lovely members in the Sean Wu laboratory: **Prof. Dr. Sean Wu**, **Dr. William Goodyer**, **Dr. Jan Buikema**, **Dr. Nazan Puluca**, **Dr. Soah Lee**, **Dr. Guang Li**, **Dr. Sharon Paige**, **Aimee Beck**, **Dr. Francisco Galdos**, **Sneha Venkatraman**, **Daniel Lee**, **James Hu** and **Adrija Darsha**. It was great to have such a nice group of close friends to work with and enjoy time together.

The project "Transcriptomic profiling of the developing cardiac conduction system at single cell resolution", as described in chapter I of this thesis, was performed and supported by a group of brilliant friends and scientists: **Dr. William Goodyer**, **Dr. David Paik**, **Dr. Lei Tian**, **Dr. Guang Li**, **Dr. Jan Buikema**, **Orlando Chirikian**, **Shannon Choi**, **Sneha Venkatraman**, **Dr. Eliza Adams**, **Prof. Dr. Marc Tessier-Lavigne**, **Prof. Dr. Joseph Wu** and **Prof. Dr. Sean Wu**. Specifically, precise statistical analyses of large genetic datasets were performed by **Dr. William Goodyer**, **Dr. David Paik** and **Dr. Lei Tan**. Special thanks to every single one of you and for all your great scientific effort.

Further, the project "Generation of novel optical imaging tools for intraoperative visualization of the cardiac conduction system", as described in chapter II, was performed, and profoundly impacted by **Dr. William Goodyer**, **Dr. Nynke van den Berg**, **Dr. Nazan Puluca**, **Dr. Jan Buikema**, **Dr. Elise Robinson**, **Dr. Darren Salmi**, **Dr. Stephan Rogalla**, **Prof. Dr. Eben Rosenthal** and **Prof. Dr. Sean Wu**. This work was only possible through the great effort and passion this group put into this project.

Furthermore, my stay at Stanford would not have been possible without the financial support provided by the **Biomedical Education Program (BMEP)** and the **Bayer Science Fellowship (Carl-Duisberg-Fellowship)**. Thank you for your trust and support.

Finally, I would like to thank my mom and dad (**Prof. Dr. Friedhelm Beyersdorf** & **Dr. Susanne Beyersdorf**), my brother and sister (**Dr. Christoph Beyersdorf** and **Dr. Caroline Beyersdorf**) as well as my wonderful partner **Caroline Schöning**. Thank you for being a constant source of inspiration and for supporting me in pursuing my dreams at any given time in my life.
This work is dedicated to you.

List of Tables

List of Figures

List of Abbreviations

ASD:	Atrial septal defect
ATZ:	Atrial transitional zone
AVB:	Atrioventricular block
AVN:	Atrioventricular node
AWM:	Atrial working myocardium
BB:	Bundle branch
BBB:	Bundle branch block
Bmp2:	Bone morphogenic protein 2
BSA:	Bovine serum albumin
Cacna1g:	Voltage-dependent calcium channel subunit alpha-1g
Cacna2d2:	Voltage-dependent calcium channel subunit alpha-2/delta-2
cAVN:	Compact atrioventricular node
CCS:	Cardiac conduction system
cDNA:	Complementary DNA
CHD:	Congenital heart disease
CM:	Cardiomyocyte
Cntn2:	Contactin-2
Cpne5:	Copine-5
cSAN:	Compact sinoatrial node
CT:	Computed tomography
DAPI:	4’,6-diamidino-2-phenylindole
DAVID:	Database for Annotation, Visualization and Integrated Discovery
DBE:	Dibenzylether
DCM:	Dichloromethane
ECG:	Electrocardiogram
EGFR:	Epidermal growth factor receptor
Etv1:	ETS variant transcription factor 1
FACS:	Fluorescence activated cell sorting
FBS:	Fetal bovine serum
FCM:	Fiberoptic confocal microscopy
FHF:	First heart field
FISH:	Fluorescence *in situ* hybridization
FOV:	Field of view
GAINS:	Goggle augmented imaging and navigation system
GEM:	Gel bead-in-emulsions
GEO:	Gene expression omnibus
GFP:	Green fluorescent protein
Gja5:	Gap junction protein alpha 5
GluR1:	Glutamate receptor subunit 1
GMP:	Good manufacturing practice
GO:	Gene ontology
H&E:	Hematoxylin and eosin
HB:	Heart block
HBSS:	Hank's balanced salt solution
Hcn:	Hyperpolarization-activated cyclic nucleotide-gated cation channel
hES:	Human embryonic stem cell

HIS:	Bundle of His
HRP:	Horseradish peroxidase
ICG:	Indocyanine green
Id2:	DNA-binding protein inhibitor ID-2
iDISCO+:	Immunolabeling-enabled three-dimensional imaging of solvent-cleared organs
Igfbp5:	Insulin-like growth factor-binding protein 5
IHC:	Immunohistochemistry
IND:	Investigational new drug application
INT:	Internodal tracts
iPSC:	Induced pluripotent stem cells
Irx3:	Iroquois-class homeodomain protein IRX-3
Isl1:	ISL LIM homeobox 1
IVS:	Interventricular septum
Kcne1:	Potassium voltage-gated channel subfamily E member 1
Kcnj5:	G protein-activated inward rectifier potassium channel 4
Kcnk3:	Potassium channel subfamily K member 3
LA:	Left atrium
LAVR:	Left atrioventricular ring bundle
LCM:	Laser capture microscopy
L-TGA:	Levo-transposition of the great arteries
MeOH:	Methanol
MRI:	Magnetic resonance imaging
mRNA:	Messenger RNA
NAVR:	Nodal atrioventricular ring
NCBI:	National center for biotechnology information
NIR:	Near-infrared
Nptn:	Neuroplastin
Ntm:	Neurotrimin
OTL:	Office of technology licensing
pAVB:	Postoperative atrioventricular block
PBS:	Phosphate-buffered saline
PC:	Principal component
PCA:	Principal component analysis
PCR:	Polymerase chain reaction
PD:	Pacemaker dysfunction
PET:	Positron emission tomography
PF:	Purkinje fibers
PFA:	Paraformaldehyde
PMI:	Post-mortem interval
PMJ:	Purkinje fiber-myocyte junction
POA:	Postoperative arrhythmias
PPI:	Permanent pacemaker implantation
QC:	Quality control
RA:	Right atrium
RAVR:	Right atrioventricular ring
Rgs6:	Regulator of G-protein signaling 6
RNA-seq:	RNA-sequencing
RPM:	Rounds per minute

RT:	Room temperature
SAN:	Sinoatrial node
SACP:	Sinoatrial conduction pathway
SBR:	Signal to background ratio
Scn5a:	Sodium channel protein type 5 subunit alpha
ScRNA-Seq:	Single-cell RNA-sequencing
SEP:	Sinoatrial exit pathway
Sema3a:	Semaphorin 3A
Shox2:	Short stature homeobox protein 2
Smoc2:	SPARC-related modular calcium-binding protein 2
SVC:	Superior vena cava
TAVR:	Transitional atrioventricular ring
Tbx3:	T-box transcription factor 3
Tbx5:	T-box transcription factor 5
TF:	Transcription factor
T-SNE:	T-distributed stochastic neighbor embedding
Tz:	Transitional cells
UMI:	Unique molecular identifier
VCS:	Ventricular conduction system
VF:	Ventricular fibrillation
VM:	Ventricular myocardium
VSD:	Ventricular septal defect
VT:	Ventricular tachycardia
VTZ:	Ventricular transitional zone
WBC:	White blood cells

General introduction

The cardiac conduction system

Rhythmic beating of the heart is performed over 30 million times a year and over 2 billion times throughout an average human life. To allow for coordinated contraction of the human heart, providing blood and nutrients to the entire body, roughly 5 billion heart cells[1] must work in synchrony. This precise orchestration of our everyday heartbeat is guided and driven by a small subset of heart cells, altogether known as the cardiac conduction system (CCS). The CCS consists of various unique components including the sinoatrial node (SAN), the atrioventricular node (AVN), the bundle of His (HIS), left and right bundle branches (BB) as well as the Purkinje fiber system (PF)[2] **(Figure 1.1)**.

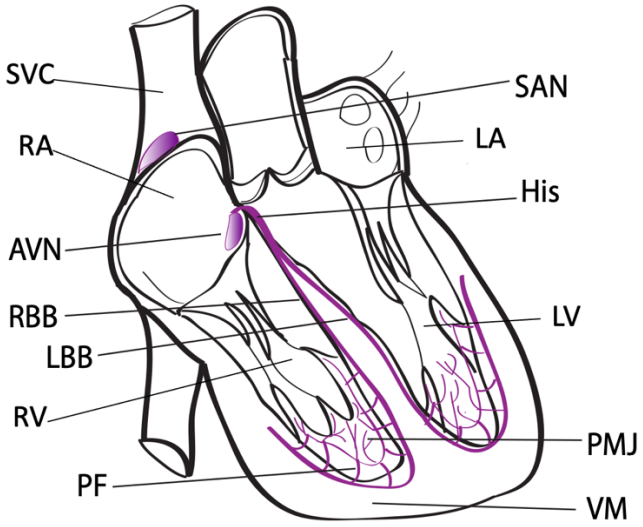

Figure 1.1: Schematic representation of cardiac conduction system components
Cardiac conduction system components are highlighted in purple, while additional structures of a schematic heart are drawn colorless. AVN indicates atrioventricular node; His: bundle of His; LA: left atrium; LBB: left bundle branch; LV: left ventricle; PF: Purkinje fibers; PMJ: Purkinje fiber-myocyte junction; RA: right atrium; RBB: right bundle branch; RV: right ventricle; SAN: sinoatrial node; SVC: superior vena cava; VM: ventricular myocardium. From[3].

The SAN dictates the rhythm of the heart and is the natural pacemaker in healthy individuals[4]. The core component of the SAN, also known as the compact SAN (cSAN), is comma-shaped and harbors both a “head” as well as a “tail” subpopulation of cells[3,5–7]. The SAN head lies right at the junction of the superior vena cava (SVC) and the right atrium (RA). Further, SAN head cells are contiguous with the SAN tail, which is anatomically aligned along the terminal crest[7]. A subset of pacemaker cells within the cSAN rhythmically depolarizes, on average about 60-100 times per minute in a resting state in adults, initiating electrical impulses. Direct injury, electrolyte disturbances, age-related fibrosis or even genetic alterations can cause SAN dysfunction also known as “sick sinus syndrome”[8].

Electrical impulses generated within the SAN then spread through the atrial myocardium and internodal tracts (INT), subsequently delivering depolarization to the AVN[9]. First described by Tawara and Aschoff in Freiburg (Germany) in 1906, the AVN is situated in the crux of the heart within a structure called the triangle of Koch. More specifically, in the bottom floor of the right atrium, the triangle of Koch is delineated by the membranous septum, the fibrous tendon of

Todaro and the septal tricuspid leaflet[10]. The AVN performs three main functions[11,12]: Firstly, the AVN serves as an electrical delay station, slowing down atrioventricular conduction and thus allowing for sufficient ventricular filling. Secondly, AVN cells possess features of automaticity and are hence appreciated as secondary pacemaker cells of the heart in case of SAN failure. Finally, due to its extended refractory period, the AVN helps to prevent atrial tachyarrhythmias from exciting the ventricles at similarly fast rates, thus serving as an electrical gatekeeper between the upper (atrial) and lower (ventricular) cardiac chambers. Due to its crucial role for cardiac rhythm, AVN dysfunction may lead to severe rhythm disorders, including atrioventricular block (AVB) and reentrant AV nodal tachycardias.

Extending anteriorly and inferiorly, AVN cells are in direct contact with the bundle of His, which eventually crosses a fibrous plane insulating both atria from the ventricles. Thus, the bundle of His is the only electrical bridge between the upper and lower cardiac chambers in healthy individuals[13]. Thus, disruption of His function may cause severe arrhythmias, ranging from AV conduction delays to complete AVB.

The anterior side of the His bundle forks into the left and right BB running down either side of the interventricular septum (IVS). As part of the ventricular conduction system, malfunction of either bundle branch may lead to a form of conduction disturbance called bundle branch block (BBB)[14], which may require pacemaker implantation in order to restore sufficient cardiac synchrony between the right and left ventricles.

Depolarization travels down the IVS through both left and right BB, eventually giving rise to an intricate web of PF. First described in 1839 by the anatomist and physiologist Jan Evangelista Purkinje, the complex Purkinje fiber system is interlaced in both ventricles and builds the junction from conduction system to the working ventricular myocardium (VM)[15]. Fast conductance and tight coupling to the VM are essential characteristics of PF. However, in cases of ectopic ventricular heartbeats or electrolyte disturbances, the tight electrical coupling at the Purkinje fiber-myocyte junction (PMJ) may serve as a gateway for re-entry tachyarrhythmias and other rhythm disorders[16,17].

Disruption of any of these specialized CCS components can result in a host of severe clinical manifestations such as pacemaker dysfunction (PD), complete heart block (HB), BBB, decreased cardiac output and even life-threatening diseases such as ventricular tachycardia (VT), ventricular fibrillation (VF) and sudden death[14,18–20].

Major hurdles for research in the field

Although the incidence of rhythm abnormalities is substantial and are comparable to those of stroke, acute myocardial infarction, and heart failure[21], our understanding of cardiac arrhythmias remains incomplete. Major obstacles in CCS research include a) small total conduction cell numbers, b) their intricate three-dimensional localization within the heart, c) inter- and intracomponent cell type heterogeneity, as well as d) our inability to isolate and visualize conduction cells from the surrounding working myocardium[13,22,23]. In order to improve our molecular understanding of the CCS, which is needed to elucidate novel molecular targets for the diagnosis and treatment of cardiac arrythmias, the abovementioned hurdles need to be overcome.

Aims of this study

The current study, aimed to tackle the abovementioned challenges in CCS research, is presented in two parts.

Part I describes single-cell RNA-sequencing (scRNA-seq) used for precise transcriptomic profiling of the entire murine cardiac conduction system at single cell resolution. Further, exhaustive data analyses are performed and immunohistochemistry, florescence *in situ* hybridization (FISH) and immunolabeling-enabled three-dimensional imaging of solvent-cleared organs (iDISCO+) were performed on murine heart tissues for data validation, thus establishing a comprehensive CCS gene atlas for the first time.

Part II builds on these findings discovering multiple novel cell surface markers highly enriched within the entire CCS or individual CCS components. Extensive data validation of certain molecular markers is performed in murine and human heart tissues. Thus, novel CCS-specific molecular targets are then used to create antibody-based optical imaging tools for the *in vivo* visualization of the CCS. Moreover, preclinical validation of these novel tools is performed to assess *in vivo* antibody-binding characteristics and to prove high-resolution and strong signal detection in real-time at submillimeter resolution, promoting clinical translation. Firstly, the real-time, intraoperative visualization of individual CCS components will allow cardiac surgeons to visualize the CCS and thus prevent intraoperative injury to conduction tissues. Additionally, the elucidation of novel molecular targets may also promote the discovery of novel precision treatments for common arrhythmias (e.g. targeted AV node ablation, delivery of antiarrhythmic agents to the AVN/His for junctional ectopic tachycardia etc.).

Part I: Transcriptomic profiling of the developing cardiac conduction system at single cell resolution

1.1. Introduction

1.1.1. Transitional cells

While it is known that each component of the CCS has its own unique physiological and electrochemical properties (eg. SAN vs. AVN), large intracomponent cell type heterogeneity has additionally been recognized. Each individual component is made up of a number of different cell types, including conduction cells, endothelial cells, neuronal cells, fibroblasts, white blood cells and others[22–25], displaying large cell type heterogeneity within CCS components. One of the most poorly recognized cell types within the CCS are known as "transitional cells" (Tz). Transitional cells act as a cellular bridge between the CCS and the surrounding working myocardium and have been described in all major components of the conduction system including the SAN[5], the atrioventricular conduction axis[13], and the PF network[15]. Furthermore, studies have demonstrated that transitional cells display a hybrid phenotype between both working myocytes and conduction cells[26,27]. While the true function of transitional cells is unclear, these cells are hypothesized to promote appropriate electrical coupling, facilitate the spread of depolarization, provide a high resistance barrier and amplify the electrical current before passing it on to the surrounding myocardium[5,15,28]. However, despite Tz have been implicated as key players in cardiac rhythm disturbances[29], Tz have remained largely elusive due to technical challenges in their characterization.

Transitional cells have been described in the SAN area and are thought to play a key role in normal SAN function. In this regard, recent functional mapping studies have shown that the spread of depolarization from pacemaker cells within the SAN through both cardiac atria does not occur in circular waveforms, but through distinct pathways of higher velocity[5]. Thus, it is hypothesized that electrical impulses, generated in a subpopulation of the compact SAN, are bridged to the atrial myocardium through cellular junctions named SAN exit pathways (SEP)[30], also referred to as SAN conduction pathways (SACP)[5]. As transitional cells have first been observed at the periphery of the compact SAN[27], they might play a crucial role in the initiation of cardiac beating. However, like the rest of the CCS, SAN Tz remain poorly understood, including their physiological function, transcriptomic profile and precise anatomic location.

Besides SAN Tz, transitional cells in the AVN region have been observed and studied as early as 1974[31]. However, obstacles in the identification and isolation of these cells have hindered their deeper molecular characterization. The atria and ventricles are electrically insulated from each other by a plane of fibrous tissue between them. Recent studies[13] suggest that on the atrial side, the compact AVN (cAVN) is in direct contact to additional conduction cells named mitral and tricuspid nodal atrioventricular rings (NAVR) as well as atrial septum nodal cells **(Figure 1.2)**.

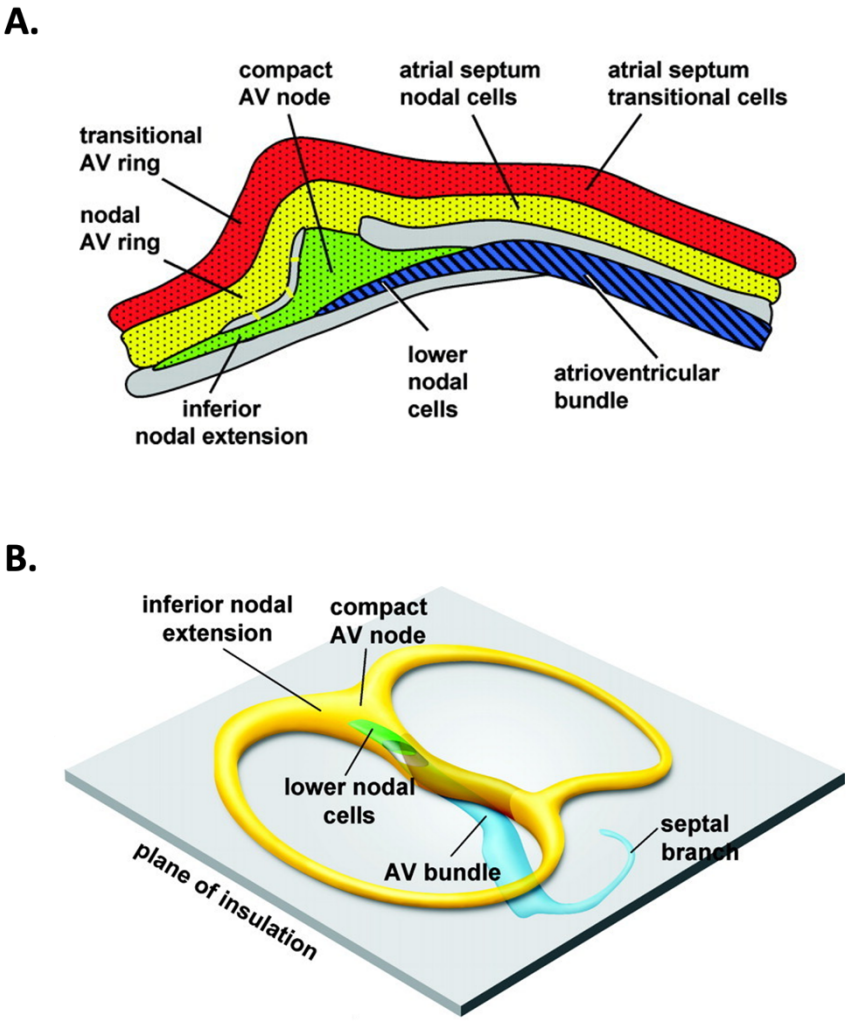

Figure 1.2: Schematic representation of transitional cell types in the atrioventricular node region
A. Two-dimensional representation of cell types within the atrioventricular conduction axis. **B.** Three-dimensional model illustrating conduction cell types within the atrioventricular conduction axis. AV indicates atrioventricular. From[13].

Together, these cells build a figure-of-eight structure that lies at the atrial side adjacent to the fibrous body. Additionally, these studies show that both NAVR as well as septal nodal cells may be separated from the working atrial myocardium by transitional AV rings (TAVR) and septal transitional cells, respectively. The discovery of these novel cell types has sparked much interest in their putative role in cardiac rhythm disorders and molecular targets for the prevention and treatment of diseases. Thus, further characterization of AVN associated transitional cells is needed.

Transitional cells have not only been found in the SAN and AVN region, but also along the Purkinje fiber system[15]. A sheet of PF transitional cells was previously shown to insulate PF cells from the working myocardium[15,32]. In part, these PF Tz may be involved in the delivery of depolarization from PF to ventricular myocytes and play a role in the physiologic conduction delay of about 5 msec at the Purkinje fiber-myocyte junction[33]. PF Tz are unique in various aspects. Morphologically, PF Tz are described as smaller in cell size than standard PF cells. PF Tz show no T-system and sarcoplasmic reticulum, lacking intercalated discs and containing only few specialized intercellular junctions[15,32]. Electrophysiologically, Tz action potentials show multiple unique characteristics: a smaller resting potential, a slower upstroke velocity,

multiple components in their upstroke or plateau phase, a smaller action potential amplitude and a shorter action potential duration in comparison to potentials recorded from Purkinje fibers or working cardiomyocytes[15,32]. These findings suggest a distinct role of PF Tz in amplifying the electrical current before passing it on to the ventricular myocardium as well as providing a high resistance barrier, thus helping to prevent re-entrant tachycardias. While it has been noted that PF Tz play an integral role in the coordinated contraction of the heart as well as the prevention of severe rhythm disorders[29], our knowledge about their true function and molecular characterization remains incomplete.

In summary, many different cell types work in precise synchrony for the normal physiologic function of each CCS component. Transitional cells define unique cell types found in the SAN region, the AV conduction axis as well as the PF system. Even though these cells have been implicated in various fatal arrhythmias[29], our molecular understanding of transitional cells and their role in cardiac pathologies is limited. Thus, technical limitations need to be overcome to uncover novel genetic markers for the improved identification, characterization, and isolation of transitional cells.

1.1.2. Transcriptomic characteristics of conduction system components

Uncovering transcriptional fingerprints for unique cell types allows not only precise cell type identification and cell isolation, but additionally provides deep insight into cell development, function, and the pathogenesis of diseases. However, elucidating the molecular landscape of the CCS and its unique components has been extremely challenging due to several inherent obstacles. Namely, small total numbers of conduction cells, their highly complex three-dimensional architecture within the heart, and large intercomponent and intracomponent cell type heterogeneity[22,23]. To date, these obstacles have hindered the full molecular characterization of the CCS. Thus, the scientific community is currently limited to few gold standard conduction markers including a handful of key transcription factors as well as CCS-specific ion channels.

Some of these known CCS-specific ion channel genes play an important role in automaticity, a quintessential feature of conduction cells. Automaticity is the ability of the SAN to spontaneously depolarize and thus initiate cardiac beating without any activation from neighboring cells[34]. Downstream CCS components such as the AVN, His and PF also display automaticity at much slower rates thus serving as backup pacemakers in case of SAN failure[11,35]. A major contributor to automaticity within pacemaker cells are the hyperpolarization-activated cyclic nucleotide-gated (Hcn) ion channels, mainly Hcn4. These are essential to maintain the so-called “funny current” (If) in pacemaker cells[36]. The current’s name refers to its unusual characteristic of channel activation upon intracellular hyperpolarization. This feature of the funny current, also known as the “membrane clock”, is essential to allowing pacemaker cells the ability to reenter the depolarization cycle automatically after every action potential. Thus, well-established Hcn-channels have provided some of the first gold-standard conduction cell markers.

Additionally established conduction cell markers include classic markers for SAN identification, such as Hcn1, Hcn4, Cacna2d2, Cav1.3, Cav3.1, Cav3.2, Cpne5, Rgs6, Ntm, and Smoc2 as well as the transcription factors (TF) Shox2, Tbx3, Tbx5, Tbx18, and Isl1[7,22,23,25,37–42]. The AVN is characterized by high levels of Hcn4, Cacna2d2, Gjd3, Gjc1, Kcne1, Cpne5, Rgs6, Ntm and the TF Tbx2 and Tbx3[13,43–46]. Further, the His bundle is characterized by high levels

of Hcn4, Cacna2d2, Kcne1, Scn5a, Gjc1, Gja5, Cpne5, Rgs6, Ntm as well as the TF Tbx3 and Etv1[13,44,47]. And lastly, the PF system is characterized by high levels of Cacna2d2, Gja5, Scn5a, Cpne5, Rgs6, Ntm and the TF Irx3 and Etv1[48–50]. These markers are well-known CCS-specific markers which are often used in this study to distinguish conduction cells from working myocytes, which do not express the above-mentioned markers at similar levels or combinations or at all.

Genetic markers are crucial for our biological understanding of the CCS. However, the large variety of different cell types contained within each component of the conduction system has imposed a major challenge in transcriptomic profiling of the CCS due to data contamination by non-conduction cell types. Conventional bulk RNA-sequencing (RNA-seq) provides average gene expression levels across a pool of cells. However, a conduction tissue sample generally contains conduction cells, transitional cells and even other cell types such as fibroblasts or endothelial cells. Thus, using bulk RNA-seq it is hardly possible to trace differentially expressed genes from a heterogeneous sample such as the heart back to the cell type that these gene transcripts are originating from. Most recent RNA-seq attempts have therefore utilized sophisticated pacemaker cell purification methods such as *Hcn4*-based laser capture microscopy (LCM)[23] or *Tbx3*-green fluorescent protein (gfp)-based FACS purification[22]. However, results from these studies were still plagued with immense non-CCS gene contamination issues. Thus, precise transcriptomic analyses of highly pure CCS cell types are needed. Not only does the transcriptomic signature of a given cell allow for identification and the further study of cardiac conduction cell types, but it also allows for deep insight into cell identity, crucial developmental cues and electrophysiologic properties, all needed to understand disease processes and elucidate novel therapeutic targets. Single-cell RNA-sequencing is ideal to overcome all above-mentioned hurdles and to provide precise transcriptomic fingerprints at single cell resolution.

1.1.3. Single-cell RNA-sequencing

Billions of cells that make up the entire human body are equipped with a nearly identical genome. However, not all genes are actively transcribed at the same time. A sophisticated regulatory machinery allows unique sets of genes to be transcribed in each cell type at a given timepoint. This cell-type specific transcriptome is the cellular blueprint for all ion channels, receptors, growth factors, transcription factors, cytoskeletal elements and more. Thus, a cells transcriptome displays its unique construction manual providing insight into cell fate, molecular properties, and cellular activity.

Bulk RNA-seq allows for the analysis of average gene expression levels across pools of cells. However, bulk RNA-seq does not take cell-to-cell variability into account, nor heterogeneity of various cell types across a given sample. In contrast, scRNA-seq has revolutionized molecular analyses by allowing for transcriptome analysis at single cell resolution[51,52]. This technique broadly entails barcoding and thus uniquely labeling single cells in a given tissue, quantitatively and qualitatively evaluating its entire transcriptome. Thus, scRNA-seq can provide individual transcriptomic fingerprints of heterogenous tissues at single cell resolution.

First steps for scRNA-seq data acquisition include experimental design, tissue dissection, tissue digestion into a single cell suspension and cell capturing. The current study made use of a microdroplet-based microfluidics approach[53]. Here, single cells are captured in microdroplets, each containing a uniquely barcoded set of oligonucleotides. Further, cell lysis

and reverse transcription is carried out within the droplets, incorporating a cell-specific barcode into each complementary DNA (cDNA) molecule[54]. Subsequent cDNA amplification, library generation and high-throughput sequencing ultimately generate scRNA-seq data from the sample of interest. At this point, quality control (QC) is performed to reduce biological and technical noise. Various QC tools are available that help determine quality distributions across reads and cells, thus eliminating low quality data as well as data derived from damaged cells and duplicates. Further, reads are aligned, and subsequent data normalization helps to remove cell-specific biases.

Interpretation of large datasets starts with cell type identification. Single cells possess their own unique transcriptomic fingerprint and thus, drawing clear borders between one cell type and another can be challenging. The original data contains thousands of cells which all show thousands of genes expressed at fine expression level differences which results in high dimensionality of normalized datasets. As a way of easier data interpretation, unsupervised linear dimensionality reduction methods such as principal component analysis (PCA)[55], or non-linear dimensionality reduction methods such as t-distributed stochastic neighbor embedding (t-SNE)[56] can be used to display the data in two dimensions. Unsupervised cell clustering by t-SNE allows to group cells based on their global gene expression profile and thus spatially separates the most obvious cell types in two-dimensions. At this point, analyses of known reliable marker gene expression can be used to identify the biological cell type underlying a specific cluster of cells. If needed, a certain identified cell cluster can be selected for further unsupervised subcluster analysis, as performed in this study.

While previous studies have applied sophisticated bulk RNA-seq approaches to major components of the cardiac conduction system, these studies were only able to acquire average gene expression data across the entirety of the conduction tissue that was isolated[22,23]. Thus, bulk RNA-seq studies were plagued with non-CCS cell types contaminating the data and additionally, important cell types such as transitional cells have remained elusive. In contrast, scRNA-seq is ideal to tackle the above-mentioned challenges in CCS research. Hence, scRNA-seq was harnessed in this study to provide deep insight into the molecular biology underlying CCS function in development, health, and disease.

1.1.4. Preliminary work

The preliminary work described in the following paragraphs was performed at Stanford University before the start of my own scientific work. Thus, this work has been performed by Dr. William Goodyer and colleagues in the Sean Wu laboratory setting the ground for my personal research and contributions. To allow for a detailed look into how the following data was acquired, this preliminary work also finds space in the *Material and Methods* section of this thesis.

Firstly, three zones of microdissection were harvested from CD1 mouse hearts at embryonic day 16.5 (E16.5), including the SAN with its immediately surrounding tissues (zone I), the AVN/His region (zone II) as well as the BB/PF system (zone III). A total of 22,462 cells deriving from all major components of the murine CCS were freshly harvested and further processed in a designed single-cell RNA-sequencing workflow using the commercial droplet-based cell capture platform from 10× Genomics (**Figure 1.3**) for scRNA-seq data acquisition.

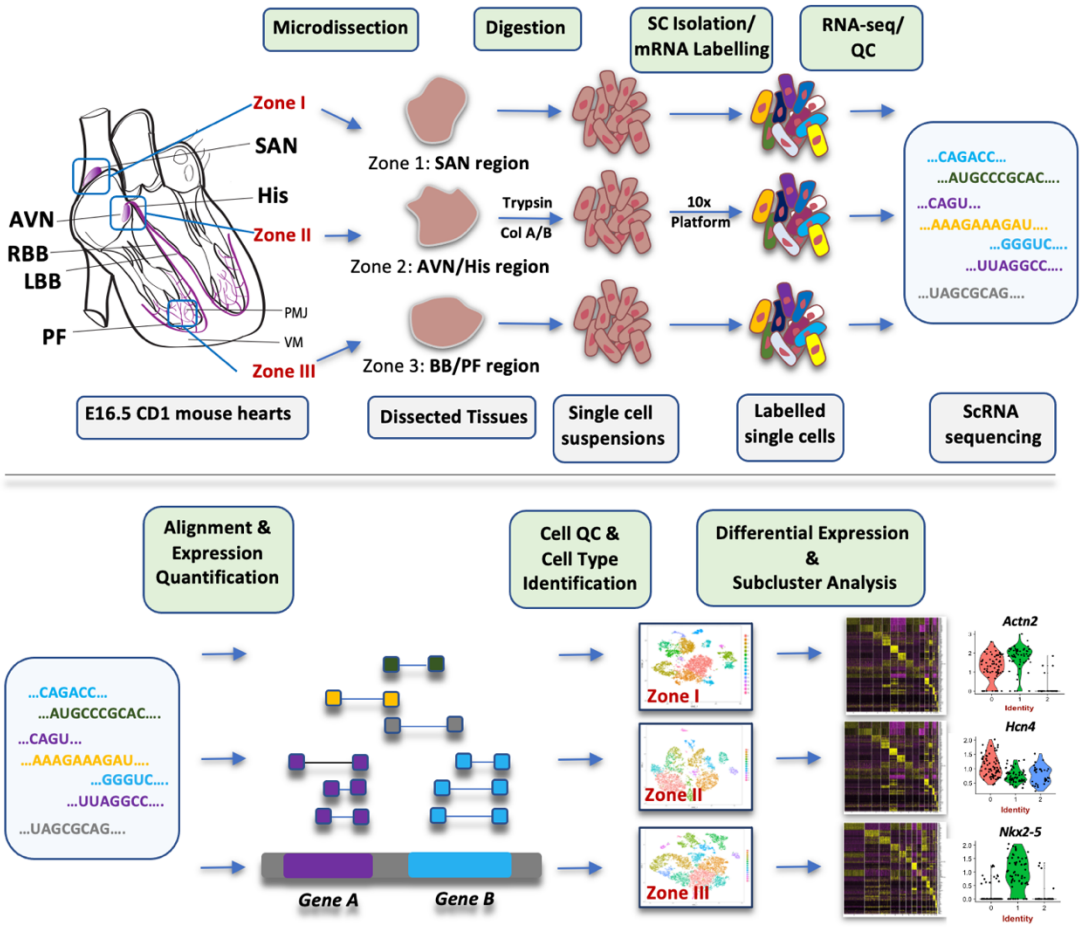

Figure 1.3: Schematic representation of the experimental design and single-cell RNA-sequencing workflow
Wild-type, embryonic day 16.5 (E16.5) CD1 mouse hearts were harvested, and 3 zones of microdissection were isolated based on anatomic landmarks. Zone I: sinoatrial node (SAN) region, zone II: atrioventricular node (AVN)/His bundle (His) region, and zone III: bundle branch (BB)/Purkinje fiber (PF) region. A minimum of 6 embryonic hearts were pooled per zone. Tissues were digested into a single cell (SC) suspension using trypsin and collagenase A/B, isolated via oil droplets, mRNA was labeled with cell-specific barcodes, a library was created and subsequently sequenced, all using the commercial droplet-based cell capture platform from 10× Genomics. Reads were then aligned with gene expression quantification followed by a series of quality control (QC) steps as well as differential gene expression and subcluster analysis. Col A/B indicates collagenase A/B; LBB: left bundle branch; PMJ: Purkinje fiber-myocyte junction; RBB: right bundle branch; scRNA-seq: single-cell RNA sequencing; VM: ventricular myocardium. Modified from[3].

Upon data acquisition and normalization, unsupervised weighted gene co-expression analysis was performed for two-dimensional data organization and spatial separation of cells based on differences in global gene expression. In this regard, cell clustering and dimensionality reduction by t-distributed stochastic neighbor embedding (t-SNE) was performed on each zone, respectively. As a result, all major cardiac cell types were successfully identified (**Figure 1.4**). Most importantly, one distinct cell cluster was detected in each zone, representing bona fide conduction cells (zone I: cluster 9 contains SAN cells; zone II: cluster 4 contains AVN/His cells; zone III: cluster 13 contains BB/PF cells).

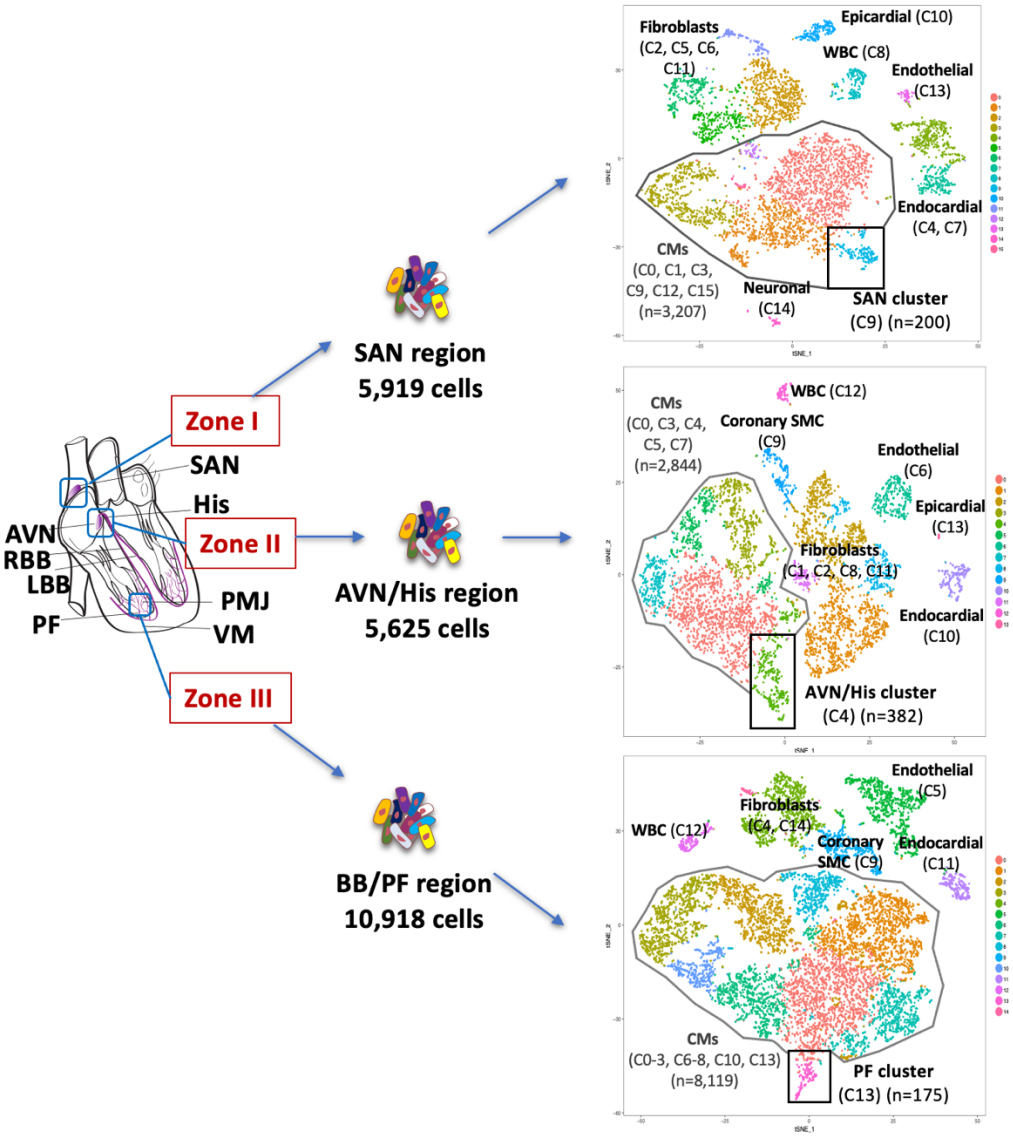

Figure 1.4: Bioinformatic data analyses reveal conduction system-specific cell clusters
First, cells from three zones of microdissection (zone I: 5,919 cells; zone II: 5,625 cells; zone III: 10,918 cells) were obtained and underwent a designed single-cell RNA-sequencing workflow, as shown in Figure 1.3. Cell clustering and dimensionality reduction by t-distributed stochastic neighbor embedding (t-SNE) was performed on data derived from each zone, respectively. T-SNE plots for each zone are shown on the right, entailing all major cardiac cell types, including one conduction cell cluster in each zone respectively (C9 in zone I = SAN cluster; C4 in zone II = AVN/His cluster; C13 in zone III = PF cluster). CM indicates cardiomyocyte; LBB: left bundle branch; PMJ: Purkinje fiber-myocyte junction; RBB: right bundle branch; SMC: smooth muscle cell; VM: ventricular myocardium; and WBC: white blood cells. Modified from[3].

Subsequently, subcluster analyses were performed to identify minor CCS cell types present within the dataset. To distinguish clusters of transitional cells from core conduction cell clusters, borders were drawn based on differences in established marker gene expression as indicated in **Figure 1.5**.

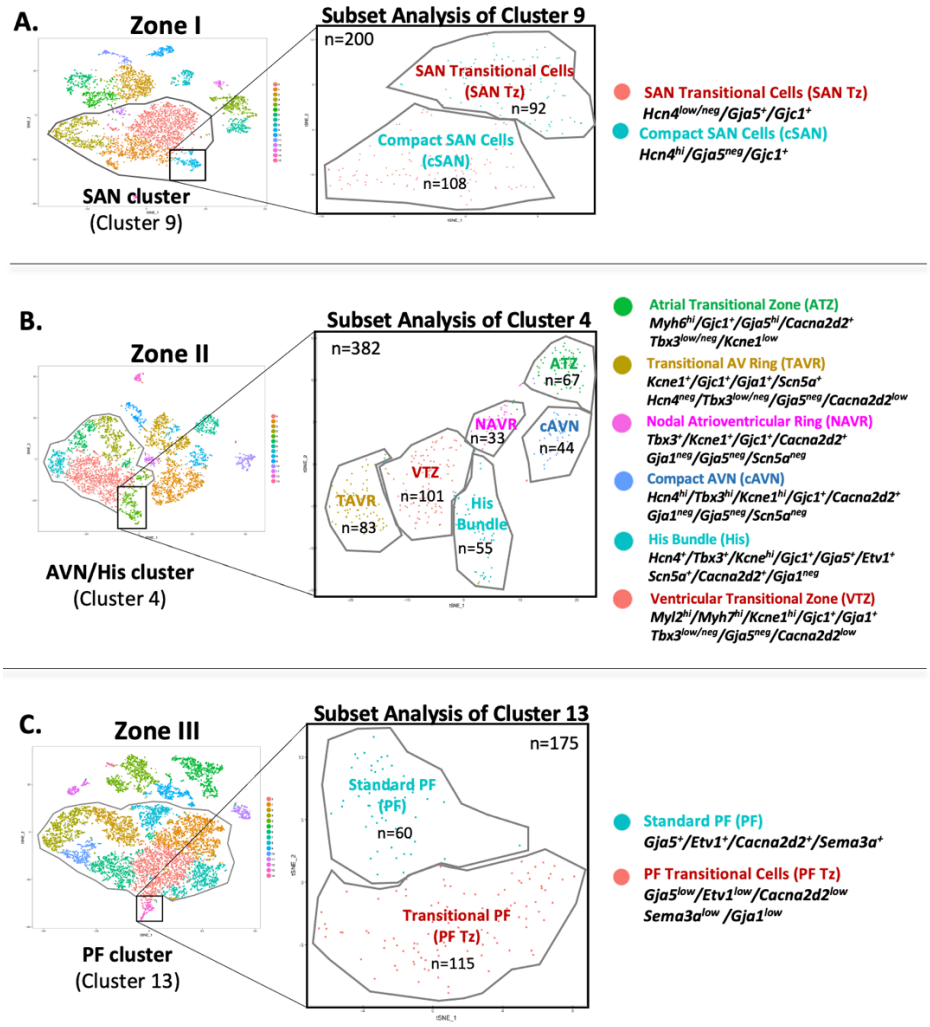

Figure 1.5: Subcluster analyses reveal transcriptomic profiles of transitional cells in all components of the cardiac conduction system

Borders around each cell cluster are drawn based on differences in established marker gene expression as indicated on the right. **A.** Subcluster analysis of cluster 9 cells from zone I (n=200) results in the identification of 2 distinct cell subclusters consistent with compact sinoatrial node (SAN) cells and SAN transitional cells displayed in a t-distributed stochastic neighbor embedding (t-SNE) plot. **B.** Subcluster analysis of cluster 4 cells from zone II (n=382) results in the identification of 6 distinct cell subclusters representing an atrial transitional zone (ATZ), transitional AV ring (TAVR), nodal atrioventricular ring (NAVR), compact AVN (cAVN), His bundle (His), and a ventricular transitional zone (VTZ) as displayed in the t-SNE-plot on the left. **C.** Subcluster analysis of cluster 13 cells from zone III (n=175) results in the identification of 2 distinct cell subclusters consistent with a standard Purkinje fiber (PF) cell cluster and transitional PF cell cluster (PF Tz) as displayed in a t-SNE-plot. Modified from[3].

First, SAN cells of cluster 9 (zone I) were further analyzed resulting in the distinct identification of SAN Tz in addition to core SAN cells (**Figure 1.5A**). Moreover, six distinct cell clusters could be distinguished within AVN/His cells of cluster 4 (zone II) and were named compact AVN (cAVN), nodal AV ring (NAVR), His bundle, transitional AV ring (TAVR), atrial transitional zone (ATZ) and ventricular transitional zone (VTZ) based on differences in established marker gene expression (**Figure 1.5B**). Finally, subcluster analysis of PF cells in cluster 13 (zone III) revealed bona fide PF transitional cells in addition to proper Purkinje fiber cells (**Figure 1.5C**). Thus, the scRNA-seq dataset contains detailed transcriptomic information for all components of the CCS including previously elusive cell types such as transitional cells.

1.1.5. Aims of this study

Using the scRNA-seq data mentioned above, this study aims to generate the first comprehensive gene atlas of the mammalian cardiac conduction system, in order to provide insight into the identity, development and electrophysiologic properties of CCS components at single cell resolution. Additionally, this approach aims at the discovery and validation of novel and specific genetic CCS-markers crucial to identify and isolate CCS subtypes as well as to understand disease processes and elucidate novel therapeutic targets.

1.2. Material

1.2.1. Single cell isolation	
Collagenase A	#10103586001, Roche, USA
Collagenase B	#11088807001, Roche, USA
FBS serum	# 16000044, Thermo Fisher, USA
HBSS (Calcium^{+}, Magnesium^{+})	#14025134, Thermo Fisher, USA
Trypsin	# 15050065, Thermo Fisher, USA

1.2.2. Immunohistochemistry	
Bovine Serum Albumin	#A7906, Sigma-Aldrich, USA
Cover Glasses (24x60 mm)	#CGI-2460, IMEB, USA
Electron Microscopy Sciences Nail Polish	#72180, Fisher Scientific, USA
Paraformaldehyde	#50-980-487, Thermo Fisher, USA
Immunostaining Moisture Chamber	#240-9000-010, Caplugs Medical, USA
Microscope Slides	#12-550-15, Thermo Fisher, USA
Mounting media (+ DAPI)	#H-1200, Vector Laboratories, USA
PBS (10x)	#70011-044, Thermo Fisher, USA
Staining Jar	#UX-48585-30, Cole-Parmer, USA
Triton X-100	#648462, Sigma-Aldrich, USA
Tissue-Plus OCT	#23-730-571, Thermo Fisher, USA

1.2.3. Immunolabeling-enabled three-dimensional imaging of solvent-cleared organs	
Benzyl ether 98% (DBE)	#108014, Sigma-Aldrich, USA
Blocking solution (50 ml)	• 42 mL PTx.2 • 3 mL of Donkey Serum • 5 mL of DMSO
Dichloromethane (DCM)	#270997, Sigma-Aldrich, USA
Dimethyl Sulfoxide (DMSO)	#D8418, Sigma-Aldrich, USA
Donkey Serum	#S30, Sigma-Aldrich, USA
Glycine	#G7126, Sigma-Aldrich, USA
Heparin	#375095, Sigma-Aldrich, USA
Hydrogen Peroxide (30% in H20)	#216763, Sigma-Aldrich, USA

Methanol	#A452-4, Thermo Fisher, Canada
Nalgene Syringe Filter 0.2 µm	#723-2520, Thermo Fisher, USA
Permeabilization solution (500 mL)	• 400 mL PTx.2 • 11.5 g of Glycine • 100 mL of DMSO
PTwH (1 L)	• 100 mL PBS 10x • 2 mL Tween-20 • 1 mL of 10 mg/mL Heparin stock solution
PTx.2 (1 L)	• 100 mL PBS 10x • 2 mL TritonX-100
Tween-20	#P5927, Sigma-Aldrich, USA

1.2.4. Primary antibodies	
Anti-Cpne5 rabbit polyclonal	#NBP184406, Novus Biologicals, USA
Anti-Cx40 rabbit polyclonal	#Cx40-A, Alpha Diagnostics, USA
Anti-Hcn4 rat monoclonal	#ab32675, Abcam, USA
Anti-Igfbp5 goat polyclonal	#AF578, R&D systems/Thermo Fisher, USA
Anti-Rgs6 rabbit polyclonal	#ab155809, Abcam, USA
Anti-Smoc2 sheep polyclonal	#AF5140, R&D Systems, USA

1.2.5. Secondary antibodies	
Chicken anti-rat IgG AlexaFluor 594	#A31572, Invitrogen, USA
Chicken anti-rat IgG AlexaFluor 647	#A21472, Invitrogen, USA
Donkey anti-goat IgG Alexa Fluor 555	#A21432, Invitrogen, USA
Donkey anti-goat IgG Alexa Fluor 647	#A21447, Invitrogen, USA
Donkey anti-rabbit IgG Alexa Fluor 555	#A31572, Invitrogen, USA
Donkey anti-rabbit IgG Alexa Fluor 647	#A31573, Invitrogen, USA

1.2.6. RNAscope *in situ* hybridization	
1x Plus Amplification Diluent	#FP1135, Akoya Biosciences, USA
Cyanine 3 Amplification Reagent	#FP1170, Akoya Biosciences, USA
Cyanine 5 Amplification Reagent	#FP1171, Akoya Biosciences, USA
Probe Mm-Hcn4-C2	#421271, ACD, USA
Probe Mm-Ntm-C1	#489111, ACD, USA
Probe Mm-Smoc2-C1	#318541, ACD, USA
RNAscope® Multiplex TSA Buffer	#322809, ACD, USA
RNAscope® Hydrogen Peroxide	#322381, ACD, USA
RNAscope® Target Retrieval Reagents	#322000, ACD, USA
RNAscope® Protease Plus	#322331, ACD, USA
RNAscope® Wash Buffer Reagents	#310091, ACD, USA

RNAscope® Multiplex Fluorescent Kit v2	#323100, ACD, USA
RNaseOUT	#786-70, G-Biosciences, USA
UltraPure Distilled Water	#10977-015, ThermoFisher, USA

1.2.7. Devices	
Fluorescence Microscope	Axio Imager 2, Zeiss, USA
Light Sheet Microscope	Ultramicroscope II, LaVision Biotec, USA

1.3. Methods

1.3.1. General comments

The following paragraphs noted here, namely “Microdissection of cardiac conduction system components”, “Tissue dissociation into single cell suspensions”, “Single-cell RNA-sequencing of cardiac conduction cells”, and parts of “Bioinformatic analyses”) were performed at Stanford University prior to my arrival. Thus, certain methods described in these paragraphs have been used and performed by Dr. William Goodyer and colleagues in the Sean Wu laboratory setting the ground for my own research and contributions.

1.3.2. Mice

Mice used for all experiments were acquired from Jackson Laboratory (Sacramento, CA). Specifically, wild-type CD1 mice were used. To study embryonic hearts, pregnant female mice were acquired at specific timepoints, pups were dissected at embryonic stages and microdissection of heart tissues was performed microscopically. For scRNA-seq experiments, cardiac conduction system components were microdissected from embryonic day 16.5 (E16.5) mice. Otherwise, animal ages are indicated in each section, respectively. In general, both male and female mice were used at equal numbers for all experiments in order to eliminate sex-dependent biological differences.

1.3.3. Microdissection of cardiac conduction system components

First, murine cardiac conduction tissues had to be precisely isolated for a designed scRNA-seq workflow. In this regard, mice were chosen at E16.5 for the following reasons: 1. Cell-size restrictions of current scRNA-seq devices for adult cardiomyocytes and 2. to gain insight into transcriptomic information not only relevant for the maintenance but also the physiological development of the CCS. Therefore, wild-type, pregnant CD1 mice were obtained, mice were sacrificed, and embryonic mouse hearts were harvested at E16.5. Subsequently, freshly harvested hearts were placed in Hanks balanced salt solution (HBSS) ($Calcium^{+}$, $Magnesium^{+}$) (#14025134, Thermo Fisher) and CCS-dissection was performed microscopically based on anatomical landmarks. HBSS fulfilled the function of both washing off red blood cells/coagulated blood from tissues of interest and to keep the embryonic hearts fresh and in a beating state. Specifically, conduction tissues were microdissected from three very specific zones. Zone I (SAN region) was dissected at the junction of the superior vena cava (SVC) and the right atrium, capturing the SAN and adjacent tissues. Zone II (AVN/His region) was dissected from the heart’s central part, capturing the triangle of Koch at the bottom floor of the right atrium as well as a broad area around it. Finally, zone III (BB/PF region) was captured by dissecting the inner layers of both cardiac ventricles. For each zone, CCS tissues were

dissected from a total of 6 different murine embryos and tissues were pooled in order to increase cell numbers and biological replicates.

1.3.4. Tissue dissociation into single cell suspensions

Dissected tissues were further placed in a microtube (one for each zone) and incubated in 100 µL of 0.25% trypsin (# 15050065, Thermo Fisher) at 37°C for 10 min for a first step of tissue dissociation. Next, 1.4 mL of collagenase A/B (10 mg/mL, #10103586001, #11088807001, Roche) and 20% fetal bovine serum (FBS) (# 16000044, Thermo Fisher) in HBSS (#14025134, Thermo Fisher) was added to the tubes for an additional 20 min of incubation at 37°C. Subsequently, tubes were centrifuged at 1000 rounds per minute (rpm) for 5 min to spin down cells, the supernatant was discarded, and cells were washed in 20% FBS in HBSS. Cells were resuspended to around 600 cells/µL with 0.04% FBS/HBSS solution for processing on the 10x Platform. Methodological descriptions are adapted from from[3].

1.3.5. Single-cell RNA-sequencing of cardiac conduction cells

Capturing of single cells was further performed following the 10X recommended protocol, which can be found on the following webpage: https://support.10xgenomics.com/permalink/user-guide-chromium-single-cell-3-reagent-kits-user-guide-v2-chemistry. In brief, the process started with the generation of Gel Bead-In-EMulsions (GEMs) and barcoding. This way, the 10X technology can index each single cells transcriptome. Post barcoding, primers, Unique Molecular Identifiers (UMI), and poly-dT primer sequences were released to generate cDNA libraries from mRNA transcripts. After further cleanup of broken-down GEMs, cDNA libraries were PCR-amplified, and sequencing-ready libraries were constructed. Finally, constructed libraries were sequenced using Illumina HiSeq 4000.

1.3.6. Bioinformatic analyses

Having produced standard Illumina BCL data, secondary analysis and visualization was first performed using the Cell Ranger pipeline. This way, demultiplexing was performed, genes were both aligned and counted, and first results of single cell expression data were obtained. This way, a first user-friendly overview (including cell clustering, cell type annotation and differential gene expression analysis) was obtained. Secondly, further in-depth bioinformatic analyses were performed. To this end, standard pre-processing procedures were carried out, including quality control measures, cell filtering, data normalization, identification of highly variable features, scaling the data, linear dimensional reduction, and cell clustering. This was performed in Seurat version 2 per Seurat's recommended steps[57]. Default parameters can be recapitulated in a detailed tutorial on the Satija lab website: https://satijalab.org/seurat/archive/v3.2/pbmc3k_tutorial.html. In brief, cells were filtered by the number of individual genes expressed per cell. The threshold used was > 200 genes per cell. This way, most damaged cells were sorted out. Next, data normalization was performed per Seurat's recommended steps. The *y* axis of all ViolinPlots indicates this normalized gene expression. As a standard pre-processing step before PCA, linear transformation ("scaling") was performed, and highly variable features were detected. Finally, differential gene expression analyses were performed for all cell clusters unbiasedly using the FindAllMarker function. To be detected as differentially expressed, genes must be expressed in at least 25% of cells in one of the 2 comparing clusters, and the differential gene expression level must be greater than 25%. For the identification of specific cell types within the dataset, gene expression of well-known cell type-specific marker genes was assessed. Marker genes used

for each cell type were the following: Cardiomyocytes: *Tnni3*, *Tnnt2*, *Myl7*, *Myl2*, *Gja1*, *Nppa*, *Gja5*; nodal: *Hcn4*, *Hcn1*, *Bmp2*, *Kcne1*, *Gjc1*, *Isl1*, *Shox2*, *Hopx*, *Cacna1g*, *Cacna2d2*, *Tbx2*, *Tbx3*, *Tbx5*, *Tbx18*; ventricular conduction system cells: *Gja1*, *Gja5*, *Scn5a*, *Irx3*, *Etv1*, *Id2*, *Hopx*, *Cacna1g*; epicardial cells: *Upk3b*, *Wt1*; endocardial/endothelial cells: *Npr3*, *Plvap*, *Cdh5*, *Pecam1*, *Kdr*, *Fabp4*; coronary smooth muscle cells: *Pdgfrb*, *Myh11*; fibroblasts: *Tcf21*, *Pdgfra*; white blood cells: *Csf1r*.

1.3.7. Immunohistochemistry

Murine CD1 embryonic and postnatal hearts (ages indicated at each figure, respectively) were dissected and rinsed in HBSS (Ca^+/Mg^+) (Gibco, #14025-134) three times. Further, hearts were submersed in 4% paraformaldehyde (PFA) (Fisher, #50-980-487) overnight at 4°C for tissue fixation. Fixed hearts were then rinsed in phosphate-buffered saline (PBS) (#70011-044, Thermo Fisher) 3 times for 15 min to wash off excess PFA and further put in Eppendorf tubes filled with 30% sucrose in 1x PBS overnight at 4°C. The next day, tissues were embedded in Tissue-Plus optimal cutting temperature compound (OCT compound) (Fisher, #23-730-571) and further stored at -80°C for conservation and freezing of tissues. Cryosections were performed at a thickness of 12 µm through the entire heart to capture all CCS components on different slides. Prior to immunostaining, sections were dried for 1 h, rehydrated in 1x PBS, washed three times in PBST (1x PBS + 0.1% Triton X-100) and then blocked (PBST + 0.5% Bovine serum albumin (BSA)) for 1 h at room temperature. Following this, the sections were incubated with primary antibodies diluted in blocking solution (3% BSA in PBS) overnight at 4°C in humid chambers. Primary antibodies were used at 1:100 dilution. The next day, tissue sections were rinsed with PBST three times for 15 minutes and subsequently incubated with secondary antibodies for 2 h at room temperature (covered from light in humid chambers). Secondaries were used at a 1:500 dilution in blocking solution. After additional washing with 1x PBS for 5 minutes three times, the sections were mounted with mounting media containing 4',6-diamidino-2-phenylindole (DAPI) (#H-1200, Vector Laboratories) to stain nuclei. Slides were stored at 4°C covered from light until imaged. All images were taken with the Zeiss Axio Imager 2 microscope. Generally, immediately adjacent slides were used with primary or secondary antibodies alone for negative controls. Modified from[3].

1.3.8. Immunolabeling-enabled three-dimensional imaging of solvent-cleared organs

Immunolabeling-enabled three-dimensional imaging of solvent-cleared organs (iDISCO+) was performed per official iDISCO+ protocol: https://idisco.info/idisco-protocol/. CD1 mouse embryos and hearts of postnatal mice were freshly harvested, washed in HBSS (Ca^+/Mg^+) (Gibco, #14025-134) fixed overnight in 4% paraformaldehyde in 1x PBS (Fisher, #50-980-487) at 4°C. Next, hearts were rinsed in 1x PBS for 15 min 3 times in order to wash off excess PFA and avoid overfixation. Fixed and washed hearts were then stored fully submersed in 1x PBS at 4°C until used. For the iDISCO+ workflow, hearts were first dehydrated in serial dilutions of methanol (#A452-4, Fisher Scientific) in 1x PBS (20%, 40%, 60%, 80%, 100%, 1 h each). Samples were again washed in 100% methanol for 1 h, and then chilled at 4°C for at least 3 h. Overnight, hearts were incubated in 66% dicloromethane (DCM) (#270997, Sigma-Aldrich) in 33% methanol at room temperature (RT) with shaking. The next day, samples were washed twice in 100% methanol at RT, and then cooled down 4°C until hearts were bleached in pre-cooled 5% H_2O_2in methanol (1 volume 30% H_2O_2 to 5 volumes methanol), overnight at 4°C. On day three, hearts were again rehydrated in serial dilutions of methanol in 1x PBS (5 serial dilutions, 1h each with shaking at RT) down to pure PBS. Further, samples were washed in PTx.2 two

times for 1h at RT. From here, all steps were performed in closed 1.5 mL Eppendorf tubes to prevent oxidation. Samples were incubated in iDISCO+ permeabilization solution at 37°C with shaking for two days. After two days, hearts were blocked in iDISCO+ blocking solution at 37°C for another 2 days. Next, samples were incubated with primary antibody in PTwH / 5% DMSO / 3% donkey serum at a 1:200 dilution at 37° for 2 days on a shaker. From this point, a maximum of two samples were combined in one Eppendorf tube. After incubation in primary antibodies, samples were washed in PTwH 4-5 times until the next day at RT on a shaker. The next day, secondary antibodies were prepared in PTwH / 3% donkey serum at a 1:700 dilution, then manually filtered through Nalgene syringe filters before samples were incubated in the secondary antibody solution for two days at 37° on a shaker. From here, hearts were kept covered from light to minimize fluorescence signal quenching. Next, samples were washed in PTwH for 4-5 times until the next day at RT. Now, hearts were again dehydrated in serial dilutions of methanol in PBS series (5 steps, 1 h each, shaking at RT) and left overnight. Lastly, hearts were incubated for 3 h (with shaking) in 66% DCM / 33% methanol at RT, and then in 100% DCM for 15 min twice (with shaking) before final incubation in DiBenzylEther (DBE) (no shaking). The tube was filled almost completely with DBE to prevent sample oxidation. One day after clearing, iDISCO+ samples were imaged using a light sheet microscopy. Entire hearts were scanned at a step-size of 3 µm. Thus, up to 800 images were acquired scanning entire organs. A minimum of 8 biological (different hearts) replicates were used for each immunolabeling approach. In order to reconstruct three-dimensional images from multiple images taken with the light sheet microscope, the interactive 3D image visualization and analysis software Imaris was used. No additional modification tools were used to create 3D images, except otherwise explained. Modified from[3].

1.3.9. RNAscope *in situ* hybridization

The RNAscope® Multiplex Fluorescent v2 Assay allows for high-resolution fluorescence *in situ* hybridization (FISH) and simultaneous visualization of up to three different RNA targets per cell. Following sample pre-treatment, probe hybridization and signal amplification, single RNA transcripts can be visualized as punctate dots. Here the RNAscope® Multiplex Fluorescent Kit v2 (Cat. #323100) was used per manufacturer suggested protocol and the following murine probes were used: Mm-Hcn4-C2 (#421271, ACD), Mm-Smoc2-C1 (#318541, ACD) and Mm-Ntm-C1 (#489111, ACD)[3]. A detailed user manual can be found on the ACD webpage: https://ruo.mbl.co.jp/bio/product/epigenetics/images/rnascope/USM-323100_MultiplexFluorescent_v2_UserManual_Support_04032017.pdf. In brief, slides containing the tissue of interest (12 µm thickness) are washed in 1x PBS for 5 min to remove OCT. Excess liquid is removed and RNAscope® Hydrogen Peroxide (#322381, ACD) is added to cover the entire section. Slides are incubated for 10 min at RT, and carefully washed again in distilled water 3-5 times. Next, slides are dried at RT, and a hydrophobic barrier is drawn closely around tissue sections of interest. Further, slides are placed in the HybEZ™ Slide Rack and 5 drops of RNAscope® Protease Plus (#322331, ACD) is added to each slide. The slide rack is then placed in the HybEZ™ Humidity Control Tray, sealed, and inserted into the HybEZ™ Oven and incubated for 30 min at 40°C. All the following steps which are performed at 40°C are similarly performed in the HybEZ™ Humidity Control Tray and the HybEZ™ Oven. Now, slides are washed 3-5 times in distilled water (#10977-015, Thermo Fisher). Next, excess liquid is removed from slides, 4-6 drops of the probe mix (all probes of interest) are added to entirely cover the slides, and slides are incubated for 2 h at 40°C. After hybridization, slides are washed twice in 1x wash buffer (#310091, ACD). Further, 4-6 drops of RNAscope® Multiplex FL v2 Amp1 is added, and slides are incubated for 30 min at 40°C. Again, slides are washed twice in

1x wash buffer, 4-6 drops of RNAscope® Multiplex FL v2 Amp2 is added and incubated for another 30 min at 40°C. One more time, slides are washed twice in 1x wash buffer, RNAscope® Multiplex FL v2 Amp3 is added, and slides are incubated for 15 min at 40°C. After slides are washed carefully in 1x wash buffer, horseradish peroxidase (HRP) signal is developed by adding HRP-C1 entirely covering the slide. Slides are incubated for 15 min at 40°C. Again, slides are washed for 2 min at RT in 1x wash buffer. Next, 200 µL of the TSA Plus fluorophore is added to each slide at a 1:1000 concentration and slides are incubated for 30 min at 40°C. At this point, the first probe (C1) is developed. To develop more than one probe in different fluorescent channels, slides must be washed for 2 min at RT in 1x wash buffer, slides must be covered with HRP blocker, incubated for 15 min at 40°C and be carefully washed again at RT. Now, the HRP-C2 signal can be developed as already described above for HRP-C1. Similarly, HRP-C3 may be developed. Lastly, slides are carefully washed in 1x wash buffer at RT, excess liquid is removed, and slides are stained with mounting media containing DAPI (#H-1200, Vector Laboratories) and mounted with a coverslip. Slides are sealed with Electron Microscopy Sciences Nail Polish (#72180, Fisher Scientific), stored at 4°C in the dark and imaged the next day.

1.3.10. ScRNA-seq data deposition and GEO database accession number

ScRNA-seq was performed as described in the paragraphs above. The raw scRNA-seq dataset of the developing murine CCS was deposited into the Gene expression omnibus (GEO) database provided by the National Center for Biotechnology Information (NCBI) under accession number GEO: GSE132658. Thus, the entire dataset was made publicly available in its entirety and can be accessed at: https://www.ncbi.nlm.nih.gov/geo/query/acc.cgi?acc=GSE132658.

1.4. Results

1.4.1. Elucidation of genetic markers enriched within the sinoatrial node

Differential gene enrichment analysis was performed comparing gene expression levels in SAN cells (cluster 9 in zone I) to all other cell clusters of zone I, including atrial cardiomyocytes, fibroblasts, epicardial cells, endocardial cells, endothelial cells, neuronal cells and white blood cells (WBC). Among the most enriched genes within cells of cluster 9 (SAN) compared to all other cell types, several genes were found that play well-known roles in SAN development and function, such as Short stature homeobox protein 2 *(Shox2),* Voltage-dependent calcium channel subunit alpha-2/delta-2 (*Cacna2d2*), Bone morphogenetic protein 2 (*Bmp2*), T-box transcription factor 3 (*Tbx3*), Hyperpolarization activated cyclic nucleotide gated potassium channel 4 (*Hcn4*) and Insulin gene enhancer protein ISL-1 (*Isl1*) (**Table 1.1**).

Cluster 9 = SAN cells		
Gene	**Avg Log FC**	***p* value (adj)**
Igfbp5	2.12	2.63E-126
Shox2	1.97	2.22E-308
Smoc2	1.69	5.23E-164
Cacna2d2	1.41	3.30E-224
Bmp2	1.37	1.24E-220
Tbx3	0.77	9.56E-244
Ntm	0.75	4.97E-81
Rgs6	0.60	2.92E-61
Hcn4	0.60	1.29E-247
Cpne5	0.57	2.90E-37
Isl1	0.34	1.03E-192

Table 1.1: Novel genetic markers significantly enriched within sinoatrial node cells
This table presents some of the most highly enriched gene transcripts found within sinoatrial node cells of cluster 9. Well-established conduction-specific genes (*Shox2, Cacna2d2, Bmp2, Tbx3, Hcn4* and *Isl1)* are shown in white, whereas novel genes found in this study (*Igfbp5, Smoc2, Ntm, Rgs6,* and *Cpne5*) are highlighted in green. SAN indicates sinoatrial node; *p*-value (adj): adjusted *p*-value. Modified from[3].

Reinforcing the identification of a true SAN cell cluster within our dataset, all established nodal markers were found to show an increased fold change in gene expression compared to non-conduction cell clusters. Strikingly, in addition to the above-mentioned known SAN markers, differential gene expression analyses uncovered a host of novel gene transcripts highly enriched within cluster 9 cells that have not previously been associated with the CCS. Namely, Copine 5 (*Cpne5*), Regulator of G-protein signaling 6 (*Rgs6*), SPARC-related modular calcium-binding protein 2 (*Smoc2*), Neurotrimin (*Ntm*) and Insulin-like growth factor-binding protein 5 (*Igfbp5*) expression were all found to be highly enriched within SAN cells at statistical significance.

Next, gene expression levels of novel genes were analyzed across all cell types and displayed in violin plot and feature plot format at single cell resolution. These analyses confirmed expression enrichment of novel markers within SAN cells (cluster 9, C9) but also provided additional valuable information regarding their expression within other cell types of the heart (**Figure 1.6**).

Igfbp5 gene expression was, in addition to SAN cells (C9) recognized in a subset of endocardial (C4) and epicardial (C10) cells, *Smoc2* expression was additionally recognized in a subset of fibroblasts (C11) and epicardial (C10) cells, and *Ntm* expression in neuronal cells (C14). Thus, besides lower gene expression in other cardiac cell types, the novel genes *Cpne5, Rgs6, Smoc2, Ntm* and *Igfbp5* demonstrate highest enrichment in SAN cells of cluster 9 and thus demonstrate novel genetic markers for the identification and characterization of SAN cells.

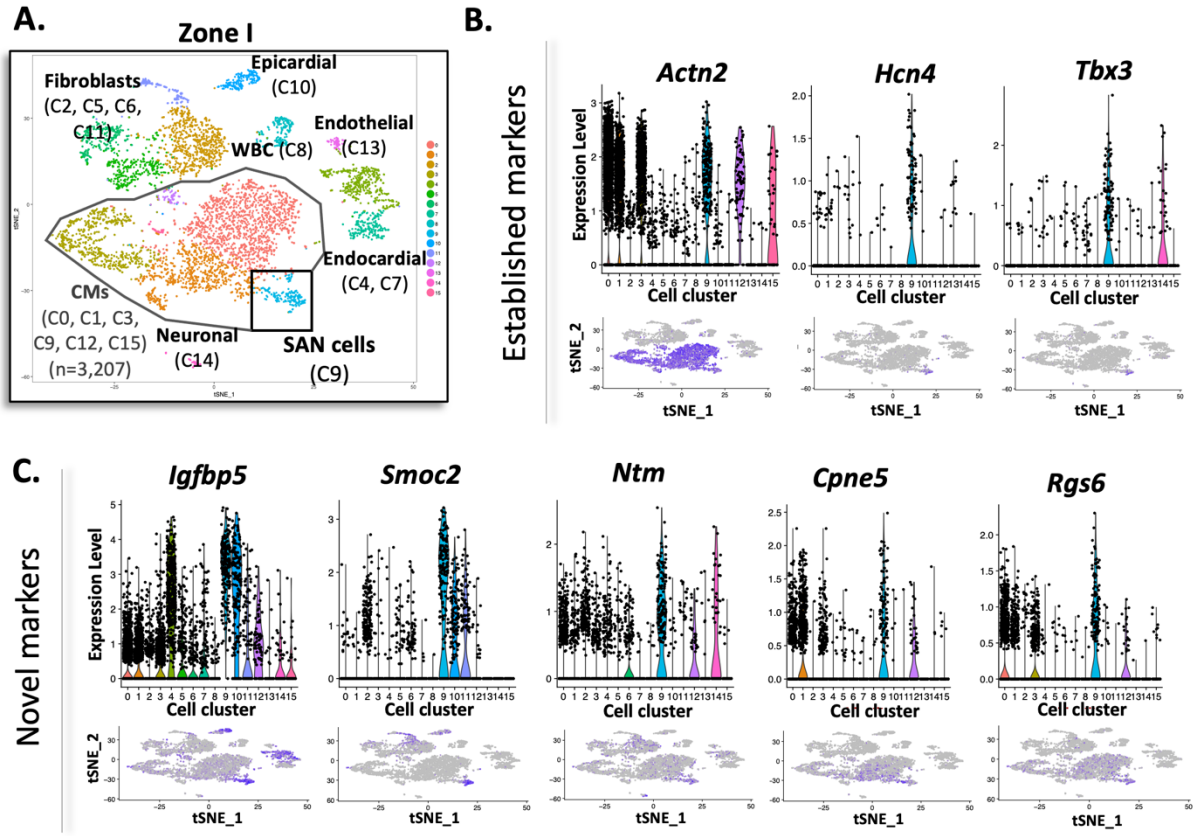

Figure 1.6: Expression levels of novel genetic markers across all cell types in zone I
A. T-distributed stochastic neighbor embedding (t-SNE) plot for zone I with all cell clusters labeled by their respective cell type. All feature plots displayed in B. and C. refer to this t-SNE plot. **B.** Established cardiomyocyte (*Actn2*$^{+}$) and nodal (*Hcn4*$^{+}$, *Tbx3*$^{+}$) markers visualized by ViolinPlots (top) and FeaturePlots (bottom) demonstrate cluster 9 as a sinoatrial node (SAN) cell cluster. **C.** *Igfbp5, Smoc2, Ntm, Cpne5* and *Rgs6* gene expression visualized by ViolinPlots (top) and FeaturePlots (bottom) across all cell types captured in zone I demonstrates high enrichment of novel markers in SAN cell cluster 9. CM indicates cardiomyocyte; WBC: white blood cells. Modified from[3].

Moreover, subcluster analyses were performed of all SAN cells in cluster 9. As a result, SAN cells were unbiasedly split into two distinct cell clusters displaying core SAN cells in one cell cluster and SAN Tz in the other (**Figure 1.7A**). Consistent with our current understanding of transitional cells as a hybrid cell type between conduction cells and working myocytes[26], the gold standard conduction marker *Hcn4* was found to be expressed at a higher level within the cSAN as compared to SAN Tz. Further reinforcing the true capture of two distinct cell types, atrial cardiomyocyte genes such as *Gja5* were found fully absent from the cSAN, however lowly expressed within SAN Tz (**Figure 1.7B**), as expected. Interestingly, enrichment of all five novel genes (*Cpne5, Rgs6, Smoc2, Ntm* and *Igfbp5)* was found not only within the cSAN, but additionally in cells representing SAN Tz (**Figure 1.7C**).

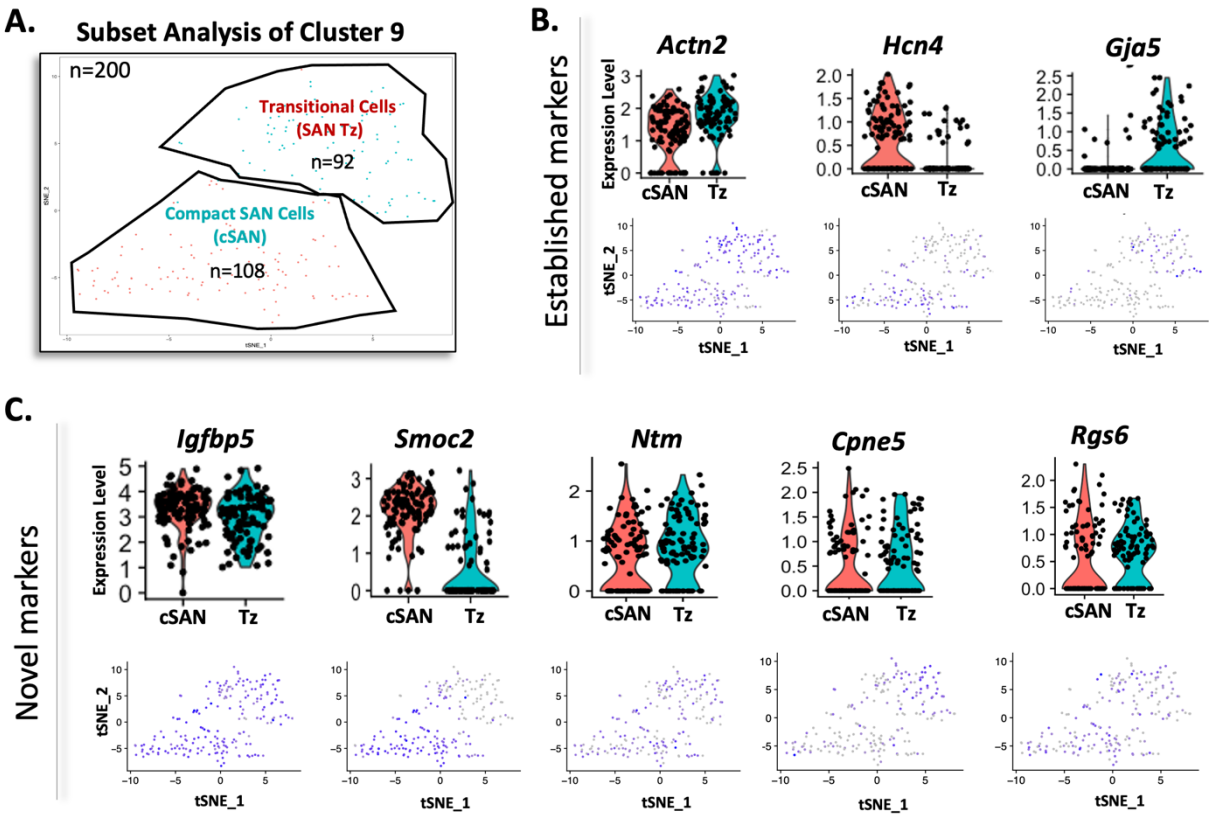

Figure 1.7: Subset analyses reveal enrichment of Igfbp5, Smoc2, Ntm, Cpne5 and Rgs6 in sinoatrial node transitional cells

A. T-distributed stochastic neighbor embedding (t-SNE) plot represents subcluster analysis of cluster 9 cells demonstrating 2 distinct cell subclusters consistent with compact sinoatrial node (SAN) cells (cSAN) and transitional cells (Tz). All feature plots displayed in B. and C. refer to this t-SNE-plot. **B.** ViolinPlots (top) and FeaturePlots (bottom) for key cardiomyocyte (*Actn2*), nodal (*Hcn4*) and atrial cardiomyocyte (*Gja5)* markers. **C.** *Igfbp5, Smoc2, Ntm, Cpne5* and *Rgs6 g*ene expression visualized by ViolinPlots (top) and FeaturePlots (bottom). Modified from[3].

Having revealed five novel genetic markers, which are highly enriched within the compact SAN and SAN transitional cells, validation of our findings was next sought through immunostaining of murine heart sections. In this regard, high resolution fluorescence *in situ* hybridization (FISH) and immunohistochemistry (IHC) was next performed in serial sections of wild-type, postnatal day 0 (P0) murine hearts (**Figure 1.8**).

The gold standard conduction cell marker Hcn4 was used to delineate the compact SAN as a positive control (red). Interestingly, precise co-labeling of the cSAN (*Hcn4^{+}/novel marker^{+}*) by all five novel genetic markers was found, thus proving highly exclusive expression of novel markers within the cSAN and absence from the atrial myocardium. Furthermore, not only the cSAN was precisely labeled, but highly specific cell clusters of transitional cells were additionally found at the junction between the cSAN and the surrounding atrial myocardium (*Hcn4^{-}/novel marker^{+}*) to be labeled by novel genetic markers. Of note, while *Igfbp5, Smoc2* and *Ntm* gene expression was recognized within minor non-conduction cell types (**Figure 1.6**) in our scRNA-seq data, expression could not be detected in these other cell types following FISH or IHC.

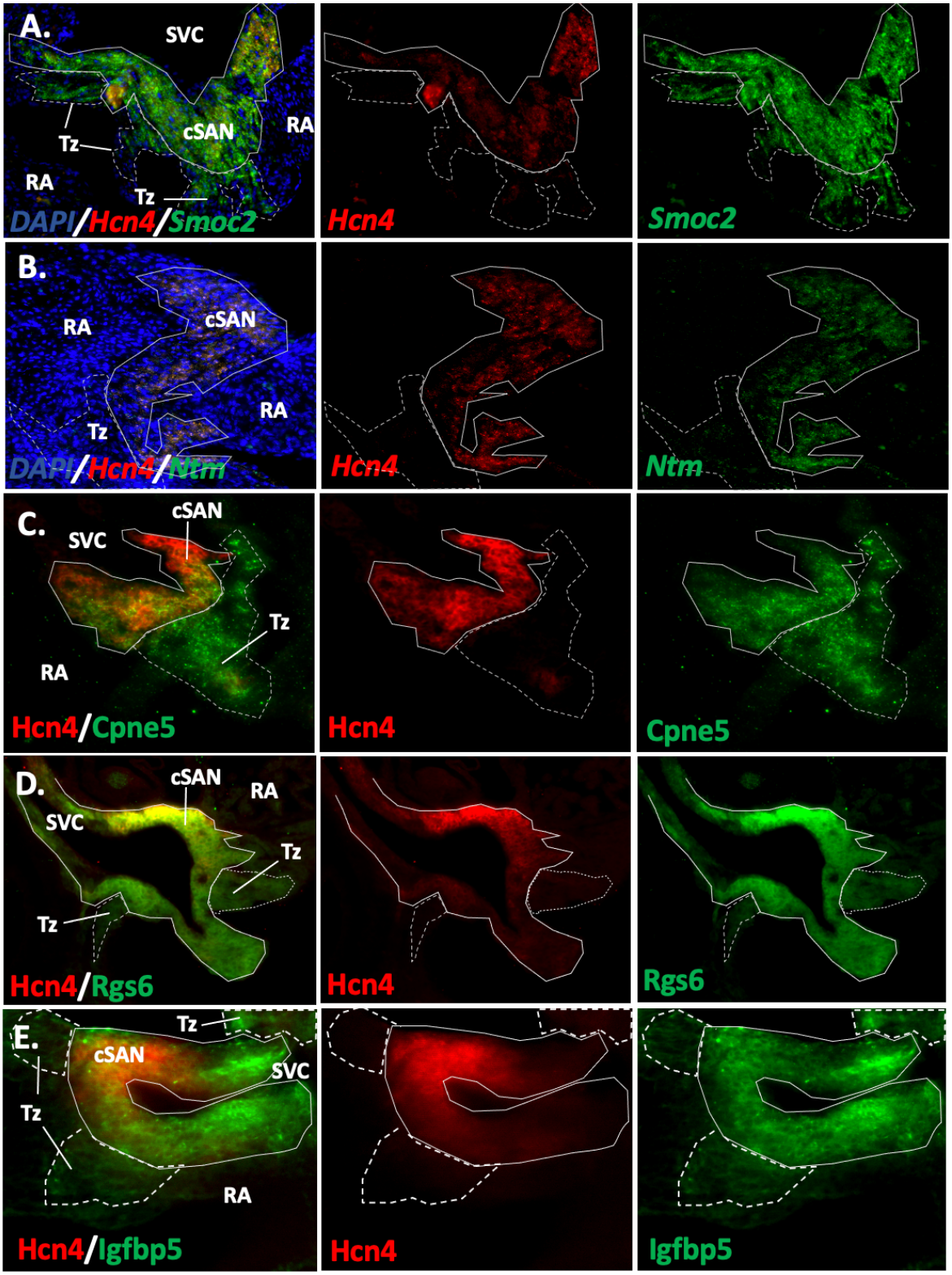

Figure 1.8: Immunohistochemistry and fluorescence in situ hybridization confirm the enrichment of novel genetic markers in sinoatrial node cells of murine hearts

A, B: High resolution fluorescence RNA *in situ* hybridization (RNAscope) targeting *Hcn4* (red punctae) and *Smoc2/Ntm* (green punctae) mRNA within heart sections of postnatal day 0 (n=3), wild-type mice. DAPI (blue). **C, D, E:** Whole mount immunostaining and lightsheet imaging (iDISCO+) of (n=5) wild-type murine hearts. The compact sinoatrial node (cSAN) is delineated by high expression of Hcn4 protein (red) and Cpne5, Rgs6 or Igfbp5 protein (green). Solid lines depicting cSAN cells ($Hcn4^{+}$/novel $marker^{+}$) and dashed lines delineate transitional cells (Tz) ($Hcn4^{-}$/novel $marker^{+}$). RA indicates right atrial myocardium, SVC: superior vena cava. Modified from[3].

In summary, the discovery of *Cpne5, Rgs6, Smoc2, Ntm* and *Igfbp5* provides five novel markers of not only the cSAN but also the previously elusive SAN Tz cells, as demonstrated by scRNA-seq at the mRNA level and validated by IHC/FISH in murine heart sections.

1.4.2. Novel genetic markers found enriched within the atrioventricular node and His bundle

Detailed gene expression analysis was performed comparing cluster 4 cells (AVN/His cell cluster) to all other cell clusters of zone II. Well-established AVN/His marker genes showed robust enrichment in cluster 4 cells at statistical significance, namely Potassium voltage-gated channel subfamily E member 1 (*Kcne1*), Voltage-dependent calcium channel subunit alpha-2/delta-2 (*Cacna2d2*), Bone morphogenetic protein 2 (*Bmp2*), T-box protein 5 (*Tbx5*), G protein-activated inward rectifier potassium channel 4 (*Kcnj5*) and Voltage-dependent calcium channel subunit alpha-1g (*Cacna1g*) (**Table 1.2**).

Strikingly, significant fold changes in gene expression were additionally detected for the novel genes *Igfbp5, Cpne5, Ntm* and *Rgs6*, which were found to be enriched within the cSAN and SAN Tz.

Cluster 4 = AVN/His cells		
Gene	**Avg Log FC**	***p* value (adj)**
Slc22a1	1.72	2.22E-308
Igfbp5	1.19	1.49E-120
Kcne1	0.98	3.59E-75
Cacna2d2	0.88	2.22E-308
Cpne5	0.73	2.22E-308
Ntm	0.55	1.20E-101
Bmp2	0.55	3.53E-57
Tbx5	0.54	2.07E-110
Kcnj5	0.42	4.33E-102
Rgs6	0.39	9.75E-153

Table 1.2: Novel markers enriched in atrioventricular node and His bundle cells
This table presents some of the most highly enriched gene transcripts found within atrioventricular node (AVN)/His bundle (His) cells of cluster 4 in zone II. Well-established conduction-specific genes (*Kcne1, Cacna2d2, Bmp2, Tbx5, Kcnj5)* are shown in white, whereas novel genes (*Igfbp5, Cpne5, Ntm* and *Rgs6*) are highlighted in green. *p*-value (adj) indicates adjusted *p*-value. Modified from[3].

Further, gene expression levels of known AVN/His markers (*Hcn4, Cacna2d2*) and novel AVN/His marker genes were analyzed across all cell types contained within zone II and displayed in violin plot and feature plot format at single cell resolution (**Figure 1.9**).

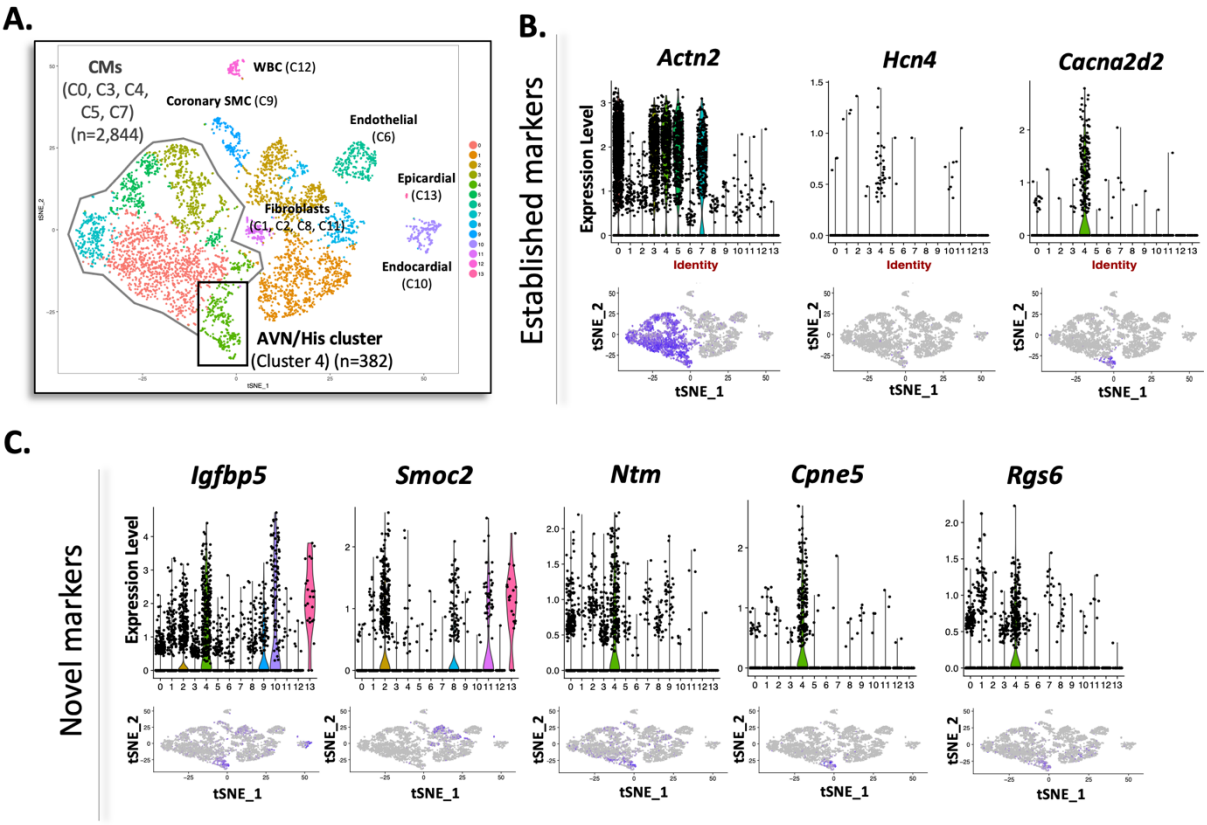

Figure 1.9: Gene expression levels of novel markers across all cell types in zone II

A. T-distributed stochastic neighbor embedding (t-SNE) plot for zone II cells including labeling of all cell types from this region. All feature plots displayed in B. and C. refer to this t-SNE plot. **B.** Established cardiomyocyte (*Actn2*$^{+}$) and nodal (*Hcn4*$^{+}$, *Cacna2d2*$^{+}$) markers visualized by ViolinPlots (top) and FeaturePlots (bottom) demonstrate cluster 4 as a true atrioventricular node (AVN)/His bundle (His) cell cluster. **C.** *Igfbp5, Smoc2, Ntm, Cpne5* and *Rgs6 g*ene expression visualized by ViolinPlots (top) and FeaturePlots (bottom) across all cell types captured in zone II. CM indicates cardiomyocyte; SMC: smooth muscle cells; WBC: white blood cells. Modified from[3].

This analysis demonstrates cluster 4 as a true nodal cell population (*Actn2*$^{+}$, *Hcn4*$^{+}$, *Cacna2d2*$^{+}$). Regarding new AVN/His markers, *Igfbp5, Cpne5, Rgs6* and *Ntm* gene expression were additionally found to be enriched and largely restricted to AVN/His conduction cells in cluster 4 as compared to all other cell types. Interestingly, the SAN-enriched gene *Smoc2* was found absent from cluster 4 cells, suggestive of an SAN-specific marker as opposed to a pan-CCS marker.

Subsequently, subcluster analysis was performed on conduction cells (C4) in zone II (**Figure 1.10**). While *Hcn4* expression is exclusively found in the cAVN, the CCS transcription factor *Tbx3* was detected in the cAVN, His and nodal AV rings (**Figure 1.10B**), as previously described[58]. *Gja1* on the other hand, a known gene encoding a gap junction protein in the myocardium[59], was indeed found absent from the cAVN, His and NAVR, further reinforcing true subcluster identification. Interestingly, when analyzing novel CCS-enriched genes in each subcluster, *Cpne5* enrichment was found not only within the cAVN and His bundle, but also in the nodal AV rings and the atrial transitional zone (**Figure 1.10C**).

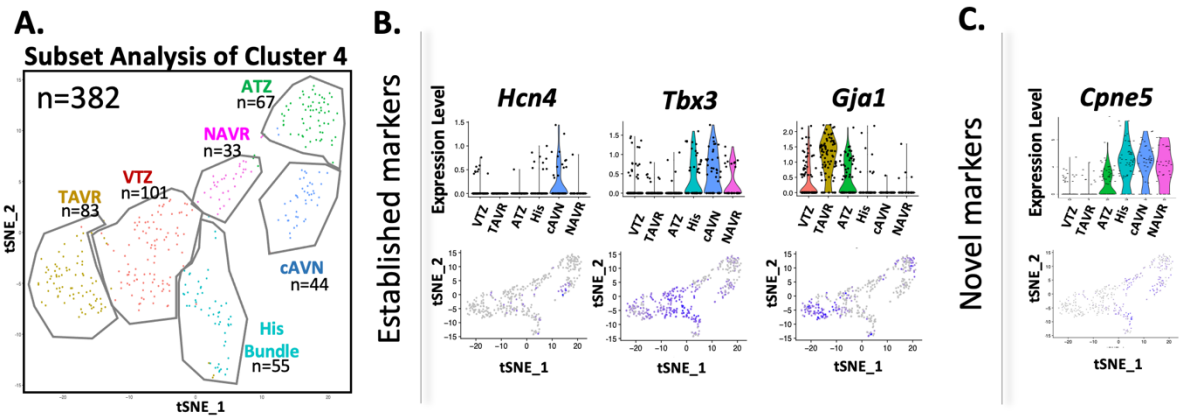

Figure 1.10: Subset analyses reveal Cpne5 enrichment in transitional cells of the atrioventricular node and His bundle

A. T-distributed stochastic neighbor embedding (t-SNE) plot represents subcluster analysis of cluster 4 cells demonstrating 6 distinct cell subclusters consistent with transitional AV rings (TAVR), ventricular transitional zone (VTZ), His bundle (His), nodal AV rings (NAVR), compact AVN (cAVN) and atrial transitional zone (ATZ). All feature plots displayed in B. and C. refer to this t-SNE plot. **B.** ViolinPlots (top) and FeaturePlots (bottom) demonstrating typical nodal and myocardial gene expression across VTZ, TAVR, ATZ, His, cAVN and NAVR. **C.** *Cpne5 g*ene expression visualized by ViolinPlot (top) and FeaturePlot (bottom) demonstrates *Cpne5* gene expression in the ATZ, His, cAVN and NAVR. Modified from[3].

Moreover, using high resolution fluorescence *in situ* hybridization and whole mount immunostaining (iDISCO+) the expression pattern of novel AVN-marker genes (*Cpne5*, *Rgs6, Ntm* and *Igfbp5*) was successfully validated in serial wild-type murine heart sections (**Figure 1.11**). In this regard, Igfbp5, Rgs6 and Cpne5 protein expression (iDISCO+), as well as *Ntm* mRNA expression (FISH) was found highly present within CCS structures (internodal tracts, AVN and His) but fully absent from non-CCS cell types. Interestingly and consistent with our scRNA-seq dataset, the novel SAN-enriched gene *Smoc2* (**Table 1.1**) was clearly absent from the AVN (**Figure 1.11D**). Of note, while *Igfbp5* gene expression was additionally recognized in fibroblasts (C2), coronary smooth muscle cells (C9), endocardial (C10) and epicardial and (C13) cells (**Figure 1.9**) at low levels at the mRNA level, Igfbp5 protein expression could not be found in these cell types by immunostaining. Cpne5 protein was clearly detected in the compact AVN, and additionally in internodal tracts, as well as nodal AV rings in 2D sections (**Figure 1.11C**), consistent with data of our subcluster analysis (**Figure 1.10**).

In summary, this is the first study to analyze the transcriptional landscape of the compact AVN, His bundle and all associated transitional cell types in this region at single cell resolution. This study has revealed and validated four novel genes, namely *Cpne5, Rgs6, Ntm* and *Igfbp5,* to be highly enriched in the AVN. Additionally, *Cpne5* presents the first marker labeling AVN Tz (cAVN, His, ATZ and NAVR) in murine hearts.

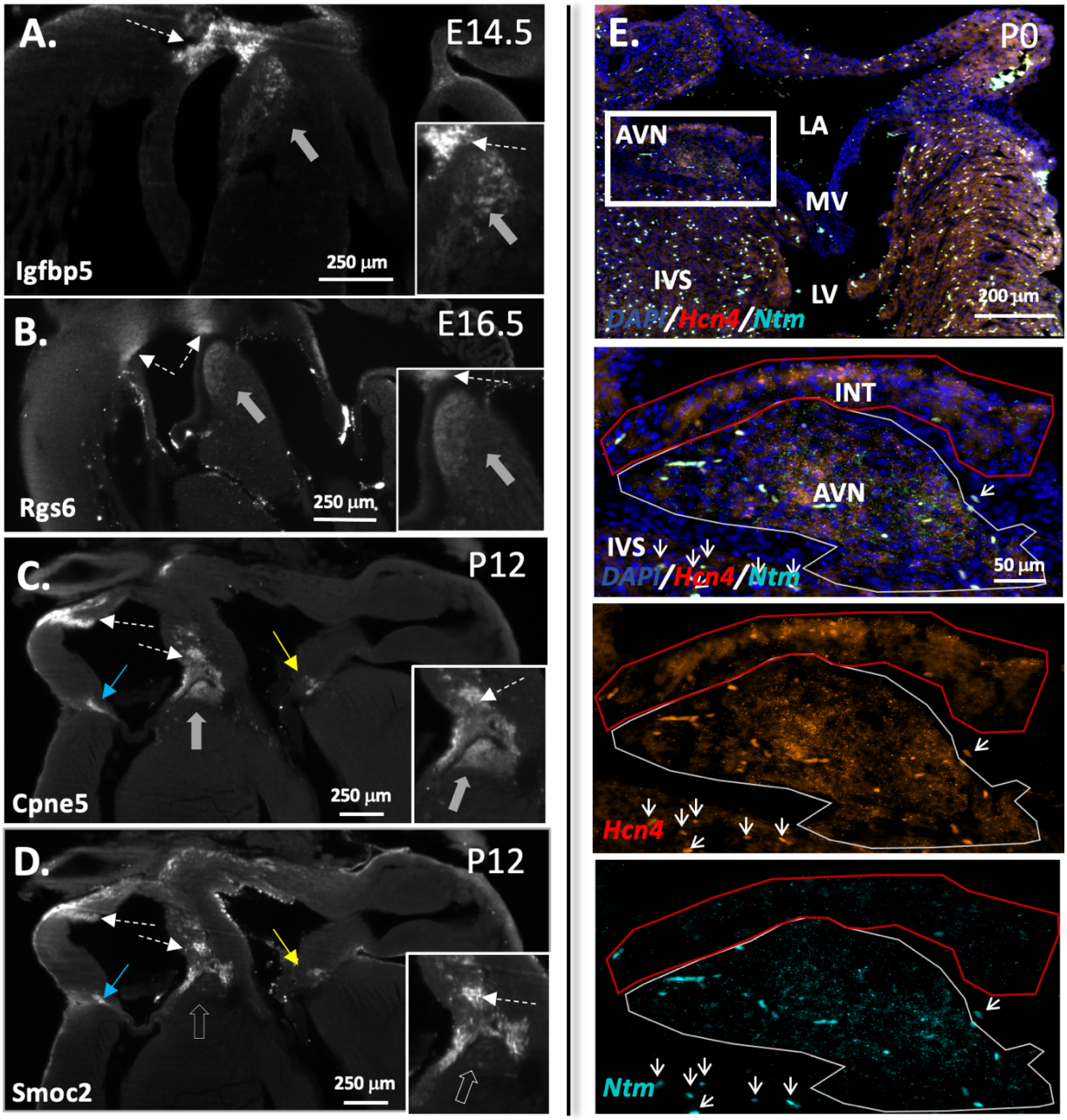

Figure 1.11: iDisco+ and fluorescence in situ hybridization confirm enrichment of novel genetic markers in the atrioventricular node of murine hearts

A. Igfbp5 immunostaining (white) per iDISCO+ protocol and lightsheet imaging in whole E14.5 hearts confirms Igfbp5 enrichment within the AVN. Inset showing an enlarged area of AVN region. **B.** Rgs6 immunostaining (white) per iDISCO+ protocol and lightsheet imaging in whole E16.5 hearts confirms Rgs6 expression within the AVN. Inset showing an enlarged area of AVN region. **C**,**D.** The same postnatal day 12 (P12) heart co-immunostained for Cpne5 (C.) and Smoc2 (D.) protein (white). Insets show a $Cpne5^{+}$ (grey arrow) but $Smoc2^{-}$ (empty white arrow) AVN. Additionally, both novel proteins are found in INT and nodal AV rings. **E.** P0 hearts (AVN and surrounding cardiac structures) labeled for *Hcn4* (red punctae) and *Ntm* (cyan punctae) using fluorescence RNA *in situ* hybridization. Uppermost picture: overview. Below: magnification of the boxed AVN, surrounding internodal tracts (INT) (above) and ventricular cardiomyocytes (below) of the interventricular septum (IVS) are labeled. Solid white lines demarcating the AVN, solid red lines demarcate INT. Larger brightly-stained objects (examples noted by white arrows) in both red and green channels represent autofluorescence from red blood cells (yellow in merge photos). True fluorescence *in situ* hybridization signal is represented by small punctae in either cyan (*Ntm*) or red (*Hcn4*). LA, left atrium; LV, left ventricle; MV, mitral valve; IVS, interventricular septum. Grey arrows: AVN, white arrows: internodal tracts; blue arrows: right AV ring bundle; yellow arrows: left AV ring bundle. Modified from[3].

1.4.3. Discovery of genetic markers enriched within the ventricular conduction system

Differential gene expression was assessed comparing PF cells in cluster 13 to all other cell clusters of zone III. Robust enrichment of well-established PF genes was recognized in cluster 13, including Voltage-dependent calcium channel subunit alpha-2/delta-2 (*Cacna2d2*), Gap junction protein alpha 5 (*Gja5*), ETS variant transcription factor 1 (*Etv1*), Sodium channel protein type 5 subunit alpha (*Scn5a*), Potassium channel subfamily K member 3 (*Kcnk3*), Semaphorin 3A (*Sema3a*), DNA-binding protein inhibitor ID-2 (*Id2*) and Iroquois-class homeodomain protein IRX-3 (*Irx3*). Interestingly, in-depth data analyses have further revealed significant enrichment of the novel genes *Igfbp5, Cpne5* and *Ntm* within PF cells of cluster 13 (**Table 1.3**).

Cluster 13 = PF cells		
Gene	**Avg Log FC**	***p* value (adj)**
Cacna2d2	1.21	2.22E-308
Gja5	0.97	1.17E-183
Igfbp5	0.96	1.11E-100
Etv1	0.89	6.67E-105
Scn5a	0.76	4.81E-86
Cpne5	0.68	2.22E-308
Kcnk3	0.64	1.57E-58
Ntm	0.61	6.32E-110
Sema3a	0.58	7.49E-184
Id2	0.58	2.49E-39
Irx3	0.51	1.89E-119

Table 1.3: Novel gene transcripts found to be enriched in Purkinje fiber cells
This table presents some of the most highly enriched genes within Purkinje fiber (PF) cells of cluster 13 in zone III. Well-established conduction-specific genes (*Cacna2d2, Gja5, Etv1, Scn5a, Kcnk3, Sema3a, Id2, Irx3)* are shown in white, whereas novel genes (*Igfbp5, Cpne5* and *Ntm*) are highlighted in green. *p* value (adj) indicates adjusted *p*-value. Modified from[3].

Further, gene expression analysis across all cell types captured in zone III was performed and results are displayed in violin plot and feature plot format at single cell resolution (**Figure 1.12**). While *Ntm* and *Cpne5* expression was found highly exclusive to bundle branch and Purkinje fiber cells in zone III, the novel gene *Igfbp5* showed significant enrichment both in Purkinje fibers, and additionally in a subset of fibroblasts (C4), coronary smooth muscle cells (C9) and endocardial cells (C11).

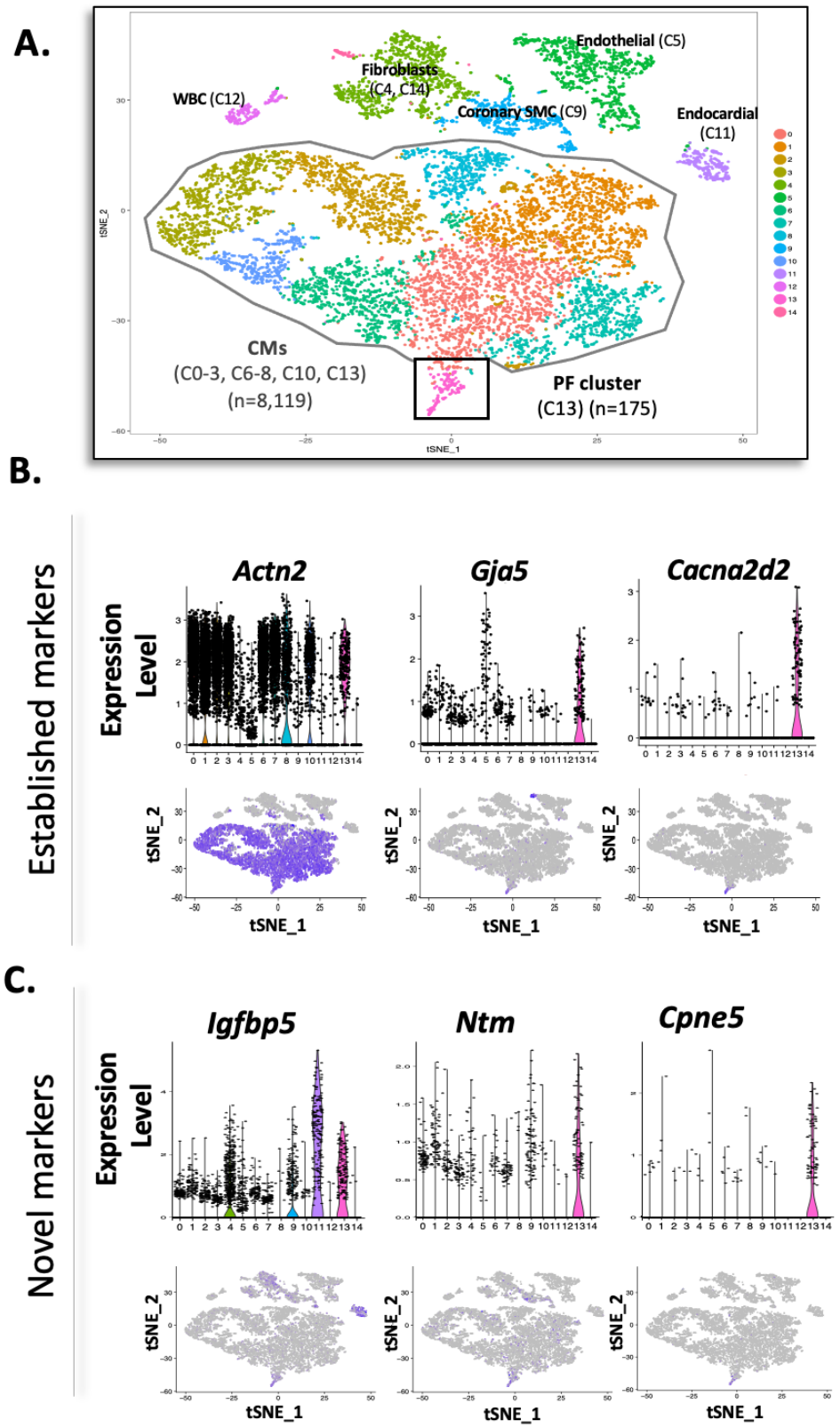

Figure 1.12: Igfbp5, Ntm and Cpne5 gene expression levels across cell types in zone III

A. T-distributed stochastic neighbor embedding (t-SNE) plot for zone III cells with all cell types labeled. All feature plots displayed in B. and C. refer to this t-SNE plot. **B.** Established cardiomyocyte (CM) (*Actn2*$^{+}$) and nodal (*Gja5*$^{+}$, *Cacna2d2*$^{+}$) markers visualized by ViolinPlots (top) and FeaturePlots (bottom). **C.** *Igfbp5, Ntm,* and *Cpne5 g*ene expression visualized by ViolinPlots (top) and FeaturePlots (bottom) across all cell types captured in zone III. CM indicates cardiomyocyte; SMC: smooth muscle cells; WBC: white blood cells. Modified from[3].

Moreover, subset analysis was performed on all cells in cluster 13. As a result, two distinct cell clusters representing standard PF cells and transitional cells could be distinguished. Both cell types are specialized heart muscle cells and hence show a cardiomyocyte signature (*Tnni3*$^{+}$). However, whereas PF are characterized by high *Gja5* and lower *Gja1* expression, PF Tz show only low *Gja5* and much higher *Gja1* expression, as expected[44,59] (**Figure 1.13**). Interestingly, the novel conduction cell marker *Ntm* was revealed to be enriched not only in the PF cell cluster, but additionally in PF Tz.

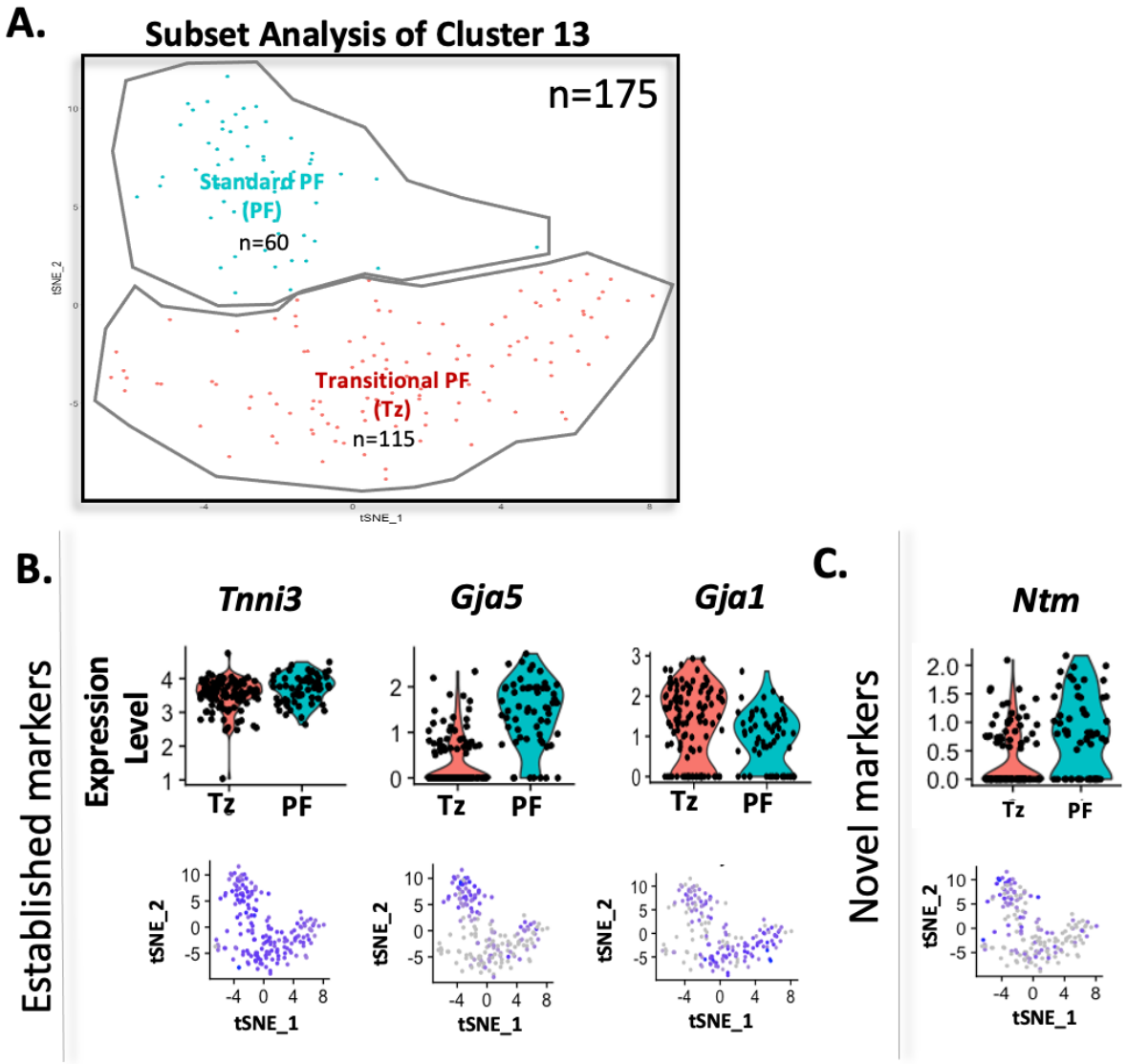

Figure 1.13: Subset analyses reveal Ntm enrichment in Purkinje fiber transitional cells
A. T-distributed stochastic neighbor embedding (t-SNE) plot represents subcluster analysis of cluster 13 cells demonstrating 2 distinct subclusters consistent with standard Purkinje fiber cells (PF) and transitional cells (Tz). All feature plots displayed in B. and C. refer to this t-SNE plot. **B.** ViolinPlots (top) and FeaturePlots (bottom) for key cardiomyocyte (*Tnni3, Gja1*) and nodal (*Gja5*) markers. **C.** *Ntm* gene expression visualized in a ViolinPlot (top) and FeaturePlot (bottom). Modified from[3].

Further, immunostaining of wild-type murine heart sections has validated *Igfbp5* and *Cpne5* gene expression in the PF system (**Figure 1.14**). Additionally, high resolution *in situ* hybridization (RNAscope) proved robust *Ntm* labeling of both standard Purkinje fiber cells as well as PF Tz in murine heart sections for the first time (**Figure 1.14C**). A single subendocardial

layer of proper Purkinje fibers (*Hcn4*$^{+}$/*Ntm*$^{+}$) was clearly outlined by the gold-standard conduction cell marker *Hcn4*. A sheath of transitional cells (*Hcn4*$^{-}$/*Ntm*$^{+}$) was found right adjacent to the proper PF system bridging Purkinje fibers to the ventricular myocardium (**Figure 1.14C**). Thus, the discovery of *Ntm* provides the first known genetic marker delineating PF Tz at the Purkinje fiber-myocyte junction.

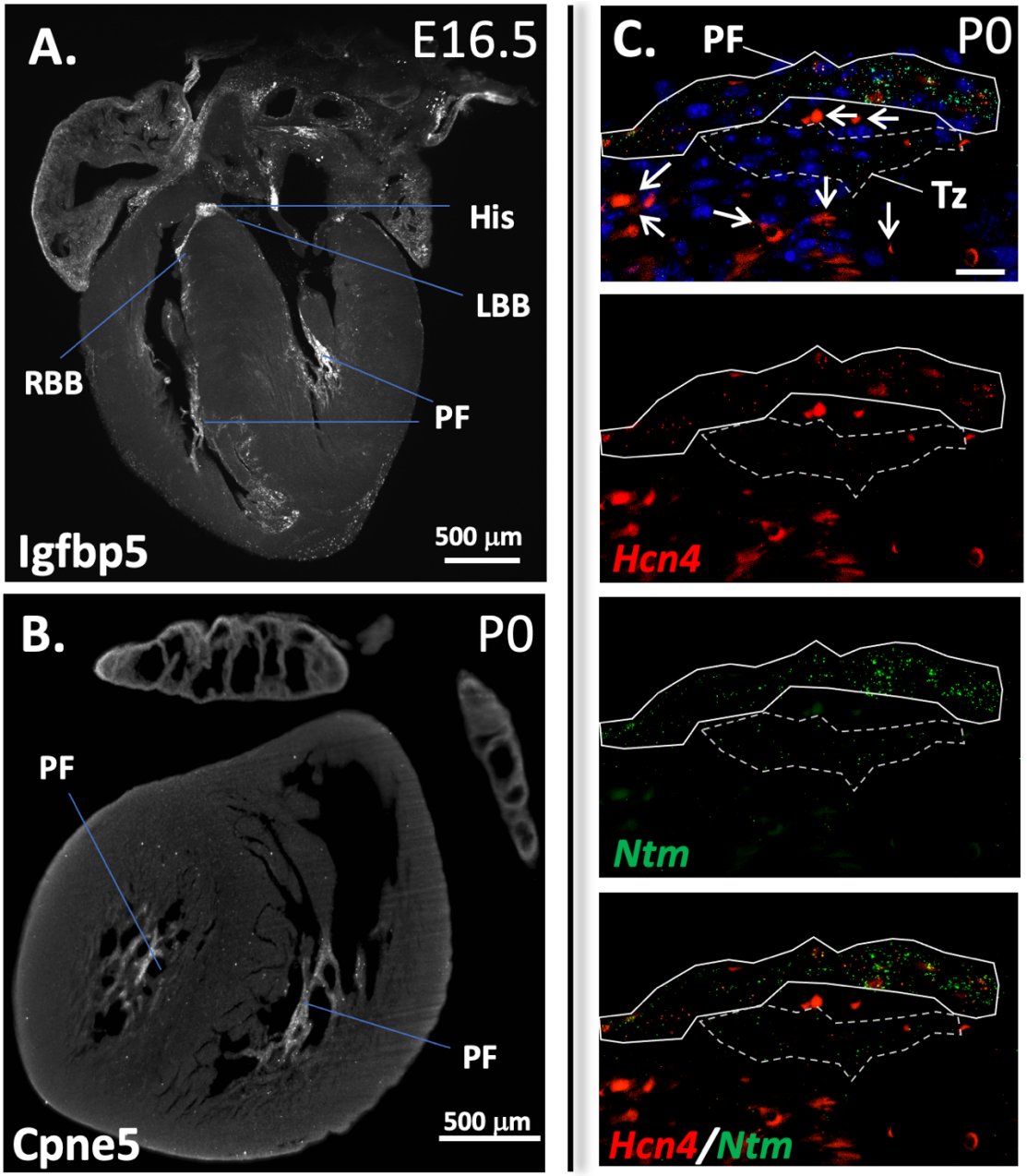

Figure 1.14: Immunohistochemistry and fluorescence in situ hybridization reveal Igfbp5, Cpne5 and Ntm enrichment in the Purkinje fiber system of murine hearts

A, B: Immunolabeling-enabled three-dimensional imaging of solvent-cleared organs (iDISCO+) and lightsheet imaging of wild-type murine hearts showing Igfpb5 (embryonic day 16.5, n=5) and Cpne5 (postnatal day 0 (P0), n=5) protein expression in white. **C:** Fluorescence *in situ* hybridization targeting *Hcn4* (red punctae) and *Ntm* (green punctae) mRNA expression within Purkinje fiber (PF) cells and transitional PF cells (Tz) within P0 mouse heart sections (n=3). DAPI (blue). Solid line depicting standard PF cells (*Hcn4*$^{+}$/*Ntm*$^{+}$) and dashed line showing Tz cells (*Hcn4*$^{-}$/*Ntm*$^{+}$). Beyond these borders are ventricular myocardial cells (*Hcn4*$^{-}$/*Ntm*$^{-}$). Larger brightly stained objects (examples noted by white arrows) in both red and green channels represent autofluorescence from red blood cells. True RNAscope fluorescence *in situ* hybridization signal is represented by small punctae in either green (*Ntm*) or red (*Hcn4*). LBB indicates left bundle branch, RBB: right bundle branch. Modified from[3].

In summary, this study elucidated *Cpne5, Rgs6, Smoc2, Ntm* and *Igfbp5* to be five novel markers highly enriched within individual components of the CCS. In addition to core conduction system components (e.g. cSAN, cAVN, His, BB, PF) some of these markers additionally demonstrate validated genetic markers for the identification and characterization of previously elusive transitional cells in all components of the CCS for the first time.

1.4.4. Demonstration of the precise 3D architecture of sinoatrial node transitional cells

Immunolabeling-enabled three-dimensional imaging of solvent-cleared organs (iDISCO+) followed by lightsheet imaging is a cutting-edge imaging technique that allows for the three-dimensional image acquisition and volumetric analysis of immunolabeled structures in whole organs. The discovery of the first markers labeling SAN Tz, including *Cpne5, Igfbp5, Ntm, Rgs6* and *Smoc2* were here used to determine the exact anatomical localization of previously elusive SAN Tz in three dimensions. A designed iDISCO+ workflow (**Figure 1.15**) was performed using anti-Rgs6 antibodies allowing for high-resolution three-dimensional imaging of the SAN region in whole hearts.

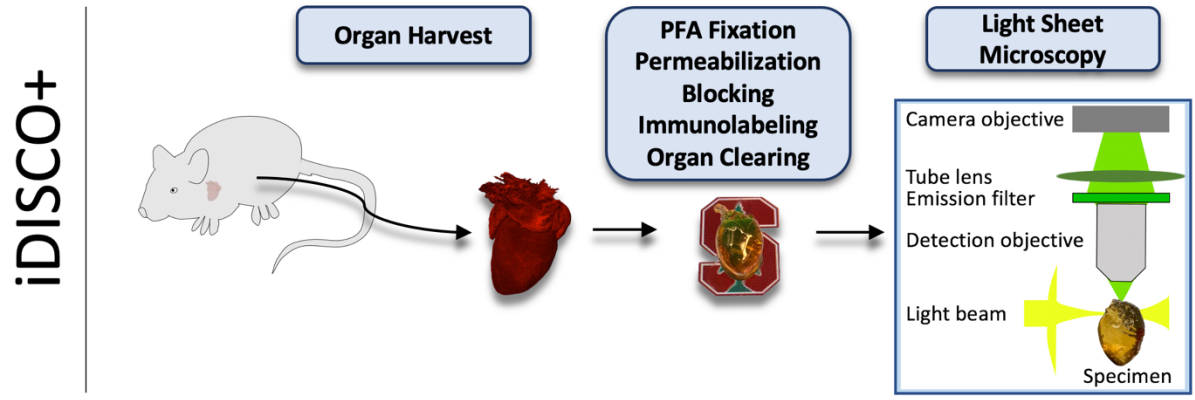

Figure 1.15: iDISCO+ workflow
Schematic representation of the iDISCO+ workflow including harvest of intact mouse hearts, followed by paraformaldehyde (PFA) fixation, permeabilization, blocking, immunolabeling and whole organ clearing. Visualization was performed using light sheet microscopy. Modified from[3].

Post immunostaining and organ clearing, up to 500 single images were acquired at 3 µm thickness through the entire SAN region using light sheet microscopy. Further, three-dimensional images were reconstructed using the interactive microscopy analysis software Imaris. As a result, the cSAN and SAN transitional cells were successfully visualized in 3D in intact hearts (**Figure 1.16**). Here, the comma-shaped compact SAN is outlined in red by Hcn4 immunostaining. Additionally, the novel marker Rgs6 was used to label the entire SAN including SAN Tz. Thus, $Hcn4^{-}/Rgs6^{+}$ (green) cells clearly illustrate pure SAN Tz populations in three dimensions for the first time.

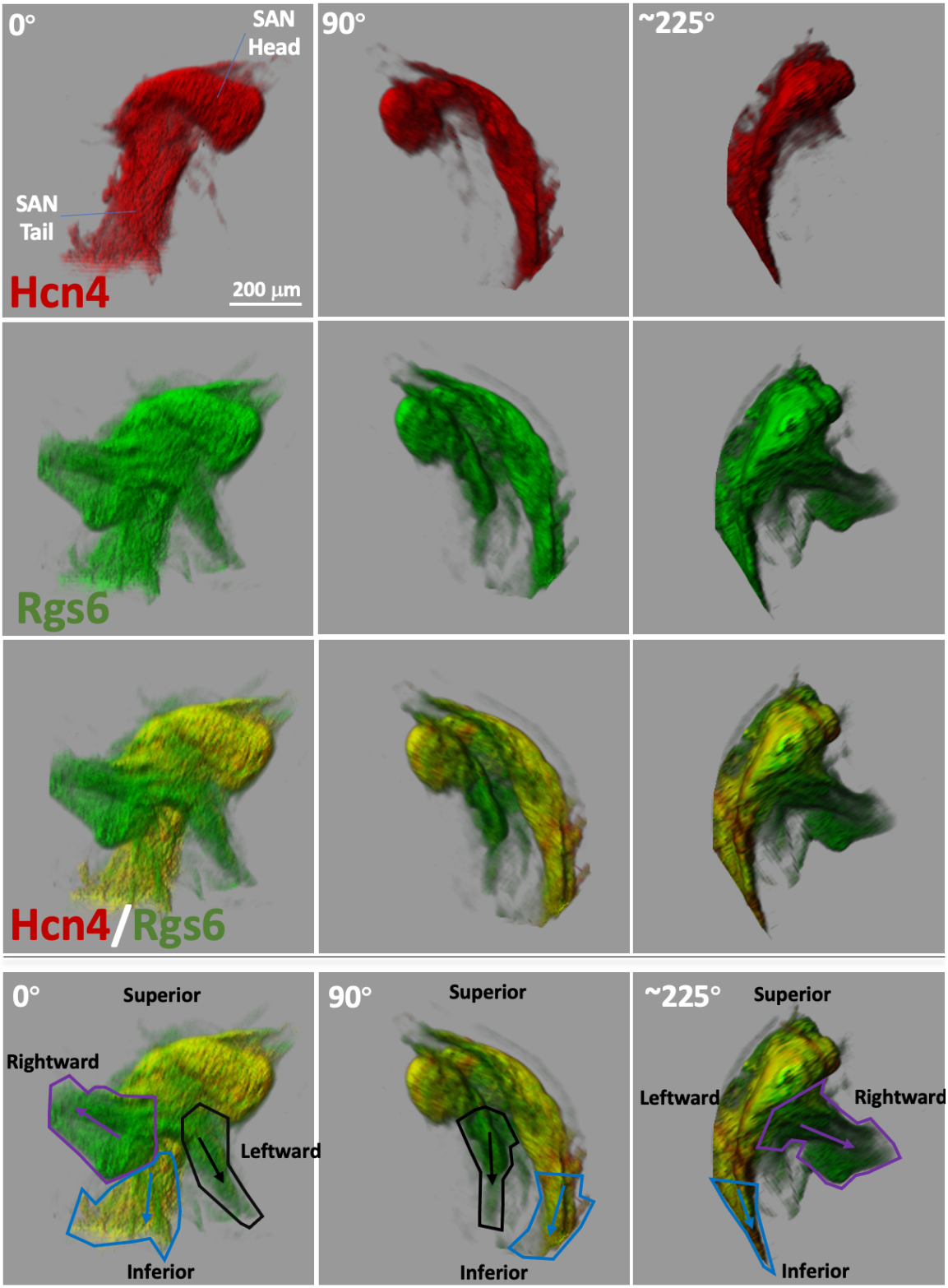

Figure 1.16: Three-dimensional architecture of sinoatrial node transitional cells
Immunolabeling-enabled three-dimensional imaging of solvent-cleared organs (iDISCO+) cleared wild-type, intact sinoatrial nodes (SAN) (6.3x magnification) from embryonic day 16.5 (E16.5) murine hearts co-immunolabeled for Hcn4 (red) and Rgs6 (green) protein. SAN is shown at 3 angles of view (0°, 90°, 225°). In the last row, a merge image is displayed (Hcn4 in red, Rgs6 in green) with 2 major transitional sinoatrial conduction pathways (SACPs) outlined in purple and black lines, respectively ($Hcn4^{-}/Rgs6^{+}$). Purple SACP: from SAN body directed rightward; black SACP: from the SAN head directed inferiorly and leftward. Blue SACP: ($Hcn4^{+}/Rgs6^{+}$) emerges inferiorly from the tail of the SAN eventually giving rise to the internodal tracts. From[3].

Interestingly, three distinct clusters of cells were found to leave the cSAN in stereotyped directions, consistent through 15 biological replicates at different developmental stages (E16.5, postnatal day 1 (P1), P13). One such pathway is arising from the SAN head region extending inferiorly and leftward. The second group of transitional cells is consistently found to be arising from the SAN body extending rightward. And lastly, the third group of cells emerges from the SAN tail apically, ultimately giving rise to one major internodal tract of conduction cells. Thus, the novel SAN Tz specific marker Rgs6 in combination with three-dimensional imaging of intact SAN using iDISCO+ allowed for the precise anatomical elucidation of SAN Tz in murine hearts for the first time.

1.4.5. 3D architecture of the entire cardiac conduction system in intact murine hearts

Based on our scRNA-seq findings, *Cpne5* mRNA was enriched throughout the CCS including the SAN, SAN Tz, INT, AVN, NAVR, His bundle, as well as the ventricular conduction system including BB and PF cells. Driven by these findings, three-dimensional visualization of the entire CCS was performed to confirm the specificity of its protein expression throughout the intact heart. In this regard, postnatal day 13 (P13) mouse hearts were freshly harvested and underwent a designed iDISCO+ workflow (**Figure 1.15**) immunolabeling whole hearts with anti-Cpne5 antibodies (**Figure 1.17**). Consistent with our scRNA-seq data, *Cpne5* expression was found in all components of the CCS including transitional cells. To the best of my knowledge, this study presents the first three-dimensional model of the entire CCS including minor cell types such as Tz without the use of a transgenic animal model system. Of note, a high-resolution movie of this 3D CCS model is available online as presented in the supplemental materials of our published work[3].

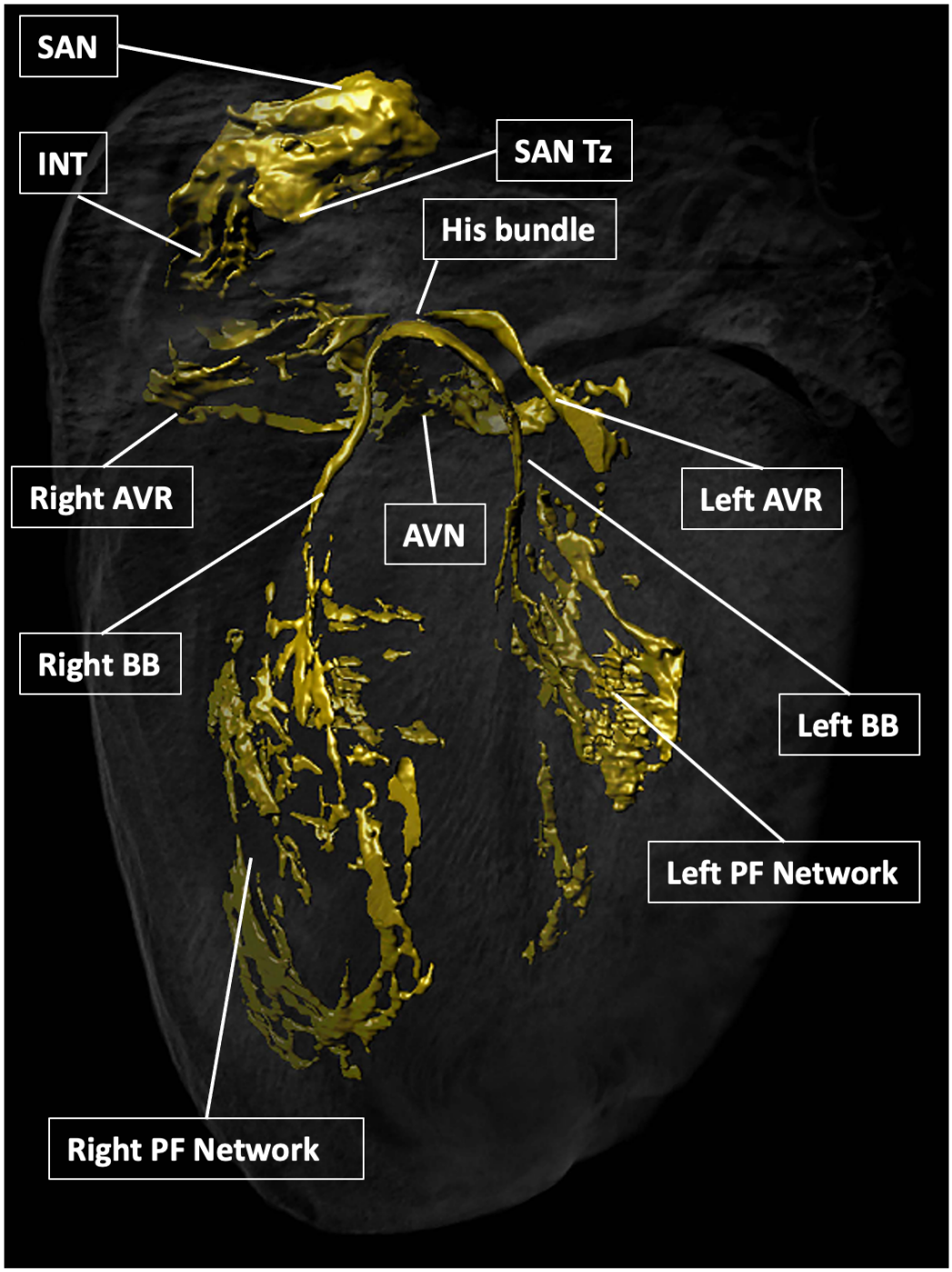

Figure 1.17: Immunolabeling and optical clearing reveal the three-dimensional architecture of the murine cardiac conduction system in whole organs

Intact wild-type hearts (n=5) at the age of postnatal day 13 (P13) were immunolabeled with anti-Cpne5 antibodies in a designed Immunolabeling-enabled three-dimensional imaging of solvent-cleared organs (iDISCO+) workflow. Upon organ clearing, more than 750 single images were captured through the entire hearts at 3 µm thickness using lightsheet microscopy. Three-dimensional objects of whole immunolabeled hearts were reconstructed using the interactive microscopy analysis software Imaris. Additionally, a virtual surface tool (gold) was used to increase signal intensity of Cpne5-labeled cells. AVN indicates atrioventricular node; AVR: atrioventricular ring; BB: bundle branch; INT: internodal tract; PF: Purkinje fiber; SAN: sinoatrial node; Tz: Transitional cells. Modified from[3].

1.4.6. Single-cell RNA-sequencing excels data purity of previous RNA-sequencing studies

The method of scRNA-seq was first published in 2009[51] and has since been widely used unraveling unique transcriptomes of various organ systems. However, to the best of my knowledge, our group was the first to use this technique on conduction cells within the heart. Thus, until now, bulk RNA-seq has been the primary method used to perform transcriptomic analyses of CCS cell types and to elucidate novel genetic markers.

Bulk RNA-seq can present differentially expressed genes within a given sample compared to control tissue. When obtaining highly pure cells from the structure of interest, it is possible to unravel tissue-specific gene expression profiles. However, within the SAN and other CCS components, pacemaker cells are intermingled with fibroblasts, neuronal cells, endothelial cells, white blood cells, and others[24,60]. Therefore, bulk RNA-seq data is often subject to "gene contamination", meaning that genes expressed in non-conduction cell types get falsely accredited to the CCS. Using scRNA-seq, it is now possible to precisely analyze gene expression in the conduction system at single cell resolution and this study has thus obtained the highest data purity possible. Here, the current scRNA-seq approach is compared to two of the most sophisticated bulk RNA-seq studies performed previously, that have made exceptional efforts on pacemaker cell purity[22,23].

Firstly, the Srivastava group has provided important novel SAN markers[23]. In their study, the group used cryosections from flash-frozen *Hcn4*-Gfp (green fluorescent protein) transgenic mouse hearts harvested at embryonic day 14.5 (E14.5). Further, RNA-seq data was generated from the SAN head region near the SAN artery (vs. right atrial myocardium) isolated by laser capture microdissection (LCM). Using the current study's scRNA-seq dataset, their 30 most significant differentially expressed SAN genes were re-analyzed. Interestingly, 22 genes were found to be truly enriched within the SAN. However, as many as 25% of detected transcripts (7 genes) derive from other cell types, such as epicardial cells, endothelial cells and fibroblasts (**Figure 1.18**). Thus, although *Hcn4*-based LCM is an innovative approach appropriate for the purification of SAN cells, a significant amount of gene contamination remained. One explanation for this phenomenon may be the relatively large fraction of *Hcn4*-negative non-pacemaker cells, which remain intermingled within the SAN and are thus additionally sequenced.

A.

Modified from *Vedantham et al. 2015*			Current Study	
Gene	Log(2) Fold-Change RA vs SAN	PValue	Cluster Enrichment for Zone I	Associated Cluster Identity
Isl1	-14.28835332	2.81E-75	C9	SAN
Smoc2	-7.383172348	1.62E-69		
Rgs4	-8.598664639	1.60E-57	C14	Neuronal
Hcn4	-5.873773035	1.94E-43	C9	SAN
Tbx3	-7.143232512	1.47E-39	C9	SAN
Shox2	-6.282438792	4.58E-37	C9	SAN
Gm15415	-5.106812377	4.52E-37	Not detected	Not detected
Odz4	-4.143877804	1.70E-33		
Csmd1	-6.364072299	1.51E-30		
Vsnl1	-4.37227765	3.80E-28		
Dmrt2	-8.068581086	8.53E-28		
Thbd	-4.645158256	1.09E-27	C4, C13	Endothelial
Gabra3	-4.819268604	3.17E-27		
Syn2	-5.673823248	4.43E-27		
Gm2301	-11.58561666	4.33E-26		
Kif1a	-4.21900186	7.00E-25		
Cckar	-8.063142611	2.06E-24		
Ssr4	-6.273610875	6.97E-22	All Clusters	N/A
Rgs6	-3.20300397	1.00E-21		
Hcn1	-5.343241944	1.13E-21	C9	SAN
Bmp2	-4.415253764	7.50E-21		
Mfsd6	-2.998749942	8.15E-21		
Gucy2e	-10.86679374	2.45E-20		
Uchl1	-4.439850542	3.19E-20		
S1pr3	-3.188558335	4.40E-20	C2, C5, C6	Fibroblast
Itgb8	-3.177652546	1.34E-19	C10	Epicardial
Cntfr	-4.646736865	1.88E-19	C2, C6, C12, C14	Fibroblast/Mixed
Cthrc1	-8.61221459	6.65E-19	C2, C5, C6 C11	Fibroblast
Fzd7	-2.84996998	4.15E-18		
Ramp1	-3.794472111	5.76E-17		

B.

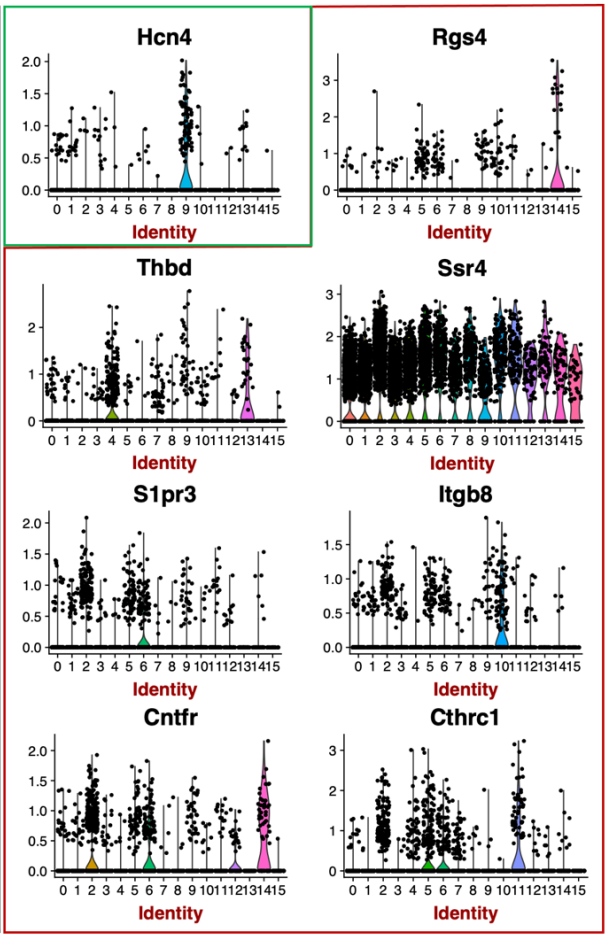

Figure 1.18: Laser capture microscopy-purification and bulk RNA-sequencing results in significant data contamination from non-conduction cell types

A. Table modified from Vedantham et al. 2015[61], listing the 30 most significant differentially expressed sinoatrial node (SAN) genes. The right side of the table displays for each gene the corresponding cell cluster from the current study's single-cell RNA-sequencing (scRNA-seq) data within zone I of embryonic day 16.5 mice. Genes highlighted in green represent known SAN genes. Genes highlighted in red represent examples of enrichment due to contaminant cells as listed. *Gm15415* encodes a predicted long non-coding RNA that was not detected within our scRNA-seq dataset under its current name. **B.** Gene expression enrichment across all 15 clusters within zone I, visualized by violin plots. Cluster 9 (C9) represents the SAN cell cluster, while other atrial cardiomyocyte clusters include C0, C1, C3, C12, C15. Additional clusters, based on their respective gene expression profiles, include fibroblasts (Clusters 2, 5, 6, 11), endothelial cells (Clusters 4, 7, 13), epicardial cells (Cluster 10), white blood cells (Cluster 8) and neuronal cells (Cluster 14). From[3].

Secondly, the Christoffels group took a recent approach in order to further purify SAN cells and eliminate intermingled non-conduction cell types for RNA-sequencing[22]. This group used a *Tbx3*-Venus reporter knock-in mouse model in combination with Fluorescence-activated cell sorting (FACS) purification of SAN pacemaker cells. Tbx3 is known to play an essential role in SAN development[7] and it is thus thought to be almost exclusively expressed within the CCS. Thus, Tbx3-positive cells were FACS isolated in order to obtain highly pure SAN cells from E17.5 mice. Of note, the author himself recognized large variation and heterogeneity between SAN samples, namely small SAN size, low cell numbers and putatively incomplete cell dissociation before FACS purification. When using our scRNA-seq dataset to analyze the top 16 differentially expressed SAN genes, massive gene contamination issues were recognized. Of their top 16 genes, 25% (*Hcn4, Tbx3, Shox2, Nfasc)* are established CCS-markers and were found highly enriched within SAN cluster 9 of this current scRNA-seq study. However, 75% of

the top 16 genes show higher enrichment within non-conduction cell types such as fibroblasts (clusters 2,5,6,11), endothelial cells, (cluster 13), endocardial cells (cluster 4 and 7) and neuronal cells (cluster 14) (**Figure 1.19**). While Tbx3 is important for SAN development and is indeed highly enriched within SAN cells, it is a key transcription factor for the development of limbs, certain neurons, mammary glands, the liver and other structures[62–65]. Thus, *Tbx3* gene expression is not exclusive to the SAN and may not be an ideal marker for SAN cell purification.

A.

Modified from *Van Eif et al. 2019*			Current Study	
Gene	Log(2) Fold-Change RA (Katushka+) vs SAN (Venus+)	p-value	Cluster Enrichment for Zone I	Associated Cluster Identities
Ngfr	-6.604350686	2.70E-41	C14	Neuronal
Ntrk3	-6.500756702	1.95E-24	C11	Fibroblast
Figf	-6.453818752	1.03E-12	C2, C6	Fibroblast
Tnxb	-6.44060532	9.43E-18	C2, C5, C6, C10, C11, C12	Fibroblast/Epicardial/CM
Tgfb1	-6.297994994	6.46E-14	C4, C7, C8, C13	Endocardial/WBC/Endothelial
Nfasc	-6.233087993	3.18E-35	C9	SAN
Sox18	-6.228369461	3.41E-12	C4, C7	Endocardial
Ltbp4	-6.102507339	3.04E-21	C2, C4, C5, C6, C7, C10, C11, C12	Fibroblast/Endocardial/Epicardial/CM
Hcn4	-6.044298097	9.64E-19	C9	SAN
Adam12	-5.95992986	1.14E-20	C2, C5, C6	Fibroblast
Shox2	-5.958662083	6.81E-26	C6, C9, C12	SAN/Fibroblast/CM
Col15a1	-5.94994844	5.73E-31	C4, C7, C14	Endocardial/Neuronal
Aatk	-5.897518412	7.85E-18	C14	Neuronal
Fndc1	-5.809981383	5.12E-16	C2, C5, C6, C10, C11, C12	Fibroblast/Epicardial/CM
Ptprz1	-5.789636644	3.88E-17	C14	Neuronal
Tbx3	-5.77333563	3.30E-29	C9, C14	SAN/Neuronal

B.

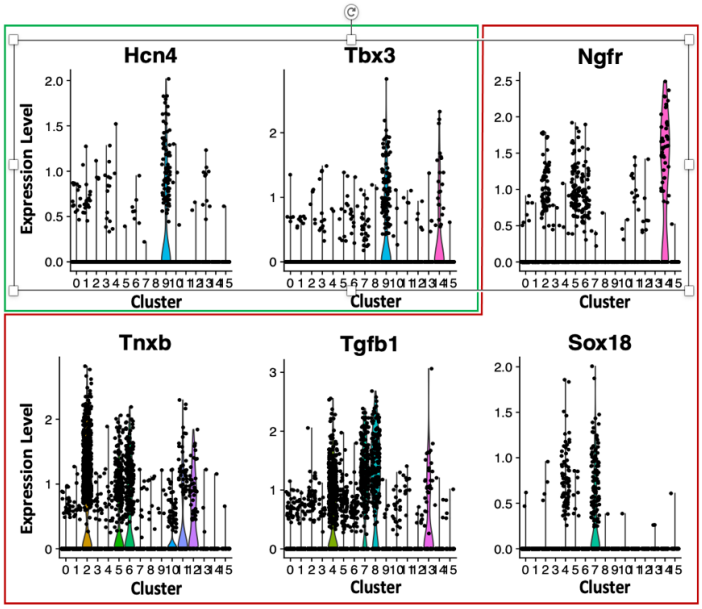

Figure 1.19: Tbx3-sorted RNA-sequencing results in significant data contamination from non-conduction cell types

A. Table modified from *Van Eif et al. 2019*[22] listing the top 16 differentially expressed sinoatrial node (SAN) genes in sorted *Tbx3*-Venus$^+$ cells versus Katushka$^+$ cells from embryonic day 17.5 (E17.5) mice. The right side of the table displays for each gene the corresponding cell cluster from the current study's single-cell RNA-sequencing data within zone I of E16.5 mice. Genes highlighted in green represent known SAN genes. Genes highlighted in red represent genes enriched within contaminant cell types. **B.** Gene expression enrichment across all 15 cell clusters within zone I, displayed in violin plot format. Cluster 9 (C9) represents the SAN cell cluster, while other atrial cardiomyocyte clusters include C0, C1, C3, C12, C15. Additional clusters include fibroblasts (Clusters 2, 5, 6, 11), endocardial/endothelial (Clusters 4, 7, 13), epicardial (Cluster 10), white blood cells (WBC, Cluster 8) and neuronal cells (Cluster 14). CM indicates cardiomyocyte. From[3]

Both of these studies have been chosen for their exceptional efforts in SAN cell purification. As a result, multiple novel CCS-enriched genes have emerged from these studies. The comparison of bulk RNA-seq studies to our approach clearly demonstrates, however, that

scRNA-seq is ideal to elucidate comprehensive transcriptomic fingerprints even of minor CCS cell types including transitional cells, which cannot be individually studied using bulk RNA-seq. Thus, the current study unraveled novel genes expressed within certain CCS components. In the following, their putative function will be discussed.

1.5. Discussion

To the best of my knowledge, Part I of this study presents single cell transcriptomic profiles of the entire CCS for the first time. Using scRNA-seq, a comprehensive gene atlas representing all major components of the developing murine CCS was established. Additionally, scRNA-seq data has been validated using immunohistochemistry, high-resolution fluorescence *in situ* hybridization as well as immunolabeling in whole organs using iDISCO+. Overall, five novel genetic markers of the CCS (*Rgs6, Cpne5, Igfbp5, Ntm* and *Smoc2*) were uncovered. Importantly, these novel markers not only label major CCS components (e.g. cSAN, cAVN, His, PF) but also help to identify, for the first time, previously elusive transitional cells. Parts of the data presented in chapter I have already been published in the journal *Circulation Research*[3].

1.5.1. Importance and function of novel genetic markers found in this study

This study has led to the discovery of a host of CCS-enriched genes, 5 of which were validated using IHC, iDISCO+ and FISH. Namely, *Rgs6*, *Cpne5*, *Ntm*, *Smoc2* and *Igfbp5* showed remarkable fold changes in gene expression within CCS components and have never been associated with the conduction system before. While their true role in CCS development, function and disease remains to be elucidated, their high exclusivity to conduction system components is suggestive of a putative role in CCS development and/or function.

Regulator of G-protein signaling 6 (*Rgs6*) was found to be expressed in the cSAN and SAN transitional cells, as well as in the cAVN. However, *Rgs6* was found to be absent in the ventricular conduction system. Interestingly, *Rgs6* was previously described to be a negative modulator of parasympathetic influence[66,67], which may directly correlate with high *Rgs6* enrichment within the SAN and AVN shown in our study. *Rgs6* has further been implicated in decreased resting heart rate and increased heart rate variability in both mice (by homozygous *Rgs6* knockout models) and in humans by GWAS[68–70]. Additionally, studies have shown a heart-protective role of *Rgs6* in events of ischemic injury[71]. In summary, *Rgs6* has been implicated in various cardiac functions before. However, precise transcriptional expression patterns of this gene have not been assessed and *Rgs6* enrichment within CCS-components was unknown. Taken together, the discovery of the exact expression pattern of *Rgs6* within the heart may present an important target in the diagnosis and treatment of cardiac rhythm disorders and heart disease.

Copine 5 (*Cpne5*) is a novel gene found to be enriched in the entire CCS, including the cSAN, SAN Tz, INT, cAVN, nodal AV rings, His, as well as the ventricular conduction system including BB and PF cells. While a deeper understanding of Copine function is lacking, Cpne5 was previously described to perform intracellular functions such as membrane trafficking in a calcium-dependent manner[72]. Interestingly, *Cpne5* and its paralog *Cpne8*, are gene candidates implicated in human heart rate variability shown by GWAS[68,73]. In summary, *Cpne5* gene expression shows remarkable enrichment as well as high exclusivity to key components of the CCS and is further functionally linked to a role in heart rate variability in humans by GWAS.

Thus, further gain- and loss-of-function models have the potential to reveal the necessity and sufficiency of *Cpne5* in CCS function.

Neurotrimin (*Ntm*) is a novel gene found to be enriched within the cSAN, SAN Tz, cAVN, His bundle as well as in PF and PF Tz. Although *Ntm* is an established cell adhesion molecule in the central nervous system[74], it has not been associated with the heart before and its functional role in the conduction system remains to be elucidated. Moreover, given its extracellular localization, *Ntm* may be the first viable marker for live CCS-cell sorting in wild-type hearts. While Contactin-2 (*Cntn2*) is a well-known GPI-anchored, fully extracellular cell surface marker expressed within all major components of the CCS[75], robust gene expression can only be detected postnatally[3,22]. In this regard, researchers are currently left incapable of live CCS cell sorting, since most FACS devices are incapable of sorting adult cardiomyocytes due to cell-size limitations. The discovery of *Ntm* as a novel and fully extracellular marker enriched within all major components of the CCS both embryonically and in the adult heart provides an ideal marker for CCS cell sorting of core conduction cells as well as previously elusive transitional cells. *Ntm*-based cell sorting, therefore, has the potential for deeper insight into the function and development of all major CCS components at various developmental stages.

SPARC-related modular calcium-binding protein 2 (*Smoc2*) transcript enrichment was discovered in the SAN and SAN Tz, while expression of this novel gene was found fully repressed in the AVN and the ventricular conduction system. *Smoc2* is a member of the BM-40/osteonectin family of calcium-binding secreted matricellular proteins and was previously hypothesized to function as an inhibitor of extracellular matrix (ECM) mineralization and calcification[76,77,78]. Thus, given its high and specific gene expression within the SAN and SAN Tz, a possible role for *Smoc2* in cellular electrical coupling between the SAN and the surrounding atrial cardiomyocytes may be suggested. Additionally, a putative function of *Smoc2* in the prevention of CCS-calcification should be further studied in the future. However, van Eif et al. have very recently assessed the functional role of *Smoc2* in CCS function using a CRISPR/Cas9-based systemic homozygous murine knockout model[22]. Interestingly, despite its high gene expression within the SAN, no functional CCS abnormality was found in *Smoc2*$^{-/-}$ mice suggesting only minimal impact of *Smoc2* inactivation on cardiac function or compensatory phenotypic rescue from upregulation of a paralogue such as *Smoc1*. Nevertheless, given expression enrichment within the SAN and SAN Tz, *Smoc2* is a valuable genetic marker for future CCS research into the identification and isolation of SAN conduction cells.

Insulin like growth factor binding protein 5 (*Igfpb5*) gene expression was found to be highly enriched throughout the entirety of the CCS. Previously, Insulin-like growth factors (IGFs) were described to be important proteins involved in the development of various types of tissues[79,80]. In this regard, six individual IGF-binding proteins (IGFBP-1 to IGFBP-6) exist, which contain unique motifs and may thus function in very different ways. The genetic marker *Igfbp5* presented in this study was previously hypothesized to play a role in the inhibition of cell malignant behaviors such as proliferation, migration and invasion[81]. Moreover, *Igfbp5* may directly promote cell adhesion through interaction with certain integrins[82]. Taking these previous studies into account and given its high enrichment within pacemaker components shown in the current study, *Igfbp5* may be critically involved in the maintenance of SAN and AVN architecture[83]. Thus, while our understanding of insulin signaling within the heart

remains poor, the nodal *Igfbp5* gene expression discovered in the current study should encourage more research on this topic.

In summary, the elucidation of the novel genes *Rgs6, Cpne5, Ntm, Smoc2* and *Igfbp5* provide genetic markers allowing for the precise identification, visualization, and isolation of CCS cell types for further functional analyses of conduction cells. Additionally, the discovery of these novel genes may promote future research on their putative role in the pathogenesis of cardiac rhythm disorders and has the potential to propel novel treatment methods for cardiac arrhythmias associated with the CCS.

1.5.2. Functional role of sinoatrial node transitional cells in rhythmic cardiac beating

Ever since transitional cells have first been noted at the periphery of the cSAN[27], a crucial role of these cells in the initiation of cardiac rhythm has been suggested. However, their true function and their precise anatomical localization have remained elusive. Here, I hypothesize a putative role of SAN Tz in building specialized cellular pathways effectively bridging the compact SAN with the surrounding atrial myocardium.

It has previously been hypothesized, that depolarization does not leave the SAN in all directions simultaneously but rather through specialized conduction pathways[5]. These interdigitating nodal and atrial bundles along the SAN periphery have first been suggested several decades ago[26,27]. More recently, optical mapping studies pointed at distinct localizations of these pathways[5,84] and named them SAN exit pathways (SEP)[30] or SAN conduction pathways (SACP)[5]. Further, in a review published in 2012, Fedorov et al. have combined results of various functional, structural and molecular SAN studies[85] to generate a comprehensive functional SACP model (**Figure 1.20**). These studies demonstrate precise three-dimensional locations of SACPs through which electricity leaves the compact SAN, however the identity of these cells had remained largely unknown.

This current study not only provides some of the first novel markers of these transitional cells but also used advanced imaging techniques (iDISCO+ with light sheet imaging) to firmly establish the three dimensional anatomical location of Tz in the context of the intact SAN. At least three distinct populations of transitional cells were identified at very discrete and reproducible locations (**Figure 1.16**). Strikingly, the anatomical location of transitional cells shown in the current study perfectly match the location of SACPs suggested previously using optical mapping[84,86]: one SACP emerges from the SAN body directed rightward; the second SACP emerges from the SAN head directed inferiorly and leftward; and the third SACP emerges from the SAN tail directed inferiorly eventually giving rise to a major internodal tract (compare **Figure 1.16** to **Figure 1.20**). This work provides additional support to the hypothesis that SAN Tz play a crucial role in guiding depolarization from pacemaker cells within the cSAN through specialized pathways to the rest of the heart. Thus, SAN Tz may play a crucial role in the initiation of cardiac rhythm and disruption of these cells could lead to severe diseases such as SAN exit block.

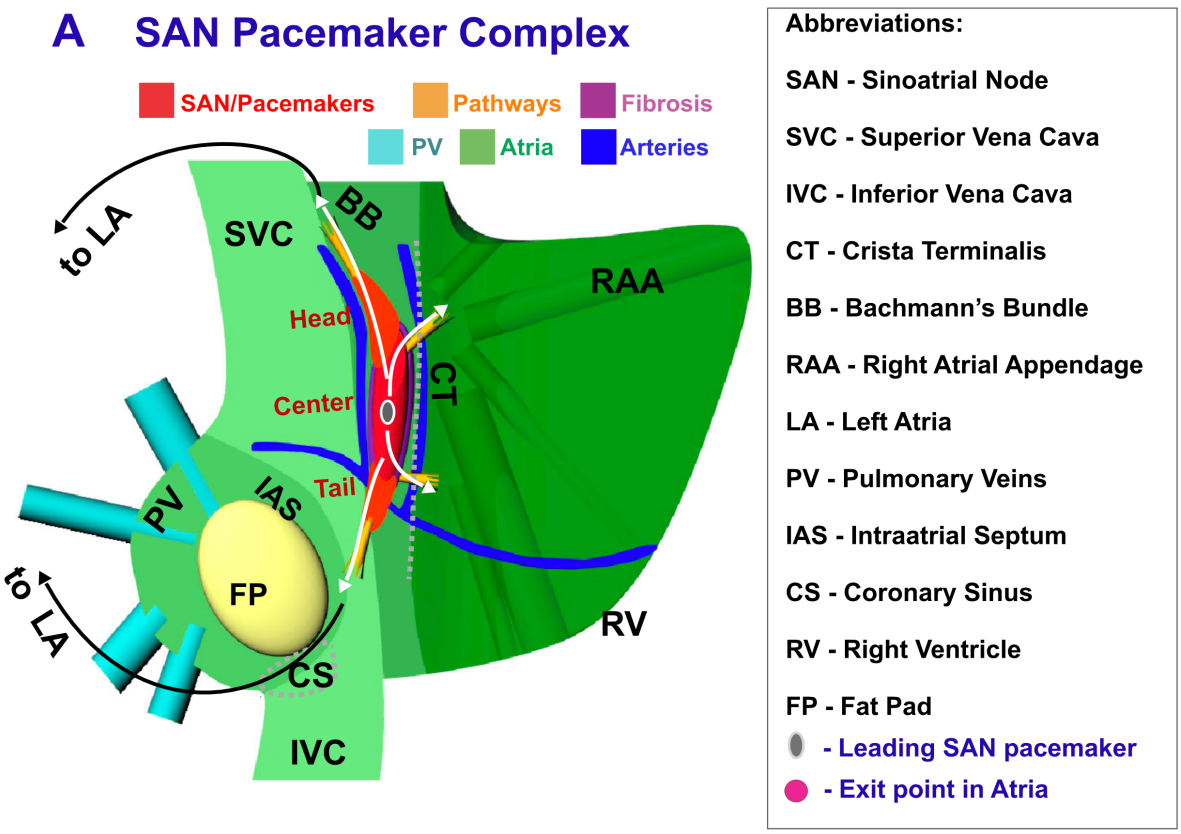

Figure 1.20: Model of sinoatrial node pacemaker complex
Enlarged epicardial view of 3-dimensional canine sinoatrial node (SAN) model based on structural and functional data from optical mapping experiments. The SAN (red) is isolated from the surrounding atrium (green) by 3 bifurcating coronary arteries (blue) and fibrosis (purple). The yellow bundles show sinoatrial conduction pathways (SACPs) that electrically connect the SAN to the atrium. From[85]

1.5.3. 3D architecture of the entire cardiac conduction system

It was consensus among most researchers in the early 1900s that electrical impulses travel from the SAN to the AVN through plain atrial myocardium. However, the existence of internodal and interatrial conduction pathways guiding depolarization from the main pacemaker in the SAN to the AVN have been discussed for over a century. Thorel, Wenckebach and Bachmann were a few of the first to make this claim and received more support over time[87]. However, the identity and existence of internodal tracts are still debated.

Various attempts have been made to unravel the complex 3D anatomy of the CCS[13,88]. However, to my knowledge, CCS components have never been shown three-dimensionally in whole hearts before. In this study, a handful of novel genetic markers were discovered, one of which (*Cpne5*) was found to be highly enriched within all components of the CCS including transitional cells, as shown in a 3D model of the entire CCS within intact hearts. Strikingly, besides precisely representing all CCS components in whole hearts, at least one major internodal tract was consistently detected in a precise anatomical location (**Figure 1.17**). While internodal conduction pathways demonstrated in our model need further functional evaluation, results from our work prove the existence and the precise location of a specialized internodal tract in mice.

1.5.4. Development of biological pacemakers

Since 1958, when the first attempt of permanent pacemaker implantation (PPI) was performed at the Karolinska Institute in Sweden[89], PPIs have rapidly improved and created a tremendous market. Permanent pacemakers are implanted over 200,000 times a year in the US alone and more than 600,000 times globally[90,91]. Although PPIs represent life-saving systems in cases of CCS failure, PPI-related complications include thrombogenesis, infections of the lead, low battery lifetime, inability to adjust to growing hearts in pediatric populations, inability to adjust to physical activation and autonomic signals as well as cardiac remodeling and scar formation at insertion sites[92,93]. Moreover, pacemakers set the need for monitoring, maintenance, and pacemaker replacement which further leads to a large financial burden for health care systems all around the globe.

For these reasons, the innovative idea of biological pacemaker cells that could be implanted into humans with CCS loss-of-function starts to come more into focus. To generate SAN-like cells in a dish, induced pluripotent stem cells (iPSC) or human embryonic stem cells (hES) can be differentiated into beating heart tissues *in vitro*[94–97], even displaying pacemaker-like properties[98]. Further, previous studies have proven successful cardiac pacing post stem cell-derived heart tissue transplantation in large-animal models of complete AV-block[99]. However, major challenges remain, including the prevention of tissue rejection, teratoma formation, arrhythmogenesis as well as successful long-term integration of the graft into the patient's heart. Moreover, most *in vitro* cardiomyocytes only achieve low rates of <60 beats per minute, which may be due to their ventricular-like (rather than pacemaker-like) transcriptomic signature. Other groups currently pursue different approaches, namely a) somatic gene transfer to resident cardiomyocytes[100] or b) cell fusion of resident cardiomyocytes with cells generated *in vitro* that are equipped with a set of ion channels necessary for pacemaker function[101].

Overall, all currently pursued approaches for the generation of viable biological pacemakers are missing an in-depth understanding of transcriptomic pacemaker properties. In this regard, the current study has discovered the endogenous transcriptome of all pacemaker cell types thereby providing a blueprint for future efforts in biological pacing (see online supplemental tables in [3]). The entire dataset generated in Part I of this study is uploaded to the GEOdatabase and made publicly available encouraging future research on the generation of biological pacemakers.

Part II: Generation of novel optical imaging tools for intraoperative visualization of the cardiac conduction system

1.6. Introduction

1.6.1. Intraoperative injury to cardiac conduction system components

The CCS is essential for the formation of our everyday heartbeat and direct injury to either of its specialized components can result in severe cardiac arrythmias or even sudden death[14,18–20]. Due to our current inability to visually distinguish conduction cells from the surrounding working myocardium, heart surgeons have to rely on rough anatomical landmarks and their surgical experience in order to spare important CCS structures when operating on the human heart[102]. Therefore, inadvertent incision or suture placement remains a significant cause of postoperative conduction system dysfunction[18,102–104]. As a result, surgical damage to the CCS oftentimes leads to life-long pacemaker dependency, which in turn increases morbidity and mortality and reduces long-term survival. Patients being at high risk for the above-mentioned events include both children and adults undergoing open heart surgery.

1.6.2. Risk of injury in congenital heart disease surgery

Congenital heart disease (CHD) remains the most common birth defect, affecting roughly 1 in 100 infants[105]. Oftentimes, patients with CHD undergo surgical treatment at least once during their lifetime. Furthermore, congenitally malformed hearts often demonstrate significant variation in their CCS location within the heart. Thus, predicting the anatomical location of CCS structures and pathways is particularly challenging in CHD surgery. In fact, 1-3% of all CHD operations and >15% of more complex repairs result in postoperative atrioventricular block (AVB)[106,107] from damage to the AVN. The AVN is also highly susceptible to surgical damage during the correction of congenital malformations such as levo-transposition of the great arteries (L-TGA) and AV canal defect[108]. In fact, in the latter two malformations, the entire AVN is located outside of the triangle of Koch[109–111], its physiological seat in the floor of the right atrium. Moreover, the ventricular conduction system is at highest risk during the surgical repair of ventricular septal defects[102], being one of the most common birth defect of all. Finally, interventions putting patients at highest risk for damage to the SAN include the Fontan, Glenn, Mustard and Senning operations, among others[108,112,113].

1.6.3. Risk of conduction system injury in adult cardiac surgery

Adult patients undergoing cardiac surgeries that intervene at sites of close proximity to conduction tissues (such as valve replacements and reconstructions) are particularly at high risk of iatrogenic CCS damage. In fact, there is a total of about 106,000 adult valve surgeries a year in the US alone, 8-26% of which are associated with postoperative AVB[114]. Specifically, aortic valve replacement imposes the highest risk in adults, as observed in 26% of patients undergoing this procedure[114]. Moreover, following mitral valve replacement and mitral valve annuloplasty, postoperative AVB was described in over 23% of patients[115]. Although associated with lower incidences, postoperative arrythmias have additionally been noted post tricuspid valve replacements as well as post repair of atrial and ventricular septal defects

(ASD/VSD)[116,117]. Therefore, the surgeon's inability to detect vital CCS structures lying near sites of frequent surgical intervention results in a significant risk for damage not only in pediatric but also adult patient populations.

1.6.4. General concept of antibody-based imaging

To date, no diagnostic method exists for the intraoperative, real-time visualization of CCS components. Addressing this critical unmet medical need, a novel optical imaging tool allowing heart surgeons to visualize and thus locate all CCS components in high-resolution and real-time is needed to reduce intraoperative damage and the associated morbidity and mortality of patients. In this regard, fluorescently labeled antibodies that specifically bind to CCS components represent an ideal tool to tackle this challenge. In fact, antibody-based optical imaging has already begun to revolutionize medical imaging within the field of oncology, where early studies have already validated its use in real-time detection of tumor tissue[118].

For the generation of antibody-based diagnostic tools, a cell surface marker (e.g. receptor, ion channel, GPI-anchored protein, transmembrane protein, etc.) needs to be selected, that is specifically enriched within the structure of interest (e.g. the CCS) but largely absent from the surrounding tissue (e.g. working myocardium). As antibodies show high binding-specificity to markers of interest, they can be used as a vehicle for precise delivery of fluorescent probes to CCS structures. Therefore, direct chemical conjugation of specific antibodies to near-infrared (NIR) (800nm) fluorophores (**Figure 2.1**) provide the basis for novel optical imaging tools for the real-time visualization of CCS structures.

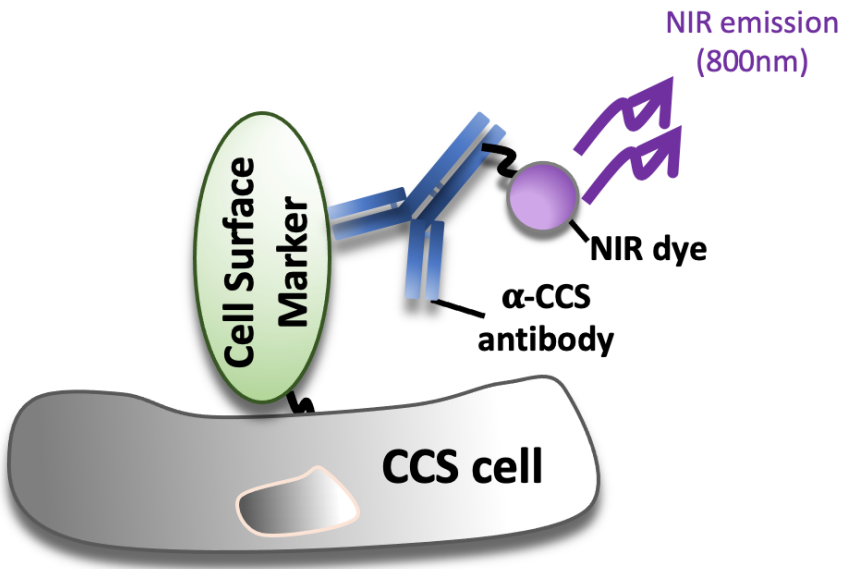

Figure 21: General concept and design of novel optical imaging agents
Cardiac conduction system (CCS) cell specific IgG-antibodies (blue) are covalently conjugated to near-infrared (NIR)-dyes (purple). Next, conjugated antibodies bind to CCS-specific cell surface markers (green) upon intravenous injection. Thus, NIR fluorescence imaging systems can be used to visualize CCS structures intraoperatively. Modified from[119]

These diagnostic agents are envisioned to be systemically administered to the patient prior to the planned surgical procedure, allowing for the real-time visualization of the CCS in the

operating room with the help of a camera system (e.g. SPY-Elite, Stryker) and thereby minimizing the risk for accidental CCS injury.

1.6.5. Established optical imaging tools improving the precision in tumor resection

Similar antibody-based optical imaging agents are currently being evaluated in human clinical trials for the improvement of precise detection of solid tumors. Currently, surgeons rely on nonspecific visual changes and gross manual palpation to guide successful tumor excision[120]. Given Epidermal growth factor receptor (EGFR) overexpression in over 90% of head and neck tumors, fluorescently labeled anti-EGFR antibodies have successfully been exploited for the visual detection of precise head and neck tumor margins at submillimeter resolution[120–122]. In fact, diagnostic tools designed by co-investigators of this current study (Rosenthal group), are currently undergoing clinical trials at Stanford University guiding cutaneous squamous cell cancer resection in humans[121,123](**Figure 2.2**).

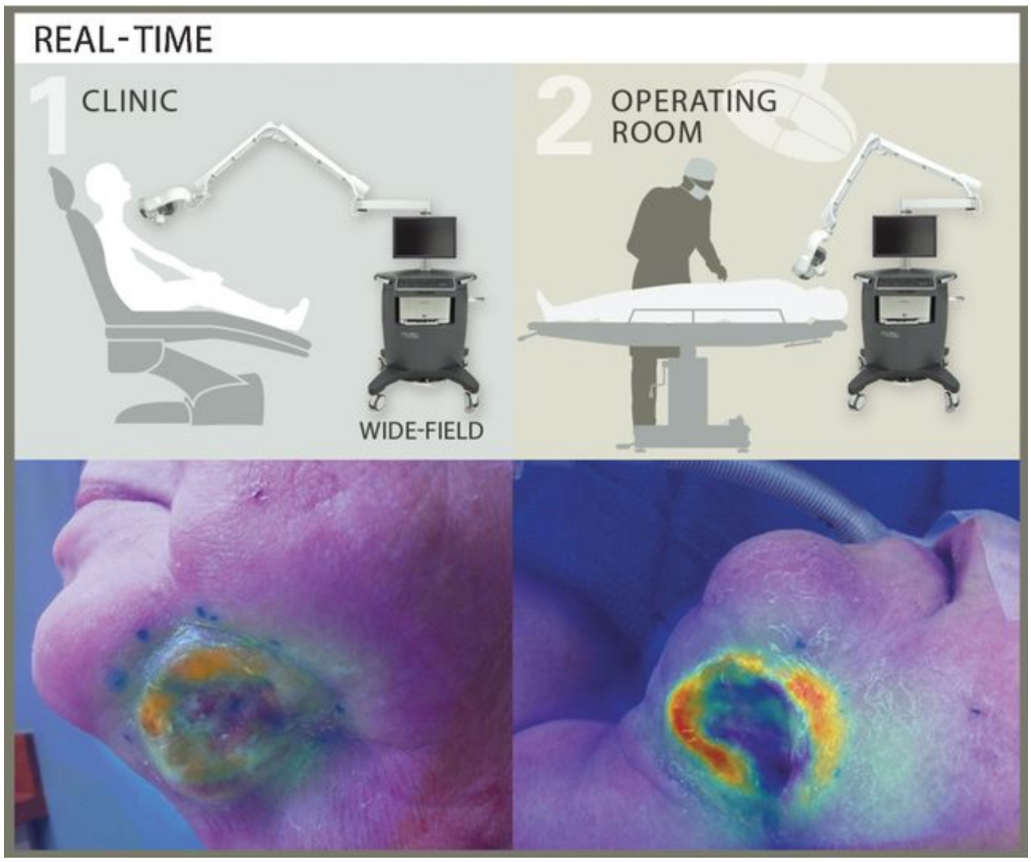

Figure 22: Trial imaging workflow for head and neck cancer detection
Real-time imaging was performed with a wide-field near-infrared (NIR) imaging system in the clinic on (1) days 0, 1, and in the (2) operating room on day 3 after cetuximab-IRDye800 infusion. From[120]

In addition to head and neck cancer surgeries, optical imaging agents have also successfully been established for the detection of other cancers including ovarian, breast, pancreatic and colorectal cancers as well as gliomas[124–128] thus reinforcing the translatability of novel optical imaging tools.

To the best of my knowledge however, successful *in vivo* delivery of fluorescent probes to substructures within the heart has never been performed before.

1.6.6. Aims of this study

In order to tackle the unmet medical need described above, this study aims to uncover novel and specific CCS-enriched cell surface markers. Novel cell-surface markers will then be used as molecular targets for *in vivo* antibody-based labeling of the CCS. Further, this study additionally aims to generate novel diagnostic tools, which consist of near-infrared (800 nm) dyes, covalently conjugated to CCS-specific IgG-antibodies. Moreover, preclinical validation of these novel diagnostic tools will be performed to assess *in vivo* antibody-binding characteristics as well as the sensitivity and specificity of novel tools promoting clinical translation.

1.7. Material

Material for IHC and iDISCO+ analysis was used as listed above in the methods section of Part I.

1.7.1. Primary antibodies	
Rabbit anti-mouse anti-Cx40 polyclonal antibody	#Cx40-A, Alpha Diagnostics, USA
Goat anti-mouse anti-Cntn2 polyclonal antibody	#AF4439, R&D Systems, USA
Rat anti-mouse anti-Hcn4 monoclonal antibody	#ab32675, Abcam, USA
Goat anti-mouse anti-Np65 polyclonal antibody	#AF5360, R&D Systems, USA
Sheep anti-mouse anti-Nptn55 polyclonal antibody	#AF7818, R&D Systems, USA

1.7.2. Secondary antibodies	
Chicken anti-rat IgG Alexa Fluor 594	#A31572, Invitrogen, USA
Chicken anti-rat IgG Alexa Fluor 647	#A-21472, Invitrogen, USA
Donkey anti-goat IgG Alexa Fluor 488	#ab150133, Abcam, USA
Donkey anti-goat IgG Alexa Fluor 555	#A-21432, Invitrogen, USA
Donkey anti-goat IgG Alexa Fluor 647	#A21447, Invitrogen, USA
Donkey anti-rabbit IgG Alexa Fluor 555	#A31572, Invitrogen, USA
Donkey anti-rabbit IgG Alexa Fluor 647	#A-31573, Invitrogen, USA
Donkey anti-sheep IgG Alexa Fluor 555	#A21436, Invitrogen, USA
Donkey anti-sheep IgG Alexa Fluor 647	#A21448, Invitrogen, USA

1.7.3. Devices	
Axio Imager 2 Microscope	Zeiss, USA
Light Sheet Microscope	Ultramicroscope II, LaVision Biotec, USA
SPY Elite Imaging System	Stryker, USA
Pearl® Trilogy Small Animal Imaging System	LI-COR, USA

1.7.4. Antibody conjugation kits and systemic injection supplies	
800CW NHS Ester Dye (0.5mg)	#929-70020, LI-COR, USA
800CW NHS Ester Microscale Labeling Kit: • IRDye 800CW Reactive Dye vials (0.1 mg) • 0.5 mL 1 M Potassium Phosphate (K2HPO4), pH 9 • 25 mL 1X PBS (store at 4 °C) • 0.5 mL ultra-pure water • Pierce® Zeba™ Desalting Spin Columns, P/N 89891	#928-38044, LI-COR, USA
Dulbecco's PBS (DPBS)	#14190144, Thermo Fisher, USA
Zeba™ Spin Columns (0.5mL)	#89882, Thermo Fisher, USA

1.8. Methods

1.8.1. Mice

For general comments, see methods section of Part I. Specifically, for systemic injection of novel optical imaging tools, wild-type CD1 male and female mice were used at ages of 4-6 weeks. For IHC analyses, mice were used at indicated ages.

1.8.2. Immunohistochemistry

Immunofluorescence analyses were performed as described above in the methods section of Part I.

1.8.3. Immunolabeling-enabled three-dimensional imaging of solvent-cleared organs

IDISCO+ was performed per iDISCO+ protocol (https://idisco.info/idisco-protocol/) and as described above in the methods section of Part I, with the following variation: In this part of the study, polyclonal anti-Cntn2 antibodies (#AF4439, R&D Systems) were covalently conjugated to NIR-fluorophores (described below) and systemically administered to wild-type, CD1 mice at the age of 4-6 weeks through tail-vein injections. 48 h post systemic infusion, mice were sacrificed, hearts were isolated by dissection and covered from light in all following steps. First, hearts were washed in HBSS (Ca^+/Mg^+) (Gibco, #14025-134) and fixed overnight in 4% paraformaldehyde in 1x PBS (Fisher, #50-980-487) at 4°C. Next, hearts were rinsed in 1x PBS for 15 min 3 times in order to wash off excess PFA and avoid overfixation. For the iDISCO+ workflow, hearts were then dehydrated in serial dilutions of methanol (#A452-4, Fisher Scientific) in 1x PBS (20%, 40%, 60%, 80%, 100%, 1 h each). Samples were again washed in 100% methanol for 1 h, and then chilled at 4°C for at least 3 h. Overnight, hearts were incubated in 66% dicloromethane (DCM) (#270997, Sigma-Aldrich) in 33% methanol at room temperature (RT) with shaking. The next day, samples were washed twice in 100% methanol at RT, and then cooled down 4°C until hearts were bleached in pre-cooled 5% H_2O_2in methanol (1 volume 30% H_2O_2 to 5 volumes methanol), overnight at 4°C. The following steps (rehydration, permeabilization, blocking, incubation in primary/secondary antibodies) were not performed in this part of the study, since fluorescently labeled antibodies had already bound to the structure of interest after *in vivo* injections. Lastly, hearts were incubated for 3 h (with shaking) in 66% DCM / 33% methanol at RT, and then in 100% DCM for 15 min twice

(with shaking) before final incubation in DiBenzylEther (DBE) (no shaking). The tube was filled almost completely with DBE to prevent sample oxidation. One day after clearing, iDISCO+ samples were imaged using light sheet microscopy. Entire hearts were scanned at a step-size of 3 µm. Thus, up to 800 images were acquired scanning entire organs. A minimum of 8 biological (different hearts) replicates were used for each immunolabeling approach. In order to reconstruct three-dimensional images from multiple images taken with the light sheet microscope, the interactive 3D image visualization and analysis software Imaris was used. No additional modification tools were used to create 3D images, except otherwise explained. Modified from[3].

1.8.4. Human cardiac conduction tissues

Human cardiac conduction system tissue samples (Adult, n=1, 45 years; Infant, n=1, 11 months) with post-mortem intervals (PMI) shorter than 24 h were acquired from the tissue bank of the pathology department at Stanford University and were appropriately de-identified.

1.8.5. Generation of optical imaging agents

To generate novel antibody-based optical imaging agents (Nptn-800 and Cntn2-800), polyclonal antibodies (1. anti-Cntn2 goat polyclonal antibodies (#AF4439, R&D Systems); and 2. anti-Nptn goat polyclonal antibodies (#AF7818, R&D Systems)), were chemically conjugated to a commercially available near-infrared (NIR) dye (IRDye800CW, #928-38044, LI-COR). IRDye800CW was used due to its characteristics of low non-specific binding, high signal-to-noise ratio and deep tissue penetration. In fact, IRDye800CW was previously demonstrated to be benign to rodents[129] and humans[123]. First, anti-CCS antibodies were prepared at a concentration of 1 mg per mL (100 µg diluted in 100 µL of 1x PBS). Critically, the pH of prepared antibody solutions must then be raised to a pH of 8.5, in order to raise the efficiency of the labeling reaction. To do so, 1/10th volume (10 µL) of 1.0 M potassium phosphate buffer (K_2HPO_4; pH 9), provided in the kit (#928-38044, LI-COR), was added to each vial. Furthermore, the pH-adjusted antibody solution was kept at RT until it reached a reaction temperature of 20-25°C. Meanwhile, one tube of IRDye800CW was thoroughly mixed with 25 µL of ultra-pure water (provided in the kit) by vortexing. Next, dissolved IRDye800CW and the antibody solution were thoroughly mixed and protected from light for a reaction time of 2 h at RT. Furthermore, Zeba™ Spin Desalting Columns (#89882, Thermo Fisher) were equilibrated with 50 mM phosphate buffer (pH 8.5) for appropriate buffer exchange. Subsequently, the antibody-dye mixture was put onto PBS-equilibrated desalting columns (pH 7.4) and centrifuged at 1,500 x g for 2 min to separate conjugate from free dye[130]. While free dye was discarded, conjugated antibodies were captured in tubes and stored at 4°C (in the dark) until use *in vivo*. Using this protocol, a conjugated dye:protein ratio of 1.5-2 was achieved. Similarly, control agents (non-specific IgG-800) consisted of non-specific IgG (#50270683, Thermo Fisher), which were covalently conjugated to IRDye800CW, as described above.

1.8.6. Systemic delivery of optical imaging agents and imaging

For systemic application of optical imaging agents, adult (4-6 weeks) wild-type CD1 mice were tail-vein injected with Nptn-800, Cntn2-800 or non-specific IgG-800 (dose indicated at each figure, respectively). Tail-vein injection was performed under inhaled sedation of 3.5% isoflurane, surface ECGs were taken, and mice were carefully monitored for any systemic reaction. 24-48 h post injection, mice were sacrificed, and hearts were harvested. NIR-signal was either immediately imaged using open NIR-detection (SPY Elite) or closed-field NIR-

detection (Pearl® Trilogy Small Animal Imaging System), or hearts were further processed per IHC or iDISCO+ protocol, as detailed above. During the IHC process, primary and secondary antibodies against gold standard conduction markers (Hcn4 or Cx40) were used as positive controls, however no additional primary anti-Nptn or anti-Cntn2 antibody was applied.

1.9. Results

1.9.1. Discovery of cardiac conduction system-specific cell surface markers

ScRNA-seq data of the murine cardiac conduction system (described in Part I) were used in this part of the study to uncover cell surface markers enriched or exclusive to CCS components (compared to all other cell types within the heart). First, the top 250 genetic markers showing highest enrichment within CCS cell clusters (cluster 9 of zone I=SAN cluster, cluster 4 of zone II=AVN/His cluster, cluster 13 of zone III=BB/PF cluster) were extracted *in silico*. All genes were prioritized by 1. Log fold enrichment within the CCS as compared to other cell types; and 2. Significance ("adjusted *p*-value" based on the Bonferroni correction). Next, subcellular localization analysis was performed using SurfaceGenie[131], a tool for rational candidate cell surface marker identification. The cell surface localization was further manually confirmed using Uniprot Knowledgebase (https://www.uniprot.org/help/uniprotkb). As a result, a host of CCS component-enriched markers were identified, that display a significant extracellular portion and thus present ideal targets for antibody-based targeting of conduction tissues (**Table 2.1**).

1.9.1. Neuroplastin is enriched in all components of the murine conduction system

Our data analysis has revealed Neuroplastin (*Nptn*) as a novel CCS-cell surface marker. In fact, especially strong *Nptn* gene expression was found within cluster 9 of zone I (SAN- 0.629 avg log FC, adjusted *p*-value = 1.64×10^{-36}) and cluster 13 of zone III (BB/PF - 0.335 avg log FC, adjusted *p*-value = 3.79×10^{-12}). While *Nptn* was not initially found to be significantly enriched within AVN/His cells when compared to all other cell types as demonstrated in Table 4, it was indeed significantly enriched when compared specifically to all other cardiomyocytes (AVN/His- *Nptn*: 0.303 avg log FC, adjusted *p*-value = 4.69×10^{-22}). Of note, *Nptn* has never been associated with any cardiac cell type before.

SAN			AVN/His			PF		
Gene	Avg log FC	Adjusted p value	Gene	Avg log FC	Adjusted p value	Gene	Avg log FC	Adjusted p value
Hcn4	0.60	1.29E-247	*Cacna2d2*	0.88	2.22E-308	*Cacna2d2*	1.21	2.22E-308
Cacna2d2	1.41	3.30E-224	*Slc22a1*	1.72	2.22E-308	*Slc16a12*	0.64	2.22E-308
Ntm	0.75	4.97E-81	*Ramp1*	1.02	7.20E-126	*Slc22a1*	0.67	7.50E-185
Gfra2	0.32	1.40E-61	*Pirt*	0.30	1.17E-111	*Gja5*	0.97	1.17E-183
Slc24a2	0.35	2.23E-58	*Perp*	0.87	6.77E-110	*Adgrb2*	0.37	2.83E-181
Plppr1	0.33	5.49E-54	*Kcnj5*	0.42	4.33E-102	*Slco3a1*	0.85	6.02E-157
Pcdh17	0.63	6.01E-53	*Ntm*	0.55	1.20E-101	*Ephb3*	0.52	4.68E-115
Gde1	0.71	1.15E-51	*Cacna1g*	0.39	9.57E-96	*Sdc4*	0.69	2.43E-113
Kcnj5	0.71	1.94E-51	*Fras1*	0.35	2.87E-90	*Ntm*	0.61	6.32E-110
Clic5	0.53	7.90E-48	*Parm1*	0.51	4.05E-89	*Slc6a6*	1.02	1.19E-99
Ank1	0.74	1.15E-44	*Epha4*	0.45	1.02E-81	*Scn5a*	0.76	4.81E-86
Adora1	0.47	5.27E-44	*Fxyd1*	0.64	1.92E-78	*Trabd2b*	0.38	2.12E-81
Tenm4	0.55	7.76E-43	*Rxfp1*	0.38	4.84E-77	*Corin*	1.10	2.70E-73
Cacna1h	0.39	6.31E-42	*Adora1*	0.28	7.23E-76	*Epha4*	0.57	9.25E-68
Trabd2b	0.59	1.82E-40	*Kcne1*	0.98	3.59E-75	*Slit2*	0.69	2.57E-62
Ramp1	0.91	2.04E-40	*Fitm1*	0.60	5.54E-74	*Kcnk3*	0.64	1.57E-58
Fitm1	0.62	6.75E-38	*Tmem51*	0.37	8.58E-71	*Ramp1*	1.04	1.18E-57
Gria1	0.41	1.02E-37	*Chrm2*	0.32	5.02E-70	*Sulf2*	0.89	5.18E-57
Nptn	0.63	1.64E-36	*Gpc1*	0.42	8.14E-69	*Alcam*	0.42	5.48E-54
Enpep	0.38	2.48E-35	*Cap2*	0.44	9.78E-68	*Sorcs2*	0.28	2.23E-51
Adcy5	0.47	9.56E-35	*Bcam*	0.49	2.38E-67	*Hfe2*	0.30	1.51E-44
Cacna1g	0.30	5.54E-34	*Slitrk5*	0.27	2.16E-60	*Parm1*	0.61	4.28E-42
Slc38a2	0.70	1.20E-31	*Kcnk3*	0.31	9.97E-56	*Fxyd1*	0.72	8.62E-41
Xirp1	0.48	3.97E-31	*Ddr1*	0.34	1.08E-54	*Bcam*	0.68	4.51E-40
Adam33	0.49	7.57E-31	*Furin*	0.36	1.74E-54	*Igf2r*	0.75	5.84E-38
Popdc2	0.57	1.82E-30	*Popdc2*	0.47	1.58E-52	*Fam174b*	0.43	6.89E-37
Enpp1	0.31	3.19E-30	*Cav3*	0.44	3.51E-51	*Trdn*	0.70	5.48E-36
Pirt	0.39	1.70E-29	*Slc25a4*	0.51	5.07E-51	*Itgb5*	0.50	1.20E-29
Lrrn2	0.39	2.73E-29	*Kcng2*	0.32	9.10E-50	*Gpr22*	0.44	1.43E-28
Adgrb2	0.27	4.53E-29	*Bves*	0.53	5.61E-47	*Slc22a17*	0.35	7.09E-28
Cacna1d	0.29	6.30E-29	*Sgcg*	0.38	1.04E-46	*Gipr*	0.28	2.00E-27
Slc25a4	0.53	6.34E-29	*Jph2*	0.34	1.34E-46	*Serinc1*	0.52	5.36E-27
Zdhhc2	0.53	1.51E-28	*Cxadr*	0.30	3.20E-46	*Nlrp10*	0.26	6.96E-24
Unc45b	0.46	3.40E-28	*Sspn*	0.36	6.12E-45	*Gpc1*	0.41	7.53E-24
Cav1	0.52	5.19E-28	*Itgb1bp2*	0.30	9.77E-45	*Dag1*	0.48	4.38E-23
Furin	0.70	8.93E-28	*Vldlr*	0.39	7.22E-43	*Lpl*	0.55	1.74E-22
Kcnh2	0.39	2.29E-27	*Cdh13*	0.36	1.27E-39	*Chrm2*	0.39	1.95E-22
Jph2	0.50	7.29E-27	*Tmem38a*	0.29	3.40E-38	*Spint2*	0.36	1.55E-21
Fras1	0.55	1.92E-26	*Slc22a17*	0.27	1.29E-37	*Pdpn*	0.26	1.14E-20
Unc5b	0.49	2.69E-26	*Slc2a1*	0.28	3.73E-35	*Inafm2*	0.30	2.59E-19
Ank3	0.49	1.10E-24	*Arhgap31*	0.47	3.83E-35	*Cdh13*	0.45	9.34E-19
Lmo7	0.47	7.79E-23	*Itga9*	0.30	1.44E-34	*Rxfp1*	0.26	1.22E-18
Efnb2	0.32	1.40E-21	*Smim5*	0.27	1.79E-33	*Itm2b*	0.62	1.42E-18
Slco3a1	0.41	1.62E-21	*Cdh2*	0.35	5.97E-33	*Plxna4*	0.26	1.54E-18
Vldlr	0.48	1.87E-20	*Slc25a3*	0.32	7.29E-32	*Furin*	0.32	1.09E-16
Fzd7	0.28	7.67E-19	*Tmx4*	0.33	2.85E-31	*Serinc3*	0.41	1.59E-15
Shisa4	0.33	1.14E-18	*Dag1*	0.31	3.06E-28	*Sgca*	0.27	1.98E-15
Sspn	0.46	1.72E-18	*Ptgfrn*	0.26	1.88E-24	*Tspan2*	0.30	2.42E-15
Nid2	0.40	3.27E-18	*Arhgef7*	0.25	5.18E-23	*Fitm1*	0.45	6.67E-15
Lrrc4b	0.32	5.10E-18	*Prnp*	0.42	6.12E-23	*Unc5b*	0.26	1.43E-14
Sulf2	0.49	1.18E-17	*Lpl*	0.26	4.74E-18	*Sspn*	0.36	5.41E-14
Svil	0.43	1.65E-17	*Tnfrsf12a*	0.27	1.10E-16	*App*	0.44	8.36E-14
Kcng2	0.33	6.55E-16	*Igf2r*	0.29	1.25E-16	*Llfr*	0.29	9.54E-14
Fxyd1	0.38	1.37E-15	*Ehd4*	0.26	5.07E-16	*Kcng2*	0.38	1.07E-13
Slc25a3	0.32	2.99E-15				*Itgav*	0.27	1.45E-13
Vdac1	0.36	4.43E-15				*Lrrc4b*	0.27	1.79E-13
Cap2	0.38	7.74E-15				*Slc38a10*	0.34	4.08E-13
Gpc1	0.41	4.97E-14				*Adgrl1*	0.26	1.20E-12
Plppr5	0.33	2.14E-13				*Kctd12*	0.34	3.30E-12
Ddr1	0.37	4.66E-13				*Nptn*	0.34	3.79E-12
Chrm2	0.38	8.52E-13				*Dsg2*	0.25	6.19E-12
Cacnb2	0.30	1.50E-12				*Pcdh7*	0.41	1.43E-11
Naaladl2	0.28	3.29E-12				*Perp*	0.36	3.72E-11
Bcam	0.32	6.69E-12				*Tspan3*	0.38	5.26E-11
Cdon	0.26	2.50E-11				*Tmem161a*	0.27	6.45E-11
Xpr1	0.33	3.82E-11				*Tmem176a*	0.32	7.79E-11
Parm1	0.34	5.27E-11				*Cdh2*	0.33	1.04E-10
Dmd	0.34	9.30E-11				*Kcne1*	0.67	1.63E-10
Tmem65	0.36	9.60E-11				*Tmem38a*	0.34	2.72E-10
Sort1	0.32	6.21E-10				*Inppl1*	0.27	3.39E-10
Slc22a17	0.26	2.82E-09				*Pmp22*	0.26	4.00E-10
Slc25a23	0.29	5.58E-09				*Fndc3b*	0.29	8.67E-10
Aplp2	0.28	6.54E-09				*Cd81*	0.25	4.19E-09
Kcnj3	0.32	9.48E-09				*Ncam1*	0.31	1.14E-08
Magi3	0.28	3.22E-07				*Dmd*	0.26	3.22E-08
Bambi	0.31	5.53E-07				*Tmem30a*	0.29	4.71E-08
Rxfp1	0.31	2.35E-04				*Cacna2d1*	0.25	6.27E-08
Tnfrsf12a	0.34	3.29E-04				*Ddr1*	0.28	7.93E-08
						Sgcg	0.25	8.35E-08
						Antxr2	0.31	1.14E-07
						Adam10	0.27	1.80E-06
						Ptp4a2	0.30	1.28E-04
						Rrad	0.27	1.91E-04
						Gpc3	0.30	2.06E-04
						Slmap	0.26	2.40E-04
						Wls	0.27	3.39E-04
						Cav3	0.27	7.44E-04
						Slc38a2	0.27	3.86E-03

Table 2.1: Cell surface markers enriched in specific conduction system components
List of differentially expressed genes enriched within each major component of the cardiac conduction system (CCS) as compared to all other cardiac cell types. Analyses performed on single-cell RNA-sequencing (scRNA-seq) dataset from microdissected CCS tissue of wild-type, embryonic day 16.5 (E16.5) mouse hearts. Known CCS genes highlighted in blue. Avg log FC indicates average log fold change; Adj *p* value: adjusted *p* value; AVN: atrioventricular node; His: His Bundle; SAN: sinoatrial node; PF: Purkinje fiber. From[119].

In order to validate *Nptn*-enrichment within all key CCS cell types at the protein level, IHC analysis was next performed on murine heart sections. Consistent with our scRNA-seq findings, IHC analysis revealed the existence of Nptn protein in all major components of the CCS including the SAN, AVN, His bundle, BB as well as the PF system in mice (**Figure 2.3**). Of note, little or no Nptn protein was detected in non-conduction cell types within the heart.

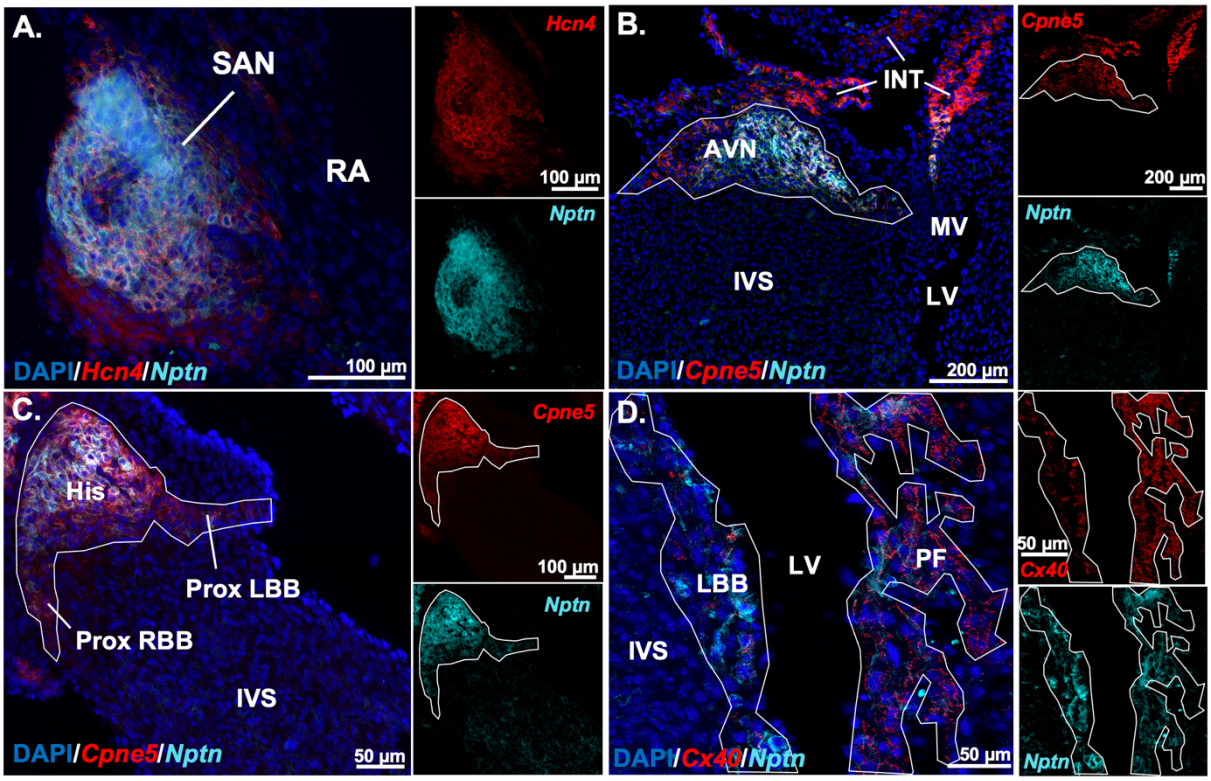

Figure 23: Neuroplastin is enriched within all components of the murine cardiac conduction system
Immunofluorescence staining of wild-type murine, postnatal day 10 (P10) cardiac tissue sections. **A.** Sinoatrial node (SAN) tissue sections. Gold-standard SAN marker Hcn4 (red) and specific co-labeling with Nptn (cyan). **B.** Atrioventricular node (AVN) labeled by the known CCS-marker Cpne5 (red) and specific co-labeling with Nptn (cyan). **C.** His bundle (His), right bundle branch (RBB) and left bundle branch (LBB) indicated by known CCS-marker Cpne5 (red) and specific co-labeling with Nptn (cyan). **D.** Purkinje fibers (PF) and bundle branches (BB) marked by Cx40 (red) and Nptn (cyan). DAPI (blue) in all panels. INT indicates internodal tracts; IVS: interventricular septum; LV: left ventricle; MV: mitral valve; Prox: proximal; RA: right atrial myocardium; VM: ventricular myocardium. Modified from[119]

1.9.2. Neuroplastin is enriched in all components of the human conduction system

To assess, whether NPTN could represent a viable cell surface marker for human use, the NPTN expression pattern was further analyzed within the human heart. In this regard, human cardiac conduction system tissue samples (adult, n=1, 45 years; Infant, n=1, 11 months) with PMIs shorter than 24 h were acquired from the tissue bank of the pathology department at Stanford University and were appropriately de-identified.

As a result, NPTN was found to be specifically expressed within key CCS components, including the SAN, INT, His bundle and BB of the infant human heart (11-month-old) (**Figure 2.4**). Additionally, strong IHC signal was found in adult cardiac conduction tissues (45-year-old) (**Figure 2.5**) demonstrating robust CCS-specific NPTN expression both in the first year of life and in adulthood.

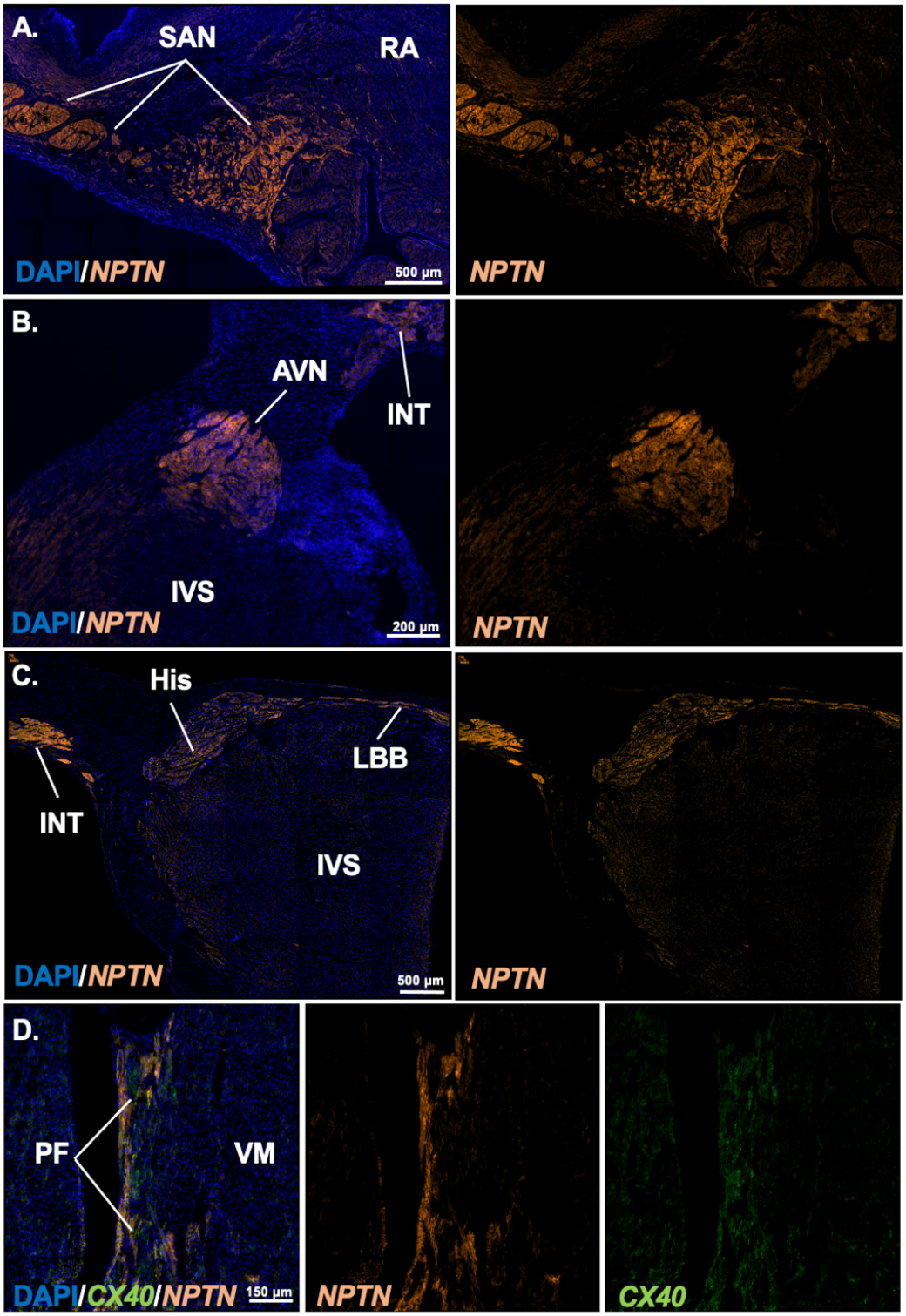

Figure 24: Neuroplastin presents a robust cell surface marker labeling cardiac conduction system components in the infant human heart

Immunofluorescence staining of cardiac tissue sections from an 11-month-old human heart stained with anti-NPTN (orange) specifically staining all major components of the cardiac conduction system (CCS). **A.** Sinoatrial node (SAN) region; **B.** Atrioventricular node (AVN) and internodal tracts (INT); **C.** Internodal tracts, His bundle (His) and left bundle branch (LBB); and **D.** Purkinje fibers (PF) co-stained with Connexin 40 (CX40). DAPI (blue). RA indicates right atrial myocardium; IVS: interventricular septum; VM: ventricular myocardium.

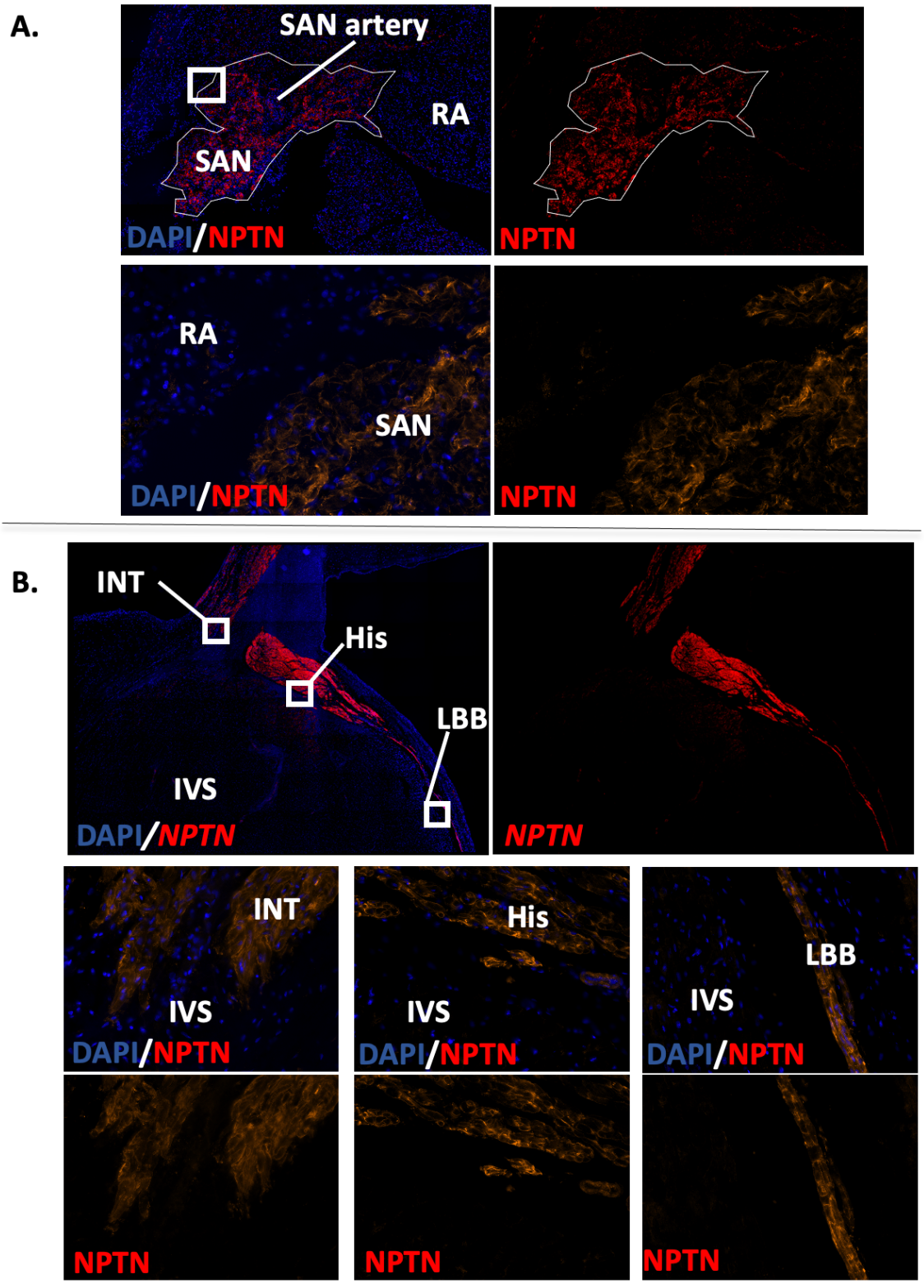

Figure 25: Neuroplastin is specifically expressed within the cardiac conduction system in the adult human heart
Heart tissue was acquired from the Stanford pathology department of a 45-year-old human subject. **A.** Sinoatrial node (SAN) region stained for Neuroplastin (NPTN) (red) and DAPI (blue). Conduction cells surrounding the SAN artery are clearly stained positive for NPTN, while the myocardium of the right atrium (RA) is not. Lower two images represent the content within the bracketed white box in higher magnification. **B.** His bundle (His) / bundle branch (BB) region stained for NPTN (red) and DAPI (blue). Lower six images represent the content within the bracketed white boxes in higher magnification (left: INT; middle: His; right: LBB). INT: internodal tract; IVS: interventricular septum; RBB: right bundle branch.

1.9.3. Systemic delivery of anti-Nptn antibodies labels the murine conduction system *in vivo*

In order to assess the *in vivo* antibody-binding efficiency to Nptn, an optical imaging tool called "Nptn-800" was created, consisting of a commercially available polyclonal anti-Nptn antibody covalently conjugated to a NIR-dye (IRDye800). Controls consisted of wild-type mice injected with nonspecific IgG conjugated to the same NIR dye ("IgG-800"). Following a single intravenous tail vein injection of Nptn-800 (150 µg), wild-type, CD1 mice were sacrificed after 24 h. Their hearts and other major organs were then isolated and processed for analysis of antibody-binding specificity using a closed-field NIR imaging system (**Figure 2.6**).

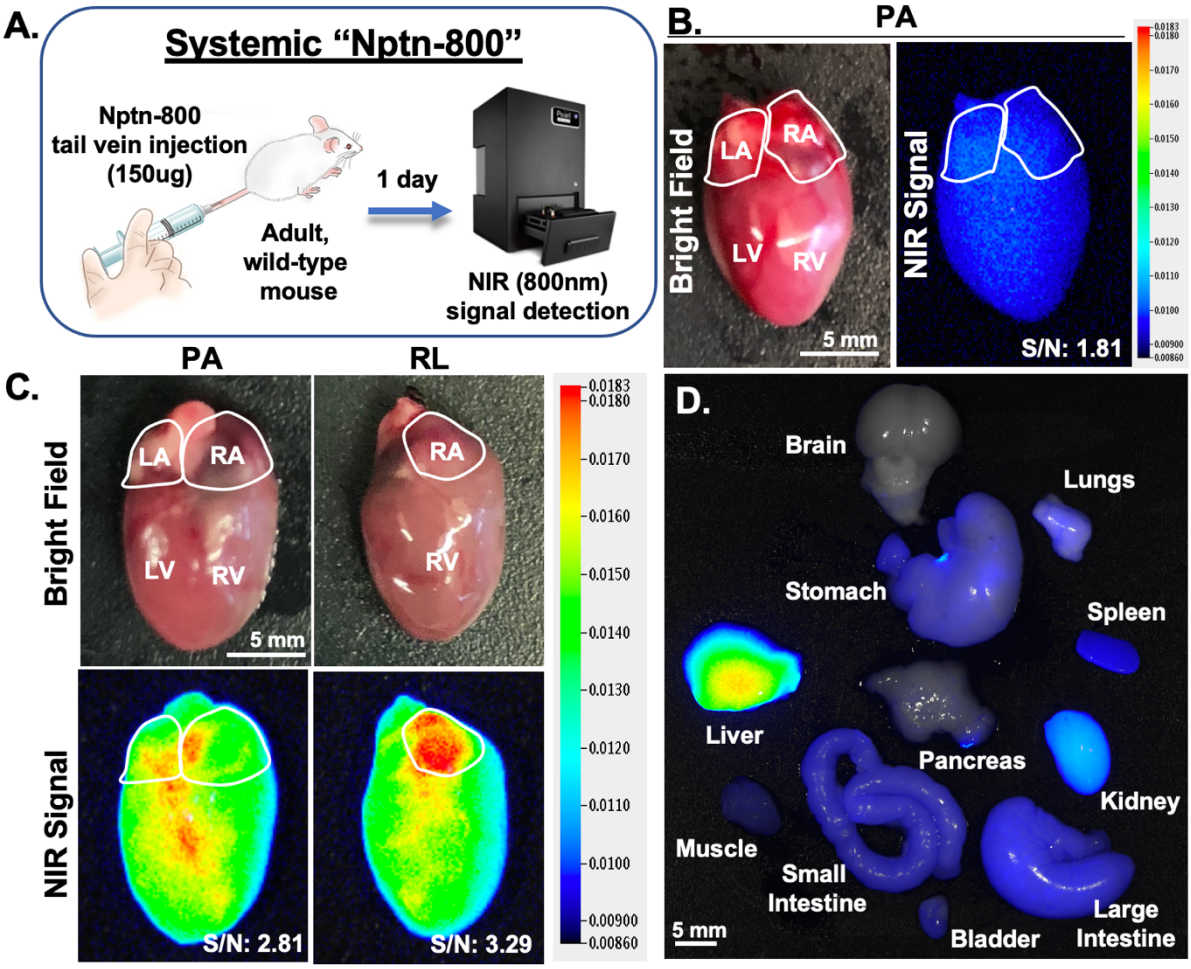

Figure 26: Systemic injection of Nptn-800 labels the cardiac conduction system in vivo

A. Experimental workflow. **B.** Whole heart from control mice injected with nonspecific IgG-800 showing no specific near-infrared (NIR) signal. **C.** Whole heart from a wild-type (CD1) mouse injected 1 day prior with Nptn-800. Heart shown in posterior-anterior (PA) and right lateral (RL) views. Atria outlined in white and left ventricle (LV) and right ventricle (RV) labeled accordingly. LA indicates left atrium; LV: left ventricle; RA: right atrium; RV: right ventricle. Top: Brightfield. Bottom: NIR signal demonstrating labeling of the presumptive cardiac conduction system (CCS) (Blue-Red = Lowest-Highest signal). Mean signal to background ratio (SBR) as indicated. **D.** Whole-body biodistribution of fluorescent signal in other tissue types (Blue-Red = Lowest-Highest signal). Modified from[119].

While no specific signal was detected in the hearts of mice injected with IgG-800 (**Figure 2.6B**), CCS-specific signal was detected in intact, whole hearts in regions consistent with the CCS using closed-field NIR imaging (**Figure 2.6C**). Outside of the heart, NIR signal was detected expectedly within the liver and kidneys similar to prior reports of metabolism and clearance

of other NIR imaging agents (**Figure 2.6D**)[132]. Notably, Nptn-800 signal was not detected within brain tissues, despite the brain being the only other major organ besides the CCS known to express *Nptn*[133]. These findings are consistent with the incapability of full IgG antibodies to cross an intact blood-brain barrier.

Next, isolated hearts were processed for analysis of antibody-binding specificity at the cellular level in serial heart sections (**Figure 2.7**). Strikingly, Nptn-800 signal was detected throughout the CCS with high specificity (namely in the SAN, AVN, His, BB and PF), whereas no significant signal was found in other cardiac cell types.

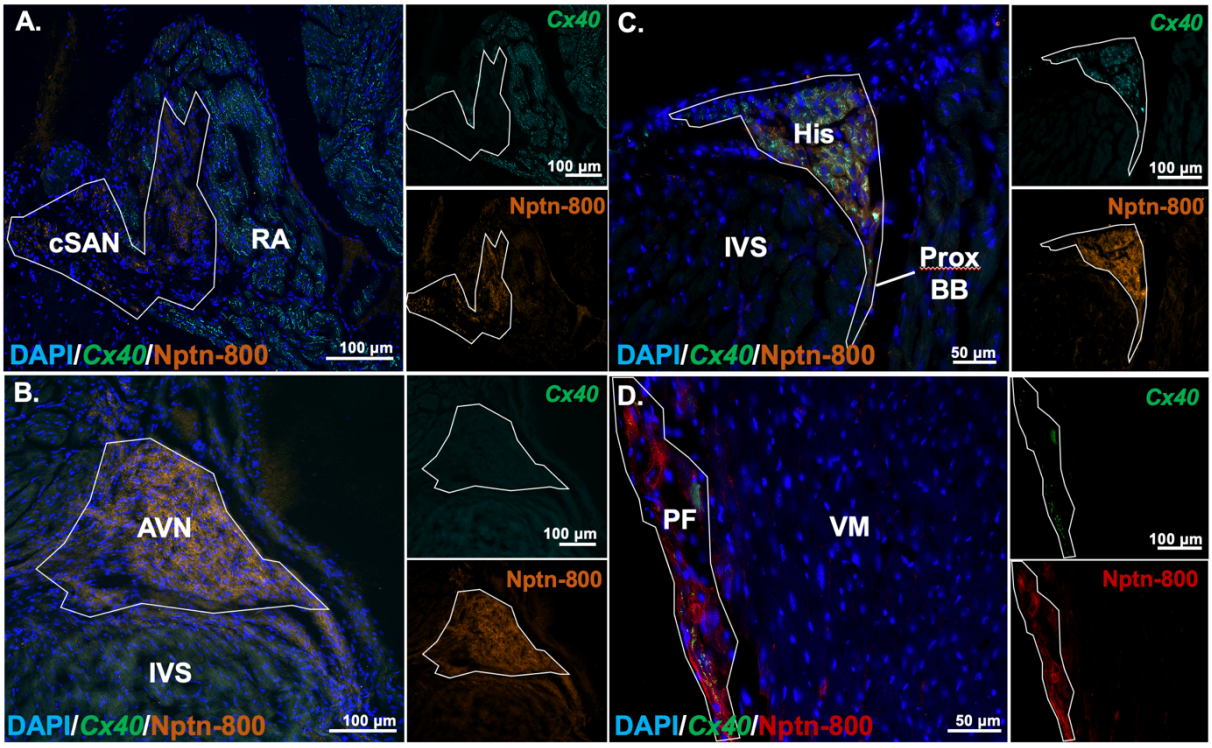

Figure 27: Precise labeling of all cardiac conduction system components following systemic injection of Nptn-800

Nptn-800 consists of a commercially available polyclonal anti-Nptn antibody chemically conjugated to a near infrared fluorescent dye. 150 µg of Nptn-800 was systemically delivered to wild-type CD1 mice. Next, hearts were isolated and processed for serial sections 48 h post injection. Cx40 (cyan) was stained per regular immunohistochemistry protocol, whereas Nptn-800 (red) displays signal derived from the systemically delivered fluorescent probe. **A.** SAN region of murine heart section. SAN ($Cx40^-$, $Nptn\text{-}800^+$), RA ($Cx40^+$, $Nptn\text{-}800^-$). **B.** AVN region of murine heart section. AVN ($Cx40^-$, $Nptn\text{-}800^+$), IVS ($Cx40^-$, $Nptn\text{-}800^-$). **C.** His region of murine heart section. His ($Cx40^+$, $Nptn\text{-}800^+$), IVS ($Cx40^-$, $Nptn\text{-}800^-$). **D.** PF region of murine heart section. PF ($Cx40^+$, $Nptn\text{-}800^+$), IVS ($Cx40^-$, $Nptn\text{-}800^-$). AVN indicates atrioventricular node; His: bundle of His; INT: internodal tract; IVS: interventricular septum; RA: right atrium; RBB: right bundle branch; SAN: sinoatrial node.

1.9.4. Anti-Cntn2 antibodies similarly label the murine conduction system *in vivo*

As a combination of antibodies against two different CCS-specific targets could be beneficial to enhance signal intensity in the operating room, an alternative diagnostic tool was created targeting Contactin-2 (Cntn2), a previously known pan-CCS cell surface marker[75]. To this end, "Cntn2-800" consists of a polyclonal anti-Cntn2 antibody covalently conjugated to a NIR fluorescent dye, adding an additional tool to our repertoire, and further reinforcing the *in vivo* applicability of optical imaging agents for the CCS.

Thus, the efficacy of this tool was similarly validated by systemically injecting wild-type, CD1 mice with a single dose of Cntn2-800 (75 µg). Hearts were harvested after 72 h and further processed for serial heart sections. Tissues were then stained for well-known CCS-markers (Hcn4: SAN/AVN/His; Cx40: PF). As a result, Cntn2-800 signal was found to specifically co-label conduction cells in all CCS components, proving precise *in vivo* labeling of the entire murine CCS (**Figure 2.8**).

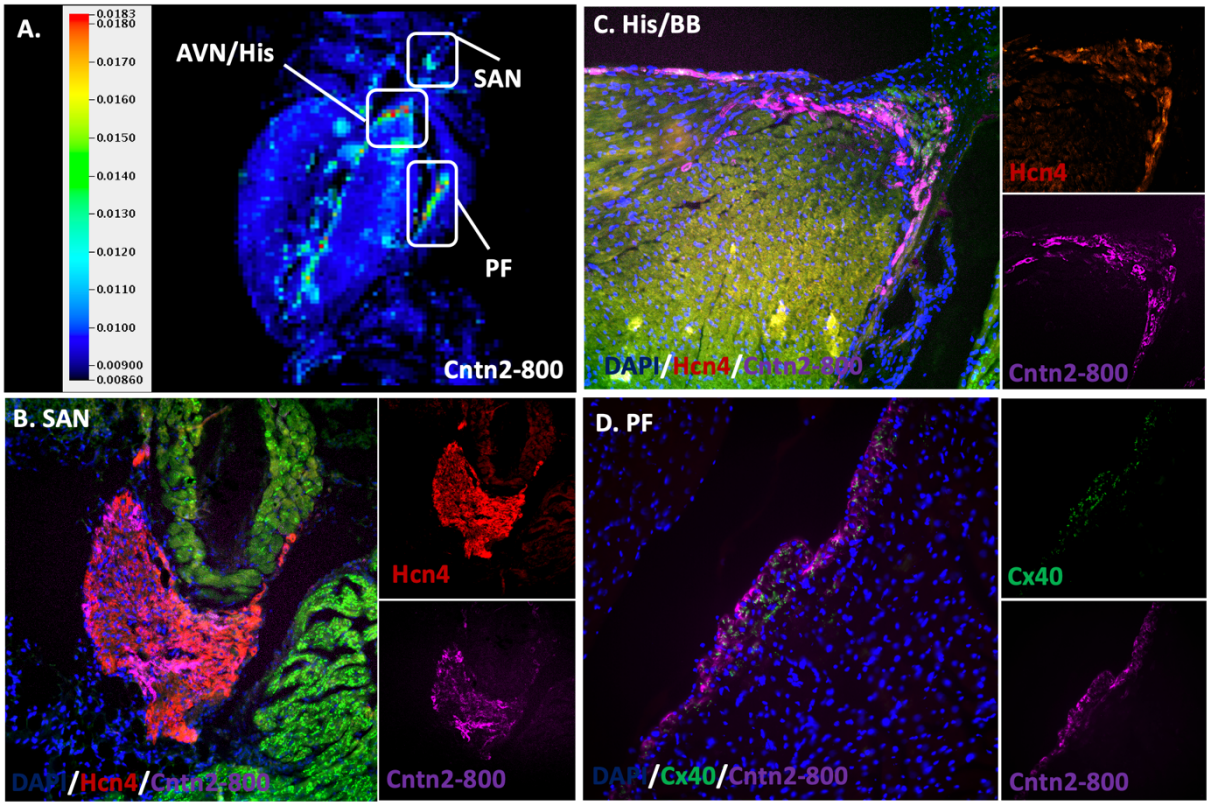

Figure 28: Cntn2-800 specifically labels all components of the murine cardiac conduction system following systemic delivery

A: Heart section from an adult mouse injected 72 h prior with Cntn2-800. Near infrared (NIR) signal demonstrates labeling of the cardiac conduction system (CCS) (Blue->Red = Lowest->Highest NIR signal). **B-D:** Magnified images of the CCS components labeled with Cntn2-800 (Purple) and co-stained with known CCS-markers anti-Hcn4 (Red) or anti-Cx40 (Green). DAPI (Blue, nuclei). AVN indicates atrioventricular node; BB: bundle branches; His: His bundle; PF: Purkinje fibers; SAN: sinoatrial node. From[119]

Finally, hearts from mice that have received a single tail-vein injection of Cntn2-800 (75 µg) were isolated, fixed in PFA per the above-described protocol, optically cleared (per iDISCO+ protocol) and imaged using light sheet microscopy. Due to fluorescence signal quenching following extensive PFA fixation of heart tissues, Cntn2-800 signal was enhanced using only an Alexa 647 anti-goat secondary antibody, specifically with no primary antibodies. More than 750 images were taken at 3 µm thickness through the entire mouse heart capturing Cntn2-800 NIR signal in the entire heart. As a result, light sheet imaging and 3D reconstruction of entire mouse hearts showed exquisite resolution and high specificity of Cntn2-800 to all components of the CCS, including the SAN, INT, AVN, His, BB and PF after systemic delivery (**Figure 2.9**).

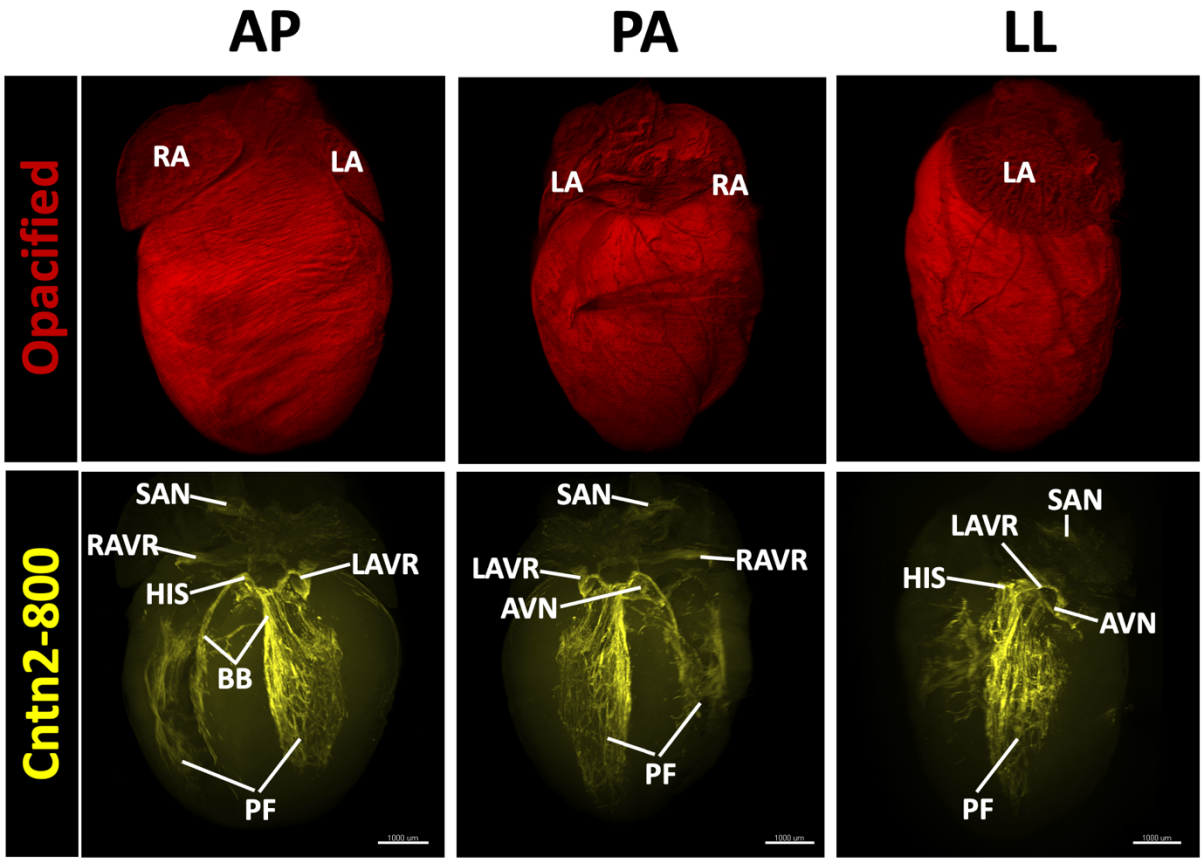

Figure 229: Precise Cntn2-800 distribution assessment in whole hearts
Immunolabeling-enabled three-dimensional imaging of solvent-cleared organs (iDISCO+)- cleared heart harvested from a wild-type (CD1) mouse injected two days prior with Cntn2-800 (75 µg). Heart shown anterior-posterior (AP), posterior-anterior (PA) and left-lateral (LL). Top and bottom rows are the same optically cleared heart using iDISCO+ where, in the top row, background fluorescence has been saturated to provide a representation of the opacified heart. Bottom row demonstrates the same tissue-cleared heart, showing signal from Cntn2-800 marking the entire cardiac conduction system (CCS). Conduction system components are labeled as indicated. AVN indicates atrioventricular node; His: His bundle, INT: internodal tracts; LA/RA: left or right atrium; LAVRB: left AV ring bundle; LBB/RBB: left of right bundle branch; LV/RV: left or right ventricle; PF: Purkinje fiber; RAVRB: right AV ring bundle; SAN: sinoatrial node. Modified from[119]

1.9.5. Validation of novel diagnostic tools using intraoperatively established imaging systems

Having assessed Cntn2-800 specificity and sensitivity at both the cellular and whole organ levels, further preclinical validation was performed in the mouse model using an intraoperatively established imaging system (SPY Elite) which was previously shown to detect antibody-IRDye800 bioconjugates intraoperatively in humans[120]. In this regard, wild-type, CD1 mice were tail-vein injected with a single Cntn2-800 dose of 100 µg, animals were sacrificed 24 h post systemic delivery, hearts were isolated, and immediately sectioned in order to display conduction system components. Next, hearts were imaged with SPY Elite systems. High intensity NIR signal was detectable from all CCS components, including the SAN, AVN, His, BB and PF (**Figure 2.10**). Of note, even smallest conduction structures could be visualized at submillimeter resolution (BB and fine PF in mice). As conduction system components in humans are far larger than in mice, these studies suggest adequate resolution for the human heart using established NIR imaging equipment for surgical use.

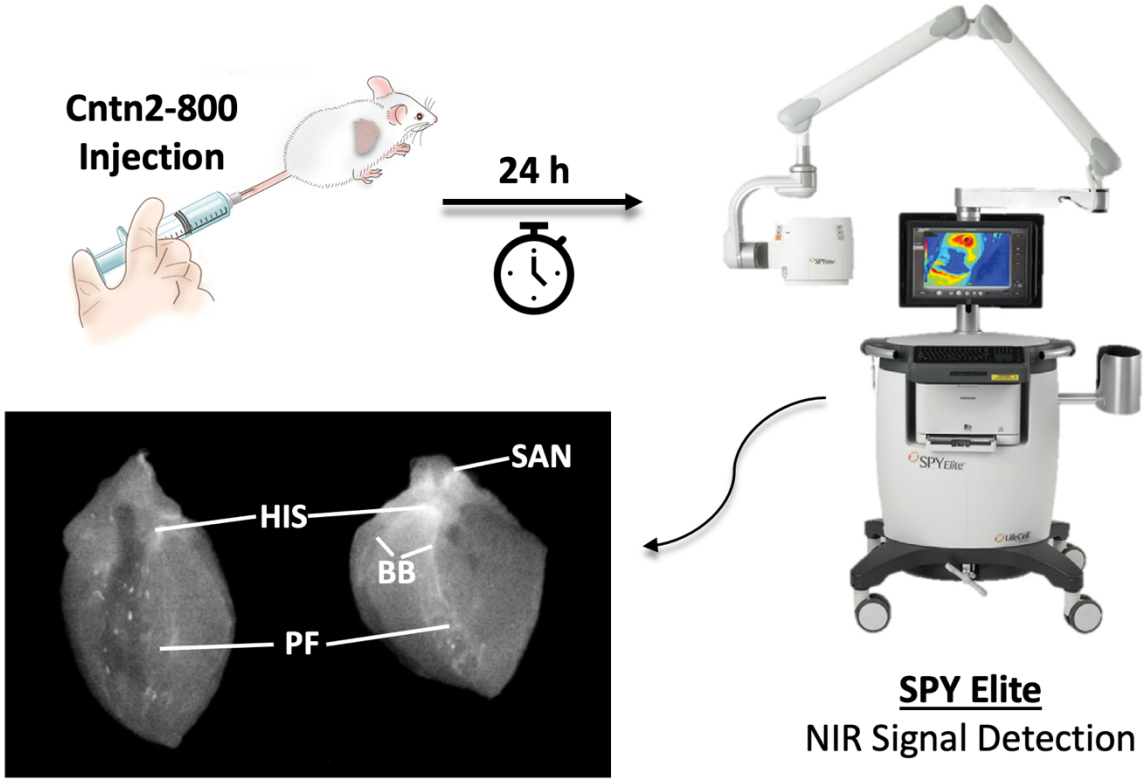

Figure 2.10: Preclinical validation of Cntn2-800 using established intraoperative imaging systems
Wild-type, CD1 mice were tail-vein injected with a single Cntn2-800 dose of 100 µg, animals were sacrificed 24 h post systemic delivery, hearts were isolated, and immediately sliced open coronally in order to display conduction system components. Further, hearts were imaged with SPY Elite systems. As a result, high intensity NIR signal was detectable from exposed cardiac conduction system (CCS) components at submillimeter resolution. BB indicates bundle branches; HIS: bundle of His; NIR: Near-infrared; PF: Purkinje fibers; SAN: sinoatrial node.

1.10. Discussion

Part II of this study exploits the large scRNA-seq dataset (described in Part I) and presents the discovery of multiple novel cell surface markers highly enriched within the entire CCS or individual CCS components (**Table 2.1**). Furthermore, this study has uncovered Neuroplastin (*Nptn*) as a novel cell surface marker not previously associated with the conduction system (**Figures 2.3**-**2.7**). From a host of novel CCS-enriched cell surface markers, *Nptn* was chosen for further validation for the following reasons: 1. significant *Nptn* enrichment within all key components of the CCS at the mRNA level; 2. high specificity to the conduction system with only minor expression within non-conduction cell types; 3. conserved CCS-specific expression in multiple species including mice (**Figure 2.3**) and humans (**Figure 2.4**); and 4. its significant extracellular protein portion[134], making NPTN an ideal target for *in vivo* antibody-targeting. Overall, these findings substantiate *Nptn* as a novel CCS-specific cell surface marker ideal for the generation of new optical imaging agents.

Subsequently, this discovery was leveraged to create novel antibody-based optical imaging tools allowing for real-time visualization of cardiac conduction tissues. Specifically, using both newly discovered (Nptn) and previously known (Cntn2) cell-surface makers of the CCS, optical

imaging agents (Nptn-800 and Cntn2-800, respectively) were successfully created with high sensitivity and specificity for labeling the entirety of the CCS (**Figures 2.7, 2.8**) *in vivo*. Lastly, using an intraoperatively established imaging system (SPY Elite, Stryker, USA) strong signal and high-resolution detection of even fine CCS structures in mice (**Figure 2.10**) was proven. Thus, novel antibody-based optical imaging tools generated in this study present a promising new way for the real-time intraoperative visualization of the CCS with the potential to prevent direct surgical damage to the CCS and to reduce morbidity and mortality in both pediatric and adult patients alike.

To the best of my knowledge, the current study is the first to present antibody-based targeting of any substructure within the heart and thus describes an entirely new field within cardiac medicine.

1.10.1. Current knowledge about Neuroplastin

Here, Neuroplastin (*Nptn*) was uncovered presenting a novel cell surface marker highly specific to all CCS components in both mice and human. While not previously associated with the heart, *Nptn* was first identified in 1988 as a membrane-bound, mostly extracellular glycoprotein within synapses of the brain[133]. Functionally, *Nptn* is known to serve as a key player in multiple neuronal and synaptic processes including neurite outgrowth, synaptic plasticity and the regulation of cerebral inhibitory and excitatory synapses[134]. Specifically, Nptn has been implicated in FGF receptor activation[135], hippocampal synapse structure formation[136] and long-term potentiation in the brain through p38MAPK activation and glutamate receptor subunit 1 (GluR1) internalization[137,138]. Moreover, Nptn is involved in neuronal metabolism through transportation of monocarboxylates and was further reported to regulate the subcellular localization of specific binding partners[134]. However, the physiologic function of Nptn within the heart and its role in cardiac disease states remains unknown.

1.10.2. Neuroplastin as a marker for immunohistochemistry in human tissues

In this study, strong *Nptn* gene expression was elucidated throughout all key components of both the murine and human CCS. Of note, IHC analysis of human conduction tissue is known to be extremely challenging due to a lack of functional antibodies as well as high tissue density and fibrosis[139]. Therefore, the research community is mostly limited to hematoxylin and eosin (H&E) or Masson‘s Trichrome stains to roughly delineate conduction tissue based on its higher fibrotic content[5]. However, IHC is a more sensitive technique as it allows to distinguish one cell type from another at cell-to-cell resolution. To this end, anti-NPTN staining was established in this study and now provides a new and reliable way to distinguish human cardiac conduction tissue from the surrounding myocardium in both newborn and adult cardiac tissues (**Figures 2.4**, **2.5**).

1.10.3. Previous attempts to visualize conduction tissues

Conventional imaging modalities are frequently used in the clinical field and include ultrasound, magnetic resonance imaging (MRI), computed tomography (CT), positron emission tomography (PET), and others. While these techniques can provide important anatomical and functional information, they are not suitable for intraoperative CCS imaging.

First attempts towards the generation of intraoperative CCS detection methods were introduced in the 1970s aiming at electrophysiological identification[140–142]. These methods

utilize intraoperative atrial pacing and the following observation of changes in electrocardiograms (ECG) to detect surgical injury intraoperatively. Further, using a special detection probe, this technique allows for the rough localization of conduction tissues during cardiac surgery. However, the reliance on atrial pacing and low-resolution detection remains a significant limitation of this method.

Decades later, Huang et al. from the University of Utah introduced a novel approach based on fiberoptic confocal microscopy (FCM) and fluorescent labeling of the extracellular space[143–145]. This group detected differences in tissue microstructure between nodal and working myocardium. Specifically, the atrial myocardium consists of highly aligned myocytes with a regularly striated arrangement whereas nodal tissue presents an irregular reticular arrangement of the extracellular space[143]. Thus, the use of dextran conjugated to a specific fluorophore (Alexa Fluor 488) was used to target the extracellular space in an undirected manner, allowing for visualization of tissue microstructure. Upon intraoperative image processing, nodal tissue may be distinguished from atrial myocardium through image analysis. However, there are certain limitations associated with FCM-based approaches. Firstly, current FCM systems can only image CCS tissue to a depth of up to 50 µm[144]. Although most conduction tissues lie rather superficially underneath the epicardium (SAN) or endocardium (rest of the CCS), the practicability for clinical application of this penetration depth has yet to be evaluated. Further, while high spatial resolution at the submillimeter level is important for clinical use, exact borders between nodal tissue and neighboring myocardium cannot be drawn using FCM-based tools. Moreover, its reliance on fluorescent dyes that have not yet proven to be non-toxic in patients may present another drawback. Finally, CCS detection methods requiring image processing and quantitative analyses cannot provide real-time information and may therefore significantly disrupt the regular surgical workflow.

Therefore, antibody-based optical imaging presents the most promising real-time imaging technique for multiple reasons. Firstly, antibodies have been widely used in humans for both the diagnosis and treatment of multiple diseases and present well-established pharmacokinetics and safety profiles thus greatly reducing translational risks[120]. Moreover, highly tissue-specific antibody-binding characteristics allow for the visualization of precise tissue borders delineating the structure of interest from its surrounding tissues. Further, the use of FDA-approved high-resolution signal detection devices such as SPY Elite provides the unique opportunity to display real-time images in the surgical field of view (FOV) without disruption of surgical workflows[130].

1.10.4. Enhancement of signal intensity and penetration through near-infrared fluorophores

Key considerations in optical imaging are the ideal excitation and emission wavelengths of the fluorescent probe used. To this end, light emitted in the visible spectrum (380-780 nm) is absorbed in large part by molecules such as water and hemoglobin[146]. However, as NIR fluorescent probes range around the 700-900 nm wavelength spectrum, exciting light is barely absorbed, tissue autofluorescence is minimized and the signal-to-background ratio (SBR) is enhanced. Furthermore, the higher emission wavelength allows for deeper tissue penetration and thus imaging of structures up to a full centimeter underneath the organ surface is possible[147]. Of note, this technology has already been successfully exploited for intraoperative cancer detection at submillimeter resolution as demonstrated in numerous recently performed studies (**Figure 2.2**)[122,124].

Although indocyanine green (ICG) is a clinically approved diagnostic imaging dye in the NIR spectrum, it lacks a reactive functional group and can thus not be conjugated to targeting antibodies[129]. However, the NIR dye used in this study (IRDye800) exhibits excitation and emission wavelengths similar to ICG and can therefore be detected using FDA-approved imaging systems (such as SPY Elite), which promote fast clinical translation. Furthermore, the IRDye800 is manufactured under good manufacturing practice (GMP) conditions suitable for human use and was proven to be non-toxic in both rodents and humans[129,130].

1.10.5. Goggle-augmented imaging and navigation system

Several NIR imaging systems are currently established for clinical use, including FLARE[148], Fluobeam[149] and SPY Elite systems, as used in the current study. Recently, an interesting new imaging system was introduced providing less bulky hardware and a perfect match between the systems and surgeon's field of view. This system, called goggle-augmented imaging and navigation system (GAINS), directly projects an overlay of both natural brightfield images and NIR signal emitted from optical imaging agents onto head-mounted goggles without latency[150]. This technique might provide additional comfort for heart surgeons to visually detect CCS structures in real-time. Although clinical feasibility of GAINS was demonstrated in the operating room, current limitations include the lack of automated focusing and the reliance on a wired connection to a PC for final image processing. Thus, while the current study presents successful and clinically translatable high-resolution NIR signal detection using the FDA-approved imaging system SPY Elite, GAINS may provide interesting advancements to real-time fluorescence-guided surgery in the future.

1.10.6. Limitations of this study

To the best of my knowledge, this is the first study presenting an antibody-based optical imaging approach targeting substructures within the heart. Further, preclinical validation of the novel optical imaging agents has proven high-resolution and strong NIR signal detection in real-time at submillimeter resolution of even fine CCS structures. However, existing limitations of this study are discussed in the following paragraphs.

Firstly, while the FDA-approved SPY Elite imaging system was shown to provide high resolution images (**Figure 2.10**), it is equipped with filters for detection of ICG dyes. Of note, the emission wavelength of ICG (820-840 nm) is slightly higher than that for IRDye800 (780-800 nm)[151]. Therefore, while existing FDA-approved NIR imaging systems improve the time of clinical translation for our tools, new imaging systems designed for the precise detection of IRDye800 will be needed to further improve the SBR of Nptn-800 and Cntn2-800 in the future.

Furthermore, while this study has proven highly precise NIR signal detection even within fine CCS structures of the mouse heart (such as PF), mouse CCS structures may not be an appropriate representation of the human conduction system. Thus, large animal models are needed to assess sufficiency of signal penetration within larger organs. However, previous studies have indicated NIR signal penetration of up to a full centimeter through dense tissues[147]. Thus, as key CCS structures lie less than 1 cm underneath the organ surface (SAN, AVN, His, BB, and PF), NIR signal penetration is expected to be sufficient for the visualization of all CCS components. Reassuringly, both human CNTN2[152] and NPTN (this current study) are known to be expressed specifically within the human CCS, providing viable targets for translational opportunities.

Finally, it is known that CCS components within the human heart are large (e.g. SAN: 29.5 mm x 1.8 mm x 6.4 mm) but only contain a limited and heterogenous number of conduction cells posing a potential issue in adequate signal detection[153]. To this end, not one but two optical imaging agents (Nptn-800 and Cntn2-800) were generated, the combination of which may provide additional signal amplification in the clinical setting.

1.10.7. Future steps towards clinical translation

This study represents, to my knowledge, the first evidence of real-time *in vivo* antibody-labeling of any cardiac component. To this end, both Nptn-800 and Cntn2-800 have been used to visually delineate all components of the CCS *in vivo*, with minimal background fluorescence from other cell types. Implicating high potential for clinical translation, these tools may help prevent intraoperative damage to the CCS and improve surgical outcomes in a clinical setting. In this regard, a patent has been filed (Patent No. 62/871,551) through Stanford Office of Technology Licensing entailing all potential genetic targets for antibody-based translational approaches to molecularly target CCS components. However, several challenges must be tackled, and various pitfalls have to be overcome on the road towards clinical translation and the improvement of patient care.

Firstly, optical imaging agents (NPTN-800 and CNTN2-800) must be manufactured according to pharmaceutical quality standards and per good manufacturing practice. In this regard, polyclonal antibodies (as used in this study) consist of various IgG molecules produced by multiple different B-cell lines. However, monoclonal antibodies derived from a single B-cell clone show much higher specificity to a given epitope and are more predictable than their polyclonal counterparts. Moreover, although several chimeric and humanized monoclonal antibodies have achieved FDA approval in the past, most antibodies that have recently achieved FDA approval are fully human in origin due to their low potential of immunogenicity. Thus, for an optimal safety profile and to maximize chances of rapid clinical translation, fully human monoclonal antibodies directed against the extracellular portion of both NPTN and CNTN2 should be generated as it is currently being pursued with industrial partners.

Additionally, preclinical validation studies addressing the ideal dosage, the timepoint of systemic delivery prior to the planned surgical procedure, and whole-body biodistribution assays have already successfully been performed in mice(Goodyer, Beyersdorf et al. 2022). Next, large animal models are needed to assess the degree of resolution and NIR signal intensity in human-sized hearts. Moreover, both safety and toxicity will be assessed in large animal models using GMP-manufactured antibodies. Once all preclinical studies necessary will have been successfully accomplished, an Investigational New Drug (IND) application will be filed to obtain permission for clinical trials in human subjects.

Summary

To allow for coordinated contraction of the human heart, all heart cells must be precisely synchronized. In this regard, the cardiac conduction system (CCS) dictates the rhythm of the heart, consisting of unique cellular components. Namely, the sinoatrial node (SAN), internodal tracts (INT), the atrioventricular node (AVN), the bundle of His (HIS), left and right bundle branches (BB) as well as the Purkinje fiber network (PF)[2].

Disruption of any of these specialized CCS components can result in a host of severe clinical manifestations such as pacemaker dysfunction, complete heart block, and other life-threatening cardiac arrhythmias such as ventricular tachycardia, ventricular fibrillation and sudden death[14,18–20]. Despite being a significant cause of worldwide morbidity and mortality, our understanding of cardiac arrhythmias remains incomplete. This is due to major obstacles in CCS research including a) small total conduction cell numbers, b) their intricate three-dimensional anatomy within the heart, c) inter- and intracomponent cell type heterogeneity, as well as d) our inability to isolate and visualize conduction cells from the surrounding working myocardium[13,22,23].

In order to tackle the above-mentioned hurdles, single-cell RNA-sequencing (scRNA-seq) of the developing murine CCS was performed in part I of this study. To this end, three zones of microdissection were harvested from wild-type CD1 mouse hearts at embryonic day 16.5 (E16.5), including the SAN with its immediately surrounding tissues (zone I), the AVN/His region (zone II) as well as the BB/PF system (zone III). A total of 22,462 cells deriving from all major components of the murine CCS were freshly harvested and further processed in a designed scRNA-seq workflow. As a result, this study provides detailed transcriptomic signatures of the entire CCS, providing the first comprehensive CCS-specific gene atlas at single cell resolution. Data validation was then performed using immunohistochemistry, high-resolution fluorescence *in situ* hybdridization (RNAscope) and immunolabeling-enabled three-dimensional imaging of solvent-cleared organs (iDISCO+), further reinforcing our transcriptomic findings. Specifically, a host of previously unknown genes were discovered to be significantly enriched within one or multiple CCS components including Copine 5 (*Cpne5*), Regulator of G-protein signaling 6 (*Rgs6*), Insulin-like growth factor-binding protein 5 (*Igfbp5*), SPARC-related modular calcium-binding protein 2 (*Smoc2*) and Neurotrimin (*Ntm*). Strikingly, these novel markers not only help to identify, characterize, and isolate core CCS components (e.g. SAN, AVN, His, PF) but also represent the first known markers for the molecular identification of previously elusive transitional cells within the CCS.

Subsequently, novel CCS-specific genetic markers were used in combination with whole-organ immunostaining, organ clearing and 3D imaging (iDISCO+) in whole hearts to elucidate the three-dimensional anatomical location of transitional cells at the periphery of the SAN (**Figure 1.16**), for the first time. Strikingly, three distinct populations of transitional cells were identified at very precise and reproducible locations surrounding the SAN. While it has previously been hypothesized, that depolarization does not leave the SAN in circular waveforms but through specialized sinoatrial node conduction pathways (SACP)[5], the findings of this current study describe, for the first time, their precise anatomical location within the heart and suggest importance of transitional cells for the initiation of rhythmic cardiac beating.

Furthermore, various attempts have been made in previous studies to unravel the complex three-dimensional anatomy of the entire CCS within the heart[13,88]. However, CCS components have never successfully been shown three-dimensionally in whole hearts before. In this study, a handful of novel genetic markers were discovered, one of which (*Cpne5*) was found to be highly enriched within all components of the CCS. Therefore, immunolabeling of the entire murine CCS was performed and subsequent whole-organ clearing and lightsheet imaging has provided the first 3D model of the entire CCS in intact hearts (**Figure 1.17**).

Part II of this study successfully translates these new molecular discoveries for clinical use, generating and validating novel optical imaging tools for the real-time intraoperative visualization of conduction tissues. In this regard, bioinformatic data analyses were performed of the large scRNA-seq dataset (described in Part I), uncovering a host of novel cell surface markers highly enriched within the entire CCS or individual CCS components (**Table 2.1**).

Specifically, Neuroplastin (Nptn) was discovered as a novel cell surface marker significantly enriched within all key components of the CCS. For further validation of this novel marker, immunohistochemistry was performed in both murine and human conduction tissues, demonstrating highly specific Nptn enrichment within the entire CCS across species borders (**Figure 2.3-2.5**). Subsequently, novel optical imaging tools were generated (called "Nptn-800" and "Cntn2-800", respectively) to target the cardiac conduction system *in vivo.* In this regard, near-infrared (800 nm) dyes were covalently conjugated to IgG-antibodies directed against Nptn as well as the previously known cell surface marker Contactin-2 (Cntn2)[75]. Next, wild-type, CD1 mice received a single intravenous injection of either Nptn-800 or Cntn2-800 to label the CCS *in vivo*. Further, mice were sacrificed, hearts were harvested and strikingly, highly sensitive and specific labeling of the entire CCS was detected after intravenous injection (**Figure 2.6-2.8, 2.10**). Additional preclinical validation of novel diagnostic tools was performed, using intraoperatively established imaging systems (SPY Elite), demonstrating the *in vivo* visualization of conduction tissues at submillimeter resolution (**Figure 2.10**). Due to promising results both *ex vivo* and *in vivo*, a patent was filed through Stanford Office of Technology Licensing (Patent No. 62/871,551) and novel optical imaging tools for human use are currently being generated with industrial partners.

Appendices

List of Publications

04/2024 **Beyersdorf, Benjamin**, Stefanos Voglis, Guoming Zhao, Johannes Sarnthein, Luca Regli, and Menno R. Germans. (2024). Treatment Outcomes and the Role of the DES Scheme in the Appropriate Treatment Selection for High-Grade Dural Arteriovenous Fistulas. *Neurosurgical Focus* 56 (3): E11.

11/2023 Voglis, S., Padevit, L., van Niftrik, C. H. B., Kälin, V., **Beyersdorf, B.**, Da Mutten, R., Stumpo, V., Bellomo, J., Sarnthein, J., Staartjes, V. E., Carretta, A., Krayenbühl, N., Regli, L., & Serra, C. (2023). Safety of microneurosurgical interventions for superficial and deep-seated brain metastases: Single-center cohort study of 637 consecutive cases. *Journal of Neuro-Oncology*. 165 (2): 271–78.

10/2022 Goodyer, W. R., **Beyersdorf, B. M.**, Duan, L., van den Berg, N. S., Mantri, S., Galdos, F. X., Puluca, N., Buikema, J. W., Lee, S., Salmi, D., Robinson, E. R., Rogalla, S., Cogan, D. P., Khosla, C., Rosenthal, E. L., & Wu, S. M. (2022). In vivo visualization and molecular targeting of the cardiac conduction system. *Journal of Clinical Investigation*, 132(20).

06/2022 Vorperian, S. K., Moufarrej, M. N., (...), **Beyersdorf, B. M.**, (...), Quake, S. R. (2022). Cell types of origin of the cell-free transcriptome. *Nature Biotechnology*, 40(6), 855–861.

05/2022 Jones, R. C., Karkanias, J., Krasnow, M. A., Pisco, A. O., Quake, S. R., Salzman, J., Yosef, N., Bulthaup, B., Brown, P., Harper, W., Hemenez, M., Ponnusamy, R., Salehi, A., Sanagavarapu, B. A., Spallino, E., Aaron, K. A., Concepcion, W., Gardner, J. M., (...), **Beyersdorf, B. M.**, (...), Wyss-Coray, T. (2022). The Tabula Sapiens: A multiple-organ, single-cell transcriptomic atlas of humans. *Science* (New York, N.Y.), 376(6594), eabl4896.

09/2021 Olivieri, J. E., Dehghannasiri, R., Wang, P. L., Jang, S., de Morree, A., Tan, S. Y., Ming, J., Ruohao Wu, A., (...), **Beyersdorf, B. M.**, (...), Quake, S. R., Krasnow, M. A., & Salzman, J. (2021). RNA splicing programs define tissue compartments and cell types at single-cell resolution. *eLife*, 10, e70692.

03/2021 Rybak-Wolf, Agnieszka, Emanuel Wyler, Ivano Legnini, Anna Loewa, Petar Glažar, Seung Joon Kim, Tancredi Massimo Pentimalli, Anna Oliveras Martinez, **Benjamin Beyersdorf**, Andrew Woehler, Markus Landthaler, and Nikolaus Rajewsky. (2021). Neurodegeneration in Human Brain Organoids Infected with Herpes Simplex Virus Type 1. 2021. *biorxiv,* 03.05.434122.

07/2020 Buikema, J. W., Lee, S., Goodyer, W. R., Maas, R. G., Chirikian, O., Li, G., Miao, Y., Paige, S. L., Lee, D., Wu, H., Paik, D. T., Rhee, S., Tian, L., Galdos, F. X., Puluca, N., **Beyersdorf, B.**, Hu, J., Beck, A., Venkamatran, S., ... Wu, S. M. (2020). Wnt Activation and Reduced Cell-Cell Contact Synergistically Induce Massive Expansion of Functional Human iPSC-Derived Cardiomyocytes. *Cell Stem Cell*, 27(1), 50-63.e5.

08/2019 Goodyer, W. R., **Beyersdorf, B. M.**, Paik, D. T., Tian, L., Li, G., Buikema, J. W., Chirikian, O., Choi, S., Venkatraman, S., Adams, E. L., Tessier-Lavigne, M., Wu, J. C., & Wu, S. M. (2019). Transcriptomic Profiling of the Developing Cardiac Conduction System at Single-Cell Resolution. *Circulation Research*, 125(4), 379– 397.

Patent

07/2020 **United States Patent**, Stanford, USA. *Title:* Novel molecular tools to visualize and target the cardiac conduction system. *Inventors:* Sean M. Wu, William R. Goodyer, **Benjamin M. Beyersdorf**, Nynke Van Den Berg, Eben Rosenthal. United States Patent No: 62/871,551

Authorization for reproduction of published material

For all figures incorporated into this dissertation that were previously published, formal authorization for reproduction was obtained as delineated below:

1. **Journal**: Circulation Research; **Title**: Transcriptomic Profiling of the Developing Cardiac Conduction System at Single-Cell Resolution; **License Number**: 5424750450378.
2. **Journal**: Circulation Research; **Title**: Developmental Origin, Growth, and Three-Dimensional Architecture of the Atrioventricular Conduction Axis of the Mouse Heart; **License Number**: 5424180426370.
3. **Journal**: American Journal of Physiology-Heart and Circulatory Physiology; **Title**: Conduction Barriers and Pathways of the Sinoatrial Pacemaker Complex: Their Role in Normal Rhythm and Atrial Arrhythmias; **License Number**: 5450120822889.
4. **Journal**: Clinical Cancer Research; **Title**: Safety and Tumor Specificity of Cetuximab-IRDye800 for Surgical Navigation in Head and Neck Cancer; **License Number**: 5424171319685.
5. **Journal**: The Journal of Clinical Investigation; **Title**: In Vivo Visualization and Molecular Targeting of the Cardiac Conduction System; **License Number**: 1300986-1.

References

1. Bergmann O, Zdunek S, Felker A, et al. Dynamics of Cell Generation and Turnover in the Human Heart. *Cell*. 2015;161(7):1566-1575. doi:10.1016/j.cell.2015.05.026
2. Christoffels VM, Smits GJ, Kispert A, Moorman AFM. Development of the Pacemaker Tissues of the Heart. *Circ Res*. 2010;106(2):240-254. doi:10.1161/CIRCRESAHA.109.205419
3. Goodyer WR, Beyersdorf BM, Paik DT, et al. Transcriptomic Profiling of the Developing Cardiac Conduction System at Single-Cell Resolution. *Circ Res*. 2019;125(4):379-397. doi:10.1161/CIRCRESAHA.118.314578
4. Keith A, Flack M. The Form and Nature of the Muscular Connections between the Primary Divisions of the Vertebrate Heart. *J Anat Physiol*. 1907;41(Pt 3):172-189.
5. Csepe TA, Zhao J, Hansen BJ, et al. Human sinoatrial node structure: 3D microanatomy of sinoatrial conduction pathways. *Prog Biophys Mol Biol*. 2016;120(1-3):164-178. doi:10.1016/j.pbiomolbio.2015.12.011
6. Liang X, Evans SM, Sun Y. Development of the cardiac pacemaker. *Cell Mol Life Sci CMLS*. 2017;74(7):1247-1259. doi:10.1007/s00018-016-2400-1

7. Wiese C, Grieskamp T, Airik R, et al. Formation of the Sinus Node Head and Differentiation of Sinus Node Myocardium Are Independently Regulated by Tbx18 and Tbx3. *Circ Res*. 2009;104(3):388-397. doi:10.1161/CIRCRESAHA.108.187062
8. Ferrer M. Irené. The Sick Sinus Syndrome. *Circulation*. 1973;47(3):635-641. doi:10.1161/01.CIR.47.3.635
9. Tawara S. *Das Reizleitungssystem des Säugetierherzens*. Fischer; 1906.
10. Aschoff L. Aschoff L. 1910. Referat über die Herzstorungen in ihren Beziehungen zu den Spezifischen Muskelsystem des Herzens. Verh Dtsch Pathol Ges 14: 3–35.
11. Meijler FL, Janse MJ. Morphology and electrophysiology of the mammalian atrioventricular node. *Physiol Rev*. 1988;68(2):608-647. doi:10.1152/physrev.1988.68.2.608
12. Sherf L, James TN, Woods WT. Function of the atrioventricular node considered on the basis of observed histology and fine structure. *J Am Coll Cardiol*. 1985;5(3):770-780. doi:10.1016/s0735-1097(85)80411-3
13. Aanhaanen WTJ, Mommersteeg MTM, Norden J, et al. Developmental Origin, Growth, and Three-Dimensional Architecture of the Atrioventricular Conduction Axis of the Mouse Heart. *Circ Res*. 2010;107(6):728-736. doi:10.1161/CIRCRESAHA.110.222992
14. Karyofillis P, Kostopoulou A, Thomopoulou S, et al. Conduction abnormalities after transcatheter aortic valve implantation. *J Geriatr Cardiol JGC*. 2018;15(1):105-112. doi:10.11909/j.issn.1671-5411.2018.01.004
15. Tranum-Jensen J, Wilde AA, Vermeulen JT, Janse MJ. Morphology of electrophysiologically identified junctions between Purkinje fibers and ventricular muscle in rabbit and pig hearts. *Circ Res*. 1991;69(2):429-437. doi:10.1161/01.RES.69.2.429
16. Haïssaguerre M, Shah DC, Jaïs P, et al. Role of Purkinje conducting system in triggering of idiopathic ventricular fibrillation. *Lancet Lond Engl*. 2002;359(9307):677-678. doi:10.1016/S0140-6736(02)07807-8
17. Nogami A, Sugiyasu A, Kubota S, Kato K. Mapping and ablation of idiopathic ventricular fibrillation from the Purkinje system. *Heart Rhythm*. 2005;2(6):646-649. doi:10.1016/j.hrthm.2005.02.006
18. Hudson RE. Surgical pathology of the conducting system of the heart. *Heart*. 1967;29(5):646-670. doi:10.1136/hrt.29.5.646
19. Peretto G, Durante A, Limite LR, Cianflone D. Postoperative Arrhythmias after Cardiac Surgery: Incidence, Risk Factors, and Therapeutic Management. *Cardiol Res Pract*. 2014;2014. doi:10.1155/2014/615987
20. Smits JPP, Veldkamp MW, Wilde AAM. Mechanisms of inherited cardiac conduction disease. *EP Eur*. 2005;7(2):122-137. doi:10.1016/j.eupc.2004.11.004
21. Khurshid S, Choi SH, Weng LC, et al. Frequency of Cardiac Rhythm Abnormalities in a Half Million Adults. *Circ Arrhythm Electrophysiol*. 2018;11(7):e006273. doi:10.1161/CIRCEP.118.006273
22. van Eif VWW, Stefanovic S, van Duijvenboden K, et al. Transcriptome analysis of mouse and human sinoatrial node cells reveals a conserved genetic program. *Development*. 2019;146(8):dev173161. doi:10.1242/dev.173161
23. Vedantham V, Galang G, Evangelista M, Deo RC, Srivastava D. RNA Sequencing of Mouse Sinoatrial Node Reveals an Upstream Regulatory Role for Islet-1 in Cardiac Pacemaker Cells. *Circ Res*. 2015;116(5):797-803. doi:10.1161/CIRCRESAHA.116.305913
24. Hulsmans M, Clauss S, Xiao L, et al. Macrophages Facilitate Electrical Conduction in the Heart. *Cell*. 2017;169(3):510-522.e20. doi:10.1016/j.cell.2017.03.050
25. Kanemaru K, Cranley J, Muraro D, et al. Spatially resolved multiomics of human cardiac niches. *Nature*. 2023;619(7971):801-810. doi:10.1038/s41586-023-06311-1
26. Masson-Pévet MA, Bleeker WK, Besselsen E, Treytel BW, Jongsma HJ, Bouman LN. Pacemaker cell types in the rabbit sinus node: a correlative ultrastructural and electrophysiological study. *J Mol Cell Cardiol*. 1984;16(1):53-63.

27. Oosthoek PW, Virágh S, Mayen AE, van Kempen MJ, Lamers WH, Moorman AF. Immunohistochemical delineation of the conduction system. I: The sinoatrial node. *Circ Res*. 1993;73(3):473-481. doi:10.1161/01.RES.73.3.473
28. Chandler NJ, Greener ID, Tellez JO, et al. Molecular Architecture of the Human Sinus Node: Insights Into the Function of the Cardiac Pacemaker. *Circulation*. 2009;119(12):1562-1575. doi:10.1161/CIRCULATIONAHA.108.804369
29. Haissaguerre M, Vigmond E, Stuyvers B, Hocini M, Bernus O. Ventricular arrhythmias and the His–Purkinje system. *Nat Rev Cardiol*. 2016;13(3):155-166. doi:10.1038/nrcardio.2015.193
30. Kharche SR, Vigmond E, Efimov IR, Dobrzynski H. Computational assessment of the functional role of sinoatrial node exit pathways in the human heart. Panfilov AV, ed. *PLOS ONE*. 2017;12(9):e0183727. doi:10.1371/journal.pone.0183727
31. Anderson RH, Durrer D, Janse MJ, et al. A Combined Morphological and Electrophysiological Study of the Atrioventricular Node of the Rabbit Heart. *Circ Res*. 1974;35(6):909-922. doi:10.1161/01.RES.35.6.909
32. Martinez-Palomo A, Alanis J, Benitez D. TRANSITIONAL CARDIAC CELLS OF THE CONDUCTIVE SYSTEM OF THE DOG HEART. *J Cell Biol*. 1970;47(1):1-17.
33. Kamiyama A, Inoue F. Conduction Delay from Purkinje Fiber to Ventricular Muscle Studied with Extracellular Microelectrodes. *Can J Physiol Pharmacol*. 1971;49(7):678-684. doi:10.1139/y71-091
34. Weidmann S. The effect of the cardiac membrane potential on the rapid availability of the sodium-carrying system. *J Physiol*. 1955;127(1):213-224. doi:10.1113/jphysiol.1955.sp005250
35. James T N, Isobe J H, Urthaler F. Correlative electrophysiological and anatomical studies concerning the site of origin of escape rhythm during complete atrioventricular block in the dog. *Circ Res*. 1979;45(1):108-119. doi:10.1161/01.RES.45.1.108
36. DiFrancesco D, Ferroni A, Mazzanti M, Tromba C. Properties of the hyperpolarizing-activated current (if) in cells isolated from the rabbit sino-atrial node. *J Physiol*. 1986;377(1):61-88. doi:10.1113/jphysiol.1986.sp016177
37. Blaschke RJ, Hahurij ND, Kuijper S, et al. Targeted Mutation Reveals Essential Functions of the Homeodomain Transcription Factor *Shox2* in Sinoatrial and Pacemaking Development. *Circulation*. 2007;115(14):1830-1838. doi:10.1161/CIRCULATIONAHA.106.637819
38. Garcia-Frigola C, Shi Y, Evans SM. Expression of the hyperpolarization-activated cyclic nucleotide-gated cation channel HCN4 during mouse heart development. *Gene Expr Patterns GEP*. 2003;3(6):777-783.
39. Liang X, Zhang Q, Cattaneo P, et al. Transcription factor ISL1 is essential for pacemaker development and function. *J Clin Invest*. 2015;125(8):3256-3268. doi:10.1172/JCI68257
40. Marionneau C, Couette B, Liu J, et al. Specific pattern of ionic channel gene expression associated with pacemaker activity in the mouse heart. *J Physiol*. 2005;562(Pt 1):223-234. doi:10.1113/jphysiol.2004.074047
41. Moskowitz IPG, Pizard A, Patel VV, et al. The T-Box transcription factor Tbx5 is required for the patterning and maturation of the murine cardiac conduction system. *Development*. 2004;131(16):4107-4116. doi:10.1242/dev.01265
42. Tellez JO, Dobrzynski H, Greener ID, et al. Differential Expression of Ion Channel Transcripts in Atrial Muscle and Sinoatrial Node in Rabbit. *Circ Res*. 2006;99(12):1384-1393. doi:10.1161/01.RES.0000251717.98379.69
43. Christoffels VM, Hoogaars WMH, Tessari A, Clout DEW, Moorman AFM, Campione M. T-box transcription factor Tbx2 represses differentiation and formation of the cardiac chambers. *Dev Dyn*. 2004;229(4):763-770. doi:10.1002/dvdy.10487

44. Greener ID, Tellez JO, Dobrzynski H, et al. Ion Channel Transcript Expression at the Rabbit Atrioventricular Conduction Axis. *Circ Arrhythm Electrophysiol*. 2009;2(3):305-315. doi:10.1161/CIRCEP.108.803569
45. Harrelson Z, Kelly RG, Goldin SN, et al. Tbx2 is essential for patterning the atrioventricular canal and for morphogenesis of the outflow tract during heart development. *Development*. 2004;131(20):5041-5052. doi:10.1242/dev.01378
46. Munshi NV, McAnally J, Bezprozvannaya S, et al. Cx30.2 enhancer analysis identifies Gata4 as a novel regulator of atrioventricular delay. *Development*. 2009;136(15):2665-2674. doi:10.1242/dev.038562
47. Remme CA, Verkerk AO, Hoogaars WMH, et al. The cardiac sodium channel displays differential distribution in the conduction system and transmural heterogeneity in the murine ventricular myocardium. *Basic Res Cardiol*. 2009;104(5):511-522. doi:10.1007/s00395-009-0012-8
48. Han W, Bao W, Wang Z, Nattel S. Comparison of Ion-Channel Subunit Expression in Canine Cardiac Purkinje Fibers and Ventricular Muscle. *Circ Res*. 2002;91(9):790-797. doi:10.1161/01.RES.0000039534.18114.D9
49. Kanter HL, Laing JG, Beau SL, Beyer EC, Saffitz JE. Distinct patterns of connexin expression in canine Purkinje fibers and ventricular muscle. *Circ Res*. 1993;72(5):1124-1131. doi:10.1161/01.RES.72.5.1124
50. Tseng GN, Boyden PA. Multiple types of Ca2+ currents in single canine Purkinje cells. *Circ Res*. 1989;65(6):1735-1750. doi:10.1161/01.RES.65.6.1735
51. Tang F, Barbacioru C, Wang Y, et al. mRNA-Seq whole-transcriptome analysis of a single cell. *Nat Methods*. 2009;6(5):377-382. doi:10.1038/nmeth.1315
52. Miranda AMA, Janbandhu V, Maatz H, et al. Single-cell transcriptomics for the assessment of cardiac disease. *Nat Rev Cardiol*. 2023;20(5):289-308. doi:10.1038/s41569-022-00805-7
53. Mazutis L, Gilbert J, Ung WL, Weitz DA, Griffiths AD, Heyman JA. Single-cell analysis and sorting using droplet-based microfluidics. *Nat Protoc*. 2013;8(5):870-891. doi:10.1038/nprot.2013.046
54. Potter SS. Single-cell RNA sequencing for the study of development, physiology and disease. *Nat Rev Nephrol*. 2018;14(8):479. doi:10.1038/s41581-018-0021-7
55. Cunningham JP, Ghahramani Z. Linear Dimensionality Reduction: Survey, Insights, and Generalizations. :42.
56. Maaten L van der, Hinton G. Visualizing Data using t-SNE. *J Mach Learn Res*. 2008;9(Nov):2579-2605.
57. Butler A, Hoffman P, Smibert P, Papalexi E, Satija R. Integrating single-cell transcriptomic data across different conditions, technologies, and species. *Nat Biotechnol*. 2018;36(5):411-420. doi:10.1038/nbt.4096
58. Hoogaars W. The transcriptional repressor Tbx3 delineates the developing central conduction system of the heart. *Cardiovasc Res*. 2004;62(3):489-499. doi:10.1016/j.cardiores.2004.01.030
59. Severs NJ. Cardiac muscle cell interaction: from microanatomy to the molecular make-up of the gap junction. *Histol Histopathol*. 1995;10(2):481-501.
60. Sánchez-Quintana D, Cabrera JA, Farré J, Climent V, Anderson RH, Ho SY. Sinus node revisited in the era of electroanatomical mapping and catheter ablation. *Heart*. 2005;91(2):189-194. doi:10.1136/hrt.2003.031542
61. Vedantham V. New Approaches to Biological Pacemakers: Links to Sinoatrial Node Development. *Trends Mol Med*. 2015;21(12):749-761. doi:10.1016/j.molmed.2015.10.002
62. Davenport TG, Jerome-Majewska LA, Papaioannou VE. Mammary gland, limb and yolk sac defects in mice lacking Tbx3, the gene mutated in human ulnar mammary syndrome. *Dev Camb Engl*. 2003;130(10):2263-2273. doi:10.1242/dev.00431

63. Eriksson KS, Mignot E. The homeobox gene T-box 3 is expressed in the adult mouse hypothalamus and medulla. *Brain Res*. 2009;1302:233-239. doi:10.1016/j.brainres.2009.08.101
64. Gibson-Brown JJ, Agulnik SI, Chapman DL, et al. Evidence of a role for T-box genes in the evolution of limb morphogenesis and the specification of forelimb/hindlimb identity. *Mech Dev*. 1996;56(1-2):93-101.
65. Suzuki A, Sekiya S, Büscher D, Belmonte JCI, Taniguchi H. Tbx3 controls the fate of hepatic progenitor cells in liver development by suppressing p19ARF expression. *Development*. 2008;135(9):1589-1595. doi:10.1242/dev.016634
66. Yang J, Huang J, Maity B, et al. RGS6, a Modulator of Parasympathetic Activation in Heart. *Circ Res*. 2010;107(11):1345-1349. doi:10.1161/CIRCRESAHA.110.224220
67. Wydeven N, Posokhova E, Xia Z, Martemyanov KA, Wickman K. RGS6, but not RGS4, is the dominant regulator of G protein signaling (RGS) modulator of the parasympathetic regulation of mouse heart rate. *J Biol Chem*. 2014;289(4):2440-2449. doi:10.1074/jbc.M113.520742
68. Kerr KF, Avery CL, Lin HJ, et al. Genome-wide association study of heart rate and its variability in Hispanic/Latino cohorts. *Heart Rhythm*. 2017;14(11):1675-1684. doi:10.1016/j.hrthm.2017.06.018
69. Nolte IM, Munoz ML, Tragante V, et al. Genetic loci associated with heart rate variability and their effects on cardiac disease risk. *Nat Commun*. 2017;8. doi:10.1038/ncomms15805
70. Posokhova E, Wydeven N, Allen KL, Wickman K, Martemyanov KA. RGS6/Gβ5 complex accelerates IKACh gating kinetics in atrial myocytes and modulates parasympathetic regulation of heart rate. *Circ Res*. 2010;107(11):1350-1354. doi:10.1161/CIRCRESAHA.110.224212
71. Rorabaugh BR, Chakravarti B, Mabe NW, et al. Regulator of G Protein Signaling 6 Protects the Heart from Ischemic Injury. *J Pharmacol Exp Ther*. 2017;360(3):409-416. doi:10.1124/jpet.116.238345
72. Creutz CE, Tomsig JL, Snyder SL, et al. The copines, a novel class of C2 domain-containing, calcium-dependent, phospholipid-binding proteins conserved from Paramecium to humans. *J Biol Chem*. 1998;273(3):1393-1402.
73. den Hoed M, Eijgelsheim M, Esko T, et al. Identification of heart rate-associated loci and their effects on cardiac conduction and rhythm disorders. *Nat Genet*. 2013;45(6):621-631. doi:10.1038/ng.2610
74. Struyk AF, Canoll PD, Wolfgang MJ, Rosen CL, D'Eustachio P, Salzer JL. Cloning of neurotrimin defines a new subfamily of differentially expressed neural cell adhesion molecules. *J Neurosci*. 1995;15(3):2141-2156. doi:10.1523/JNEUROSCI.15-03-02141.1995
75. Pallante BA, Giovannone S, Fang-Yu L, et al. Contactin-2 Expression in the Cardiac Purkinje Fiber Network. *Circ Arrhythm Electrophysiol*. 2010;3(2):186-194. doi:10.1161/CIRCEP.109.928820
76. Peeters T, Monteagudo S, Tylzanowski P, Luyten FP, Lories R, Cailotto F. SMOC2 inhibits calcification of osteoprogenitor and endothelial cells. *PLoS ONE*. 2018;13(6). doi:10.1371/journal.pone.0198104
77. Rocnik EF, Liu P, Sato K, Walsh K, Vaziri C. The novel SPARC family member SMOC-2 potentiates angiogenic growth factor activity. *J Biol Chem*. 2006;281(32):22855-22864. doi:10.1074/jbc.M513463200
78. Vannahme C, Gösling S, Paulsson M, Maurer P, Hartmann U. Characterization of SMOC-2, a modular extracellular calcium-binding protein. *Biochem J*. 2003;373(Pt 3):805-814. doi:10.1042/BJ20030532
79. James PL, Stewart CE, Rotwein P. Insulin-like growth factor binding protein-5 modulates muscle differentiation through an insulin-like growth factor-dependent mechanism.

J Cell Biol. 1996;133(3):683-693. doi:10.1083/jcb.133.3.683
80. Pera EM, Wessely O, Li SY, De Robertis EM. Neural and head induction by insulin-like growth factor signals. *Dev Cell*. 2001;1(5):655-665. doi:10.1016/s1534-5807(01)00069-7
81. Wang J, Ding N, Li Y, et al. Insulin-like growth factor binding protein 5 (IGFBP5) functions as a tumor suppressor in human melanoma cells. *Oncotarget*. 2015;6(24):20636-20649.
82. Sureshbabu A, Okajima H, Yamanaka D, et al. IGFBP5 induces cell adhesion, increases cell survival and inhibits cell migration in MCF-7 human breast cancer cells. *J Cell Sci*. 2012;125(7):1693-1705. doi:10.1242/jcs.092882
83. Ock S, Choi SW, Choi SH, et al. Insulin signaling is critical for sinoatrial node maintenance and function. *Exp Mol Med*. 2023;55(5):965-973. doi:10.1038/s12276-023-00988-0
84. Fedorov VV, Schuessler RB, Hemphill M, et al. Structural and functional evidence for discrete exit pathways that connect the canine sinoatrial node and atria. *Circ Res*. 2009;104(7):915-923. doi:10.1161/CIRCRESAHA.108.193193
85. Fedorov VV, Glukhov AV, Chang R. Conduction barriers and pathways of the sinoatrial pacemaker complex: their role in normal rhythm and atrial arrhythmias. *Am J Physiol-Heart Circ Physiol*. 2012;302(9):H1773-H1783. doi:10.1152/ajpheart.00892.2011
86. Kalyanasundaram A, Li N, Augostini RS, Weiss R, Hummel JD, Fedorov VV. Three-dimensional functional anatomy of the human sinoatrial node for epicardial and endocardial mapping and ablation. *Heart Rhythm*. 2023;20(1):122-133. doi:10.1016/j.hrthm.2022.08.039
87. James TN. The connecting pathways between the sinus node and A-V node and between the right and the left atrium in the human heart. *Am Heart J*. 1963;66(4):498-508. doi:10.1016/0002-8703(63)90382-X
88. Dobrzynski H, Li J, Tellez J, et al. Computer Three-Dimensional Reconstruction of the Sinoatrial Node. *Circulation*. 2005;111(7):846-854. doi:10.1161/01.CIR.0000152100.04087.DB
89. Larsson B, Elmqvist H, Rydén L, Schüller H. Lessons from the first patient with an implanted pacemaker: 1958-2001. *Pacing Clin Electrophysiol PACE*. 2003;26(1 Pt 1):114-124.
90. Greenspon AJ, Patel JD, Lau E, et al. Trends in Permanent Pacemaker Implantation in the United States From 1993 to 2009: Increasing Complexity of Patients and Procedures. *J Am Coll Cardiol*. 2012;60(16):1540-1545. doi:10.1016/j.jacc.2012.07.017
91. Lamas GA, Lee KL, Sweeney MO, et al. Ventricular Pacing or Dual-Chamber Pacing for Sinus-Node Dysfunction. http://dx.doi.org.stanford.idm.oclc.org/10.1056/NEJMoa013040. doi:10.1056/NEJMoa013040
92. Aggarwal RK, Connelly DT, Ray SG, Ball J, Charles RG. Early complications of permanent pacemaker implantation: no difference between dual and single chamber systems. *Heart*. 1995;73(6):571-575. doi:10.1136/hrt.73.6.571
93. Harcombe A, Newell S, Ludman P, et al. Late complications following permanent pacemaker implantation or elective unit replacement. *Heart*. 1998;80(3):240-244.
94. Zwi L, Caspi O, Arbel G, et al. Cardiomyocyte differentiation of human induced pluripotent stem cells. *Circulation*. 2009;120(15):1513-1523. doi:10.1161/CIRCULATIONAHA.109.868885
95. Itskovitz-Eldor J, Schuldiner M, Karsenti D, et al. Differentiation of human embryonic stem cells into embryoid bodies compromising the three embryonic germ layers. *Mol Med Camb Mass*. 2000;6(2):88-95.
96. Laflamme MA, Chen KY, Naumova AV, et al. Cardiomyocytes derived from human embryonic stem cells in pro-survival factors enhance function of infarcted rat hearts. *Nat Biotechnol*. 2007;25(9):1015-1024. doi:10.1038/nbt1327
97. Du R, Bai S, Zhao Y, Ma Y. Efficient generation of TBX3+ atrioventricular conduction-like cardiomyocytes from human pluripotent stem cells. *Biochem Biophys Res Commun*.

2023;669:143-149. doi:10.1016/j.bbrc.2023.05.104
98. Schweizer PA, Darche FF, Ullrich ND, et al. Subtype-specific differentiation of cardiac pacemaker cell clusters from human induced pluripotent stem cells. *Stem Cell Res Ther*. 2017;8. doi:10.1186/s13287-017-0681-4
99. Kehat I, Khimovich L, Caspi O, et al. Electromechanical integration of cardiomyocytes derived from human embryonic stem cells. *Nat Biotechnol*. 2004;22(10):1282-1289. doi:10.1038/nbt1014
100. Plotnikov Alexei N., Sosunov Eugene A., Qu Jihong, et al. Biological Pacemaker Implanted in Canine Left Bundle Branch Provides Ventricular Escape Rhythms That Have Physiologically Acceptable Rates. *Circulation*. 2004;109(4):506-512. doi:10.1161/01.CIR.0000114527.10764.CC
101. Cho Hee Cheol, Kashiwakura Yuji, Marbán Eduardo. Creation of a Biological Pacemaker by Cell Fusion. *Circ Res*. 2007;100(8):1112-1115. doi:10.1161/01.RES.0000265845.04439.78
102. Anderson RH, Ho SY, Becker AE. The surgical anatomy of the conduction tissues. *Thorax*. 1983;38(6):408-420. doi:10.1136/thx.38.6.408
103. Lev M, Weinberg MH. Surgical Injury to the Conduction System in Ventricular Septal Defect. *Am J Cardiol*.:13.
104. Titus JL, Daugherty GW, Kirklin JW, Edwards JE. Lesions of the Atrioventricular Conduction System after Repair of Ventricular Septal Defect: Relation to Heart Block. *Circulation*. 1963;28(1):82-88. doi:10.1161/01.CIR.28.1.82
105. Hoffman JIE, Kaplan S. The incidence of congenital heart disease. *J Am Coll Cardiol*. 2002;39(12):1890-1900. doi:10.1016/s0735-1097(02)01886-7
106. Gross GJ, Chiu CC, Hamilton RM, Kirsh JA, Stephenson EA. Natural history of postoperative heart block in congenital heart disease: implications for pacing intervention. *Heart Rhythm*. 2006;3(5):601-604. doi:10.1016/j.hrthm.2006.01.023
107. Bonatti V, Agnetti A, Squarcia U. Early and late postoperative complete heart block in pediatric patients submitted to open-heart surgery for congenital heart disease. *Pediatr Medica E Chir Med Surg Pediatr*. 1998;20(3):181-186.
108. Walsh. Interventional Electrophysiology in Patients With Congenital Heart Disease.
109. Anderson RH, Ho SY. The disposition of the conduction tissues in congenitally malformed hearts with reference to their embryological development. *J Perinat Med*. 1991;19 Suppl 1:201-206.
110. Lev M, Licata RH, May RC. THE CONDUCTION SYSTEM IN MIXED LEVOCARDIA WITH VENTRICULAR INVERSION (CORRECTED TRANSPOSITION). *Circulation*. 1963;28:232-237. doi:10.1161/01.cir.28.2.232
111. Anderson RH, Becker AE, Arnold R, Wilkinson JL. The conducting tissues in congenitally corrected transposition. *Circulation*. 1974;50(5):911-923. doi:10.1161/01.cir.50.5.911
112. Cecchin F, Johnsrude CL, Perry JC, Friedman RA. Effect of age and surgical technique on symptomatic arrhythmias after the Fontan procedure. *Am J Cardiol*. 1995;76(5):386-391. doi:10.1016/s0002-9149(99)80106-4
113. Flinn CJ, Wolff GS, Dick M, et al. Cardiac rhythm after the Mustard operation for complete transposition of the great arteries. *N Engl J Med*. 1984;310(25):1635-1638. doi:10.1056/NEJM198406213102504
114. Socie P, Nicot F, Baudinaud P, et al. Frequency of Recovery from Complete Atrioventricular Block After Cardiac Surgery. *Am J Cardiol*. 2017;120(10):1841-1846. doi:10.1016/j.amjcard.2017.07.090
115. Berdajs D, Schurr UP, Wagner A, Seifert B, Turina MI, Genoni M. Incidence and pathophysiology of atrioventricular block following mitral valve replacement and ring annuloplasty. *Eur J Cardio-Thorac Surg Off J Eur Assoc Cardio-Thorac Surg*. 2008;34(1):55-

61. doi:10.1016/j.ejcts.2008.03.051
116. Liberman L, Silver ES, Chai PJ, Anderson BR. Incidence and characteristics of heart block after heart surgery in pediatric patients: A multicenter study. *J Thorac Cardiovasc Surg*. 2016;152(1):197-202. doi:10.1016/j.jtcvs.2016.03.081
117. Gordon RS, Ivanov J, Cohen G, Ralph-Edwards AL. Permanent cardiac pacing after a cardiac operation: Predicting the use of permanent pacemakers. *Ann Thorac Surg*. 1998;66(5):1698-1704. doi:10.1016/S0003-4975(98)00889-3
118. Frangioni JV. In vivo near-infrared fluorescence imaging. *Curr Opin Chem Biol*. 2003;7(5):626-634. doi:10.1016/j.cbpa.2003.08.007
119. Goodyer WR, Beyersdorf BM, Duan L, et al. In vivo visualization and molecular targeting of the cardiac conduction system. *J Clin Invest*. 2022;132(20):e156955. doi:10.1172/JCI156955
120. Rosenthal EL, Warram JM, de Boer E, et al. Safety and Tumor Specificity of Cetuximab-IRDye800 for Surgical Navigation in Head and Neck Cancer. *Clin Cancer Res Off J Am Assoc Cancer Res*. 2015;21(16):3658-3666. doi:10.1158/1078-0432.CCR-14-3284
121. Gao RW, Teraphongphom N, de Boer E, et al. Safety of panitumumab-IRDye800CW and cetuximab-IRDye800CW for fluorescence-guided surgical navigation in head and neck cancers. *Theranostics*. 2018;8(9):2488-2495. doi:10.7150/thno.24487
122. Scheltinga AGTT van, Dam GM van, Nagengast WB, et al. Intraoperative Near-Infrared Fluorescence Tumor Imaging with Vascular Endothelial Growth Factor and Human Epidermal Growth Factor Receptor 2 Targeting Antibodies. *J Nucl Med*. 2011;52(11):1778-1785. doi:10.2967/jnumed.111.092833
123. Rosenthal EL, Warram JM, de Boer E, et al. Safety and Tumor Specificity of Cetuximab-IRDye800 for Surgical Navigation in Head and Neck Cancer. *Clin Cancer Res Off J Am Assoc Cancer Res*. 2015;21(16):3658-3666. doi:10.1158/1078-0432.CCR-14-3284
124. van Dam GM, Themelis G, Crane LMA, et al. Intraoperative tumor-specific fluorescence imaging in ovarian cancer by folate receptor-α targeting: first in-human results. *Nat Med*. 2011;17(10):1315-1319. doi:10.1038/nm.2472
125. Kaushal S, McElroy MK, Luiken GA, et al. Fluorophore-conjugated anti-CEA antibody for the intraoperative imaging of pancreatic and colorectal cancer. *J Gastrointest Surg Off J Soc Surg Aliment Tract*. 2008;12(11):1938-1950. doi:10.1007/s11605-008-0581-0
126. Pleijhuis RG, Langhout GC, Helfrich W, et al. Near-infrared fluorescence (NIRF) imaging in breast-conserving surgery: Assessing intraoperative techniques in tissue-simulating breast phantoms. *Eur J Surg Oncol*. 2011;37(1):32-39. doi:10.1016/j.ejso.2010.10.006
127. Sampath L, Kwon S, Ke S, et al. Dual-labeled trastuzumab-based imaging agent for the detection of human epidermal growth factor receptor 2 overexpression in breast cancer. *J Nucl Med Off Publ Soc Nucl Med*. 2007;48(9):1501-1510. doi:10.2967/jnumed.107.042234
128. Stummer W, Pichlmeier U, Meinel T, et al. Fluorescence-guided surgery with 5-aminolevulinic acid for resection of malignant glioma: a randomised controlled multicentre phase III trial. *Lancet Oncol*. 2006;7(5):392-401. doi:10.1016/S1470-2045(06)70665-9
129. Marshall MV, Draney D, Sevick-Muraca EM, Olive DM. Single-Dose Intravenous Toxicity Study of IRDye 800CW in Sprague-Dawley Rats. *Mol Imaging Biol*. 2010;12(6):583-594. doi:10.1007/s11307-010-0317-x
130. Zinn KR, Korb M, Samuel S, et al. IND-Directed Safety and Biodistribution Study of Intravenously Injected Cetuximab-IRDye800 in Cynomolgus Macaques. *Mol Imaging Biol*. 2015;17(1):49-57. doi:10.1007/s11307-014-0773-9
131. Waas M, Snarrenberg ST, Littrell J, et al. SurfaceGenie: a web-based application for prioritizing cell-type specific marker candidates. *Bioinformatics*. doi:10.1093/bioinformatics/btaa092
132. Prince AC, Moore LS, Tipirneni KE, et al. Evaluation of optical imaging agents in a fluorescence-guided surgical model of head and neck cancer. *Surg Oncol*. 2018;27(2):225-230.

doi:10.1016/j.suronc.2018.04.004
133. Hill IE, Selkirk CP, Hawkes RB, Beesley PW. Characterization of novel glycoprotein components of synaptic membranes and postsynaptic densities, gp65 and gp55, with a monoclonal antibody. *Brain Res*. 1988;461(1):27-43. doi:10.1016/0006-8993(88)90722-6
134. Beesley PW, Herrera-Molina R, Smalla KH, Seidenbecher C. The Neuroplastin adhesion molecules: key regulators of neuronal plasticity and synaptic function. *J Neurochem*. 2014;131(3):268-283. doi:10.1111/jnc.12816
135. Owczarek S, Kiryushko D, Larsen MH, et al. Neuroplastin-55 binds to and signals through the fibroblast growth factor receptor. *FASEB J*. 2009;24(4):1139-1150. doi:10.1096/fj.09-140509
136. Herrera-Molina R, Sarto-Jackson I, Montenegro-Venegas C, et al. Structure of Excitatory Synapses and GABA $_A$ Receptor Localization at Inhibitory Synapses Are Regulated by Neuroplastin-65. *J Biol Chem*. 2014;289(13):8973-8988. doi:10.1074/jbc.M113.514992
137. Empson RM, Buckby LE, Kraus M, et al. The cell adhesion molecule neuroplastin-65 inhibits hippocampal long-term potentiation via a mitogen-activated protein kinase p38-dependent reduction in surface expression of GluR1-containing glutamate receptors. *J Neurochem*. 2006;99(3):850-860. doi:10.1111/j.1471-4159.2006.04123.x
138. Smalla KH, Matthies H, Langnäse K, et al. The synaptic glycoprotein neuroplastin is involved in long-term potentiation at hippocampal CA1 synapses. *Proc Natl Acad Sci*. 2000;97(8):4327-4332. doi:10.1073/pnas.080389297
139. Csepe TA, Kalyanasundaram A, Hansen BJ, Zhao J, Fedorov VV. Fibrosis: a structural modulator of sinoatrial node physiology and dysfunction. *Front Physiol*. 2015;6. doi:10.3389/fphys.2015.00037
140. Dick M, Norwood W I, Chipman C, Castaneda A R. Intraoperative recording of specialized atrioventricular conduction tissue electrograms in 47 patients. *Circulation*. 1979;59(1):150-160. doi:10.1161/01.CIR.59.1.150
141. Kaiser GA, Waldo AL, Beach PM, Bowman FO, Hoffman BF, Malm JR. Specialized Cardiac Conduction System: Improved Electrophysiologic Identification Technique at Surgery. *Arch Surg*. 1970;101(6):673-676. doi:10.1001/archsurg.1970.01340300029006
142. Lincoln C, Butler P, Logan-Sinclair R, Anderson RH. A cardiac conduction monitor and probe for intraoperative identification of conduction tissue. *Br Heart J*. 1979;42(3):339-344.
143. Huang Chao, Kaza Aditya K., Hitchcock Robert W., Sachse Frank B. Identification of Nodal Tissue in the Living Heart Using Rapid Scanning Fiber-Optics Confocal Microscopy and Extracellular Fluorophores. *Circ Cardiovasc Imaging*. 2013;6(5):739-746. doi:10.1161/CIRCIMAGING.112.000121
144. Huang C, Sachse FB, Hitchcock RW, Kaza AK. Sensitivity and Specificity of Cardiac Tissue Discrimination Using Fiber-Optics Confocal Microscopy. *PLoS ONE*. 2016;11(1). doi:10.1371/journal.pone.0147667
145. Huang C, Kaza AK, Hitchcock RW, Sachse FB. Local delivery of fluorescent dye for fiber-optics confocal microscopy of the living heart. *Front Physiol*. 2014;5:367. doi:10.3389/fphys.2014.00367
146. Weissleder R. A clearer vision for in vivo imaging. *Nat Biotechnol*. 2001;19(4):316-317. doi:10.1038/86684
147. Vahrmeijer AL, Hutteman M, van der Vorst JR, van de Velde CJH, Frangioni JV. Image-guided cancer surgery using near-infrared fluorescence. *Nat Rev Clin Oncol*. 2013;10(9):507-518. doi:10.1038/nrclinonc.2013.123
148. Troyan SL, Kianzad V, Gibbs-Strauss SL, et al. The FLARE intraoperative near-infrared fluorescence imaging system: a first-in-human clinical trial in breast cancer sentinel lymph node mapping. *Ann Surg Oncol*. 2009;16(10):2943-2952. doi:10.1245/s10434-009-0594-2

149. Hirche C, Engel H, Kolios L, et al. An experimental study to evaluate the Fluobeam 800 imaging system for fluorescence-guided lymphatic imaging and sentinel node biopsy. *Surg Innov*. 2013;20(5):516-523. doi:10.1177/1553350612468962
150. B. Mondal S, Gao S, Zhu N, et al. Binocular Goggle Augmented Imaging and Navigation System provides real-time fluorescence image guidance for tumor resection and sentinel lymph node mapping. *Sci Rep*. 2015;5(1). doi:10.1038/srep12117
151. Day KE, Beck LN, Heath CH, Huang CC, Zinn KR, Rosenthal EL. Identification of the optimal therapeutic antibody for fluorescent imaging of cutaneous squamous cell carcinoma. *Cancer Biol Ther*. 2013;14(3):271-277. doi:10.4161/cbt.23300
152. Shekhar A, Lin X, Liu FY, et al. Transcription factor ETV1 is essential for rapid conduction in the heart. *J Clin Invest*. 2016;126(12):4444-4459. doi:10.1172/JCI87968
153. Chandler N, Aslanidi O, Buckley D, et al. Computer Three-Dimensional Anatomical Reconstruction of the Human Sinus Node and a Novel Paranodal Area. *Anat Rec*. 2011;294(6):970-979. doi:10.1002/ar.21379